Università
degli Studi
di Ferrara

INSTYTUT FIZYKI JĄDROWEJ
IM. HENRYKA NIEWODNICZAŃSKIEGO
POLSKIEJ AKADEMII NAUK

Copernicus International Doctorate

The University of Ferrara
and
The Henryk Niewodniczański Institute of Nuclear Physics
Polish Academy of Sciences

Doctoral course in
Physics

Cycle XXXIII

Coordinator
Prof. Eleonora Luppi

Studies of the opto-electronic chain for the LHCb RICH upgrade

Scientific-disciplinary sector: FIS/01

Supervisor
Prof. Roberto Calabrese

Supervisor
Prof. dr hab. Tadeusz Lesiak

Auxiliary supervisor
Prof. Massimiliano Fiorini

Auxiliary supervisor
dr Agnieszka Dziurda

Ph.D. candidate
Igor Ślazyk

Thesis submitted for the degree of
Doctor of Philosophy
in Physics

2017-2021

For K.Ś.

Acknowledgments

I would like to express my deep gratitude to:

The LHCb Ferrara Group, in particular to
my supervisor **Prof. Roberto Calabrese**
and my auxiliary supervisor **Prof. Massimiliano Fiorini**
for enabling me a possibility to work
in a friendly environment on the exciting project,

The LHCb IFJ Group, in particular to
my supervisor **Prof. dr hab. Tadeusz Lesiak**
and my auxiliary supervisor **dr Agnieszka Dziurda**
for constant support, patience and kindness,

and to anyone who helped me during my Ph.D. studies.

Abstract

The present thesis describes in detail the quality assurance of the photodetectors and related electronics (the so-called Elementary Cells) for the RICH (Ring-Imaging Cherenkov) detectors upgrade of the LHCb experiment, performed on-site at the University of Ferrara. The objective of this thesis is the detailed discussion of the complete quality assurance process, from the development of the experimental test setup together with its software used for acquisition and analysis of measurement data, to the description of actual tests performed on the Elementary Cells and their results.

Riassunto

La presente tesi descrive in dettaglio il controllo di qualità dei fotorivelatori e relativa elettronica (le cosiddette celle elementari) per l'aggiornamento dei rivelatori RICH (Ring Imaging Cherenkov) dell'esperimento LHCb, realizzato presso l'Università di Ferrara. L'obiettivo di questa tesi è la discussione dettagliata del processo completo di controllo di qualità, dallo sviluppo del setup sperimentale di test, che include il software utilizzato per l'acquisizione e l'analisi dei dati, alla descrizione dei test effettivi eseguiti sulle celle elementari e dei loro risultati.

Streszczenie

Niniejsza praca opisuje szczegółowo testy jakości fotodetektorów i związanej z nimi elektroniki (tzw. komórek podstawowych) dla modernizacji detektorów promieniowania Czerenkowa RICH (ang. Ring-Imaging Cherenkov), wchodzącego w skład spektrometru LHCb, dokonanych w Uniwersytecie w Ferrarze. Celem pracy jest szczegółowe omówienie kompletnego procesu kontroli jakości, od rozwoju zestawu pomiarowego przeznaczonego do testów wraz z jego oprogramowaniem służącym do akwizycji i analizy danych pomiarowych, aż do opisu samych pomiarów dokonanych na komórkach elementarnych i ich rezultatów.

Contents

Acronyms

ADC Analog-to-Digital Converter

ALICE A Large Ion Collider Experiment

AMS Austria Microsystems

ASIC Application-Specific Integrated Circuit

ATLAS A Toroidal LHC ApparatuS

Bb Base Board

Bkb Back Board

$\mathcal{C}$ Charge Conjugation

CERN Organisation Européenne Pour la Recherche Nucléaire

CKM Cabibbo-Kobayashi-Maskawa

CMS Compact Muon Solenoid

$\mathcal{CP}$ Charge-Parity

DAC Digital Analog Converter

DAQ Data Acquisition

DB Digital Board

DCR Dark Count Rate

EC Elementary Cell

ECAL Electromagnetic Calorimeter

ERF Error Function

ESD Electrostatic Discharge

FCNC Flavour-Changing Neutral Current

FE Front-End

FEB Front-End Board

FPGA Field-Programmable Aate Array

GEM Gas Electron Multiplier

GIM Glashow–Iliopoulos–Maiani

GUI Graphical User Interface

HCAL Hadronic Calorimeter

HLT High Level Trigger

HPD Hybrid Photon Detector

HV High Voltage

IFJ PAN Institute of Nuclear Physics Polish Academy of Sciences

IT Inner Tracker

L0 Level-0

LEP Electron-Positron Collider

LHC Large Hadron Collider

LHCb Large Hadron Collider beauty

LHCf Large Hadron Collider forward

LINAC 2 Linear Accelerator

LS Long Shutdown

LV Low Voltage

MaPMT Multi-Anode Photomultiplier Tube

MoEDAL Monopole and Exotics Detector at the LHC

MVA Multivariate Analysis

MWPC Multi Wire Proportional Chambers

NP New Physics

OT Outer Tracker

$\mathcal{P}$ Parity

PDA Photon Detector Assembly

PDMDB Photon Detector Module Digital Board

PID Particle Identification

PMT Photomultiplier Tube

PS Proton Synchrotron

PS Preshower

PSB Proton Synchrotron Booster

QA Quality Assurance

QCD Quantum Chromodynamics

QED Quantum Electrodynamics

QR Quick Response

RHBD Radiation Hardened By Design

RICH Ring-Imaging Cherenkov

RPI Raspberry Pi

S/N Signal to Noise

SBA Super Bi-Akali

SciFi Scintillating Fiber

SEU Single Event Upset

SIN Signal Induced Noise

SiPM Silicon PhotoMultplier

SM Standard Model

SPD Scintillating Pad Detector

SPI Serial Peripheral Interface

SPS Super Proton Synchrotron

TCP Transmission Control Protocol

TID Total Ionising Dose

TMR Triple Modular Redundancy

TOTEM TOTal Elastic and diffractive cross section Measurement

TT Tracker Turicensis

UART Universal Asynchronous Receiver-Transmitter

UBA Ultra Bi-Akali

UNIFE University of Ferrara

UT Upstream Tracker

VELO Vertex Locator

VI Virtual Instrument

List of Figures

List of Tables

Introduction

According to the Big Bang theory, at the very earliest period of the Universe evolution (approximately 13.8 billion years ago), equal amounts of matter and antimatter were created. Particles and corresponding antiparticles were annihilating with each other, disappearing in bursts of light - photons. The process of the annihilation should have continued unceasingly. However, at certain point, the asymmetry between matter and antimatter had arisen and resulted is the observable Universe. This asymmetry can be generated upon the fulfillment of the three Sakharov conditions [1]. One of them is the requirement of the violation of charge-parity ($\mathcal{CP}$) symmetry. The latter, the combination of charge conjugation ($\mathcal{C}$) and parity ($\mathcal{P}$) operations, states that the laws of physics stay the same for particles interchanged with their antiparticles (charge conjugation) while their spatial coordinates are inverted (parity).

Physicists working at The Large Hadron Collider beauty (LHCb) experiment (one of the four major spectrometers taking data at the Large Hadron Collider at CERN), which is dedicated for the study of evidences of $\mathcal{CP}$ violation, try to unravel this mystery. It has been observed that $\mathcal{CP}$-symmetry is retained for the electromagnetic and strong interaction but is violated for certain types of weak decays. Thus, the efforts are made to search for new, exotic phenomena (so called New Physics (NP)) beyond the current theory, called the Standard Model, in the rare decays of bottom (b) and charm (c) hadrons at the LHCb experiment. These studies are motivated by the fact that the current amount of $\mathcal{CP}$ violation in the Standard Model is too small to explain the observed baryon-antibaryon asymmetry in our Universe.

The ongoing upgrade of the LHCb experiment will significantly increase the performance of the LHCb spectrometer and, as a result, the interesting processes will be able to be detected at much higher rate. As a joint Ph.D. student working in two LHCb groups, in the University of Ferrara (UNIFE) and the Institute of

Nuclear Physics Polish Academy of Sciences (IFJ PAN) in Kraków, my studies focused on the current LHCb detector upgrade. More specifically, on the Ring-Imaging Cherenkov (RICH) detectors upgrade, which are essential for the particle identification of charged hadrons.

The present thesis is organized as follows: Chapter 1 concentrates on the LHCb physics programme with the special attention paid to $\mathcal{CP}$-violating phenomena. Chapter 2 presents an overview of the Large Hadron Collider and one of its main experiments in details - the above-mentioned LHCb experiment. The current status of the detectors of the LHCb spectrometer is presented together with their running upgrade. It is followed by Chapter 3 which focuses entirely on the RICH detection system. The chapter describes the pre- and post-upgraded status of the detectors with a particular emphasis placed on the Elementary Cell (EC) upgrade - the new detection system. Chapter 4 presents the importance of the particle identification in the physics analyses. Chapter 5 presents the main objective of my Ph.D. studies - the Elementary Cell Quality Assurance (ECQA). In the last Chapter 6, conclusions are summarized.

My work, described in detail in Chapter 5, involves a preparation and optimization of the experimental test setup used for quality control of the ECs, software development of the automated software (stages of the LabVIEW-python interface, LabVIEW Commands, Standalones and temperature-humidity read-out software) and development of the offline data analysis scripts. As I was appointed responsible for the ECQA measurements, I prepared the EC assembling procedure and the ECQA test protocol. Following the instructions, I performed mapping tests and quality control measurements for all the assembled ECs in Ferrara. Based on the obtained results, I performed the ECQA data analysis with a great focus placed on Signal Induced Noise. In addition to that, I performed a simplified data analysis of the $B_s^0 \to D_s^{\mp} K^{\pm}$ decays, found in Chapter 4. The entire work was designed, and performed under my coordination.

Chapter 1

Physics at LHCb

The physics programme at the LHCb experiment focuses on flavour physics. In this chapter, a brief discussion of the Standard Model is presented, which is followed by an introduction to $\mathcal{CP}$ violation exemplified, in particular, on one of the rare decays at the LHCb and a list of key measurements carried on at the LHCb.

1.1 Standard Model

The Standard Model (SM) [2] is a set of mathematical principles that, with an experimental verification over time, resulted in a physics theory. It describes the three, out of the four, fundamental forces (electromagnetic, weak and strong) governing the Universe and known elementary particles that make up matter. The theory demonstrated a great success in the verification of its experimental predictions, such as the existence of the top [3][4] and charm quark [5][6], tau neutrino, $W^{\pm}$ and Z^0 bosons, gluon [7] and, last but not least, the Higgs boson [8].

Elementary particles are divided into two categories: building blocks of matter (fermions) and force carrying particles (bosons). In the SM, each elementary fermion q has their counterpart antiparticle $\overline{q}$, which forms matter and antimatter, respectively. The difference between them lies in the opposite quantum numbers while having the exact same masses.

Fermions are characterised by half-integer spin and follow Fermi-Dirac statistics and thus the obedience of the Pauli exclusion principle. They are split into two groups based on their properties and interactions. The first group, called leptons, contains three charged particles: electron e, muon μ, tau τ and their neutral neutrino equivalents: electron neutrino υ_e, muon neutrino υ_μ and tau neutrino υ_τ. The charged leptons interact via the weak and electromagnetic interaction whereas neutrinos only via the weak interaction since they do not carry electric charge. An overview of leptons is reported in Table 1.1. According to the SM, there are three generations (labelled as Gen. in the table). Between the generations, particles differ by their mass and flavour quantum numbers while their strong and electric interactions remain the same.

Table 1.1: Leptons described in the SM. The values are taken from [9].

Gen.	Name	Symbol	Electric Charge	Mass [MeV/c^2]
1	Electron	e^-	-1	0.51
2	Muon	μ^-		105.66
3	Tau	τ^-		1776.86
1	Electron neutrino	v_e	0	< 0.002
2	Muon neutrino	v_μ		< 0.002
3	Tau neutrino	v_τ		< 0.002

The second group, named quarks, similarly to leptons, consists of six particles: up u, down d, charm c, strange s, truth (top) t and beauty (bottom) b and of the respective six antiquarks. Depending on their electric charge, quarks can be referred as up-type ($+\frac{2}{3}e$) or down-type ($-\frac{1}{3}e$) ones. Quarks are the basic building unit of strongly-interacting bound states, called hadrons. They interact via the electromagnetic and strong interaction involving color, which is analogous to charge in the electromagnetic force. In order to satisfy the Pauli exclusion principle, a strong charge with three manifestations, labeled as red, green, blue for quarks and the respective three anticharges, antired, antigreen, antiblue for antiquarks, has been proposed. Constant exchange of color and anticolor charges carried by the strong force intermediate bosons, called gluons, makes quarks to be always confined to bound states. As a result of that, they are never observed on their own in nature, in contrast to leptons. An overview of quarks is shown in Table 1.2.

Table 1.2: Quarks described in the SM. The values are taken from [9].

Gen.	Name	Symbol	Electric Charge	Color Charge	Mass [MeV/c^2]
1	Up	u	$+\frac{2}{3}$	$R/G/B$	2.2
	Down	d	$-\frac{1}{3}$		4.7
2	Charm	c	$+\frac{2}{3}$		1270
	Strange	s	$-\frac{1}{3}$		96
3	Truth (Top)	t	$+\frac{2}{3}$		173210
	Beauty (Bottom)	b	$-\frac{1}{3}$		4180

The interactions between fermions are transferred by the second category of elementary particles called gauge bosons which are characterised by integer spin equal to 1 (except for spin zero for the Higgs boson, and spin 2 for the hypothetical carrier of gravitational interaction, called graviton) and follow Bose-Einstein statistics. Gauge bosons (Table 1.3) are the carriers of the three fundamental forces:

- Photons γ mediate the electromagnetic force between electrically charged particles. Photons are electrically neutral and massless particles. Their interaction is described by quantum electrodynamics (QED) [10][11][12] - the gauge theory with the symmetry group $U(1)_Q$, where the index Q refers to the electric charge.

- The $W^{\pm}$ and Z^0 bosons mediate the weak force. Two types of bosons are distinguished: the $W^{\pm}$ carrying charged current and the Z^0 carrying neutral current. Their masses are explained by the Higgs mechanism. Their interaction is described by electroweak theory of Glashow [13], Salam [14] and Weinberg [15] combining the electromagnetic interaction and the weak interaction - the gauge theory with the symmetry group $SU(2)_T \otimes U(1)_Y$, where the indices T and Y refer to the weak isospin and the weak hypercharge, respectively.

- Gluons mediate the strong force between the color charged particles (quarks). Gluons are electrically neutral and massless particles. Their interaction is described by quantum chromodynamics (QCD) [16][17] - the gauge theory with the symmetry group $SU(3)_C$, where the index C refers to the color quantum number.

Table 1.3: Bosons described in the SM. The values are taken from [9].

Name	Symbol	Type of Interaction	Electric Charge	Mass [GeV/c^2]
Photons	γ	electromagnetic	0	0
W^+, W^- bosons	W^+, W^-	weak	+1, −1	80.39
Z^0 boson	Z^0		0	91.19
Gluons	g	strong	0	0
Higgs boson	H^0	-	0	125.09

The last elementary particle completing the SM, the Higgs boson H^0, was observed experimentally in 2012 [18][19]. The H^0 is not related to any fundamental force. Its existence was predicted in order to provide explanation for mass generation mechanism in the SM. It is the only elementary scalar particle with a spin equal to zero which has been observed experimentally. The particle is electrically neutral and has a mass of around 125 GeV/c^2. Its discovery was essential as it confirmed that the Higgs boson is responsible, in particular, for the generation of the $W^\pm$ and Z^0 bosons masses. By spontaneous symmetry breaking of the $SU(2)_T \otimes U(1)_Y$ gauge symmetry induced by the presence of the Higgs field [20][21], charged leptons and gauge bosons acquire their masses through the Higgs mechanism.

Bound states of quarks (hadrons) are divided according to the number of quarks they possess. Mesons are particles that are built as quark-antiquark ($q\overline{q}$) pairs like e.g. pions (π) and kaons (K). Baryons are composed of three quarks (qqq) such as proton (uud) and neutron (udd). Finally, tetraquarks and pentaquarks, included in the group of exotic hadrons, are bound states of four ($qq\overline{q}\overline{q}$) and five ($qqqq\overline{q}$) quarks, respectively.

Although, the SM is a very successful theory, it lacks an explanation to certain issues:

- Gravitational force - the fourth force of nature is not a part of the SM. The gravity does not impact the micro-world much, as it is the weakest force. When considering the macro-world, the situation changes. Merging the theory of general relativity and the quantum field theory occurred to be extremely difficult and so far unsuccessful. According to predictions, the gravitational force carrier, called graviton, should exist.

- Neutrinos - in compliance with the SM, neutrinos should be massless. However, it is contradicted by the current observations [22][23] as it was proven that neutrinos oscillate, thus they posses mass.
- Dark matter - a big portion of the Universe is believed to be made of dark matter which is not included in the SM. It is unknown if dark matter is composed of baryonic or non-baryonic matter.
- Matter-antimatter asymmetry - matter and antimatter were created in equal amounts at the beginning of the Universe. The balance was tipped and resulted in the observable Universe. Although the SM predicted the $\mathcal{CP}$-violation, the amount of $\mathcal{CP}$-violation provided in the SM is too small to explain the matter-antimatter asymmetry in our Universe.

Physics at the LHCb concentrates on the last-mentioned mystery. It is important to study all the three generations of quarks to totally explore the CKM matrix (§ 1.2.1). The LHCb focuses on the third and second generation through the study of decays of b- and c-flavoured hadrons and precision measurements of $\mathcal{CP}$-violating observables.

1.2 CP Violation

The matter-antimatter asymmetry occurs if a set of three necessary Sakharov conditions [1] are met:

- baryon number violation,
- interactions out of thermal equilibrium,
- $\mathcal{C}$ and $\mathcal{CP}$ symmetry violation.

The $\mathcal{CP}$ operator is a combination of the charge conjugation $\mathcal{C}$ and the parity $\mathcal{P}$ operator. Each of them leads to the conservation of a multiplicative quantum number and represents discrete symmetries.

Charge conjugation $\mathcal{C}$ is responsible for swapping the sign of all quantum charges. This operation results in the transformation of particles into their antiparticles, as shown in the examples below:

$$\mathcal{C} : (e^-) \rightarrow e^+, \quad \mathcal{C} : (\pi^0) \rightarrow \overline{\pi}^0. \tag{1.1}$$

The second operator is parity $\mathcal{P}$ which alters the sign of the quantum number describing spin of particles. It changes the sign of the space coordinates $\overrightarrow{r} = (x, y, z)$ and, as a result, the handedness of the system of axes. This operation leads to a transformation of particles into the mirror image in comparison to the initial position:

$$\mathcal{P} : \begin{pmatrix} x \\ y \\ z \end{pmatrix} \rightarrow \begin{pmatrix} -x \\ -y \\ -z \end{pmatrix}. \tag{1.2}$$

When the $\mathcal{CP}$ operator is performed on a system, particles are turned into antiparticles and are mirrored. Apart from the so-called strong $\mathcal{CP}$-puzzle [24], the strong and electromagnetic interactions are invariant under the $\mathcal{CP}$ transformation. For the weak interaction, it was first discovered in 1964 that $\mathcal{CP}$ symmetry is violated in the decays of neutral kaons [25].

1.2.1 CKM Matrix

$\mathcal{CP}$ violation is mediated by $W^\pm$ exchange described by the Lagrangian of the weak charged currents:

$$\frac{g}{\sqrt{2}}(\overline{U}\gamma^\mu V_{CKM} D_L W_\mu^- + \overline{D}_L \gamma^\mu V_{CKM}^\dagger U_L W_\mu^+), \tag{1.3}$$

where g is the electroweak coupling constant, U and D corresponds to the weak eigenstates of the left-handed up-type quarks (u, c, t) and down-type quarks (d, s, b) respectively, W_μ represents the field of intermediate boson $W^\pm$, γ^μ are Dirac matrices and ultimately V_{CKM} is the unitary 3x3 Cabibbo-Kobayashi-Maskawa (CKM) matrix [26][27]. The weak decays, mediated by the $W^\pm$ bosons, change the up-type to the down-type quarks and also the down-type to the up-type quarks. The CKM matrix is defined as:

$$V_{CKM} = \begin{pmatrix} V_{ud} & V_{us} & V_{ub} \\ V_{cd} & V_{cs} & V_{cb} \\ V_{td} & V_{ts} & V_{tb} \end{pmatrix}. \tag{1.4}$$

where V_{ij} denotes the flavour-changing weak coupling between q_i and q_j quarks. The weak eigenstates (d', s', b') and mass eigenstates (d, s, b) are correlated with the CKM matrix with the following formula:

$$\begin{pmatrix} d' \\ s' \\ b' \end{pmatrix} = V_{CKM} \begin{pmatrix} d \\ s \\ b \end{pmatrix} = \begin{pmatrix} V_{ud} & V_{us} & V_{ub} \\ V_{cd} & V_{cs} & V_{cb} \\ V_{td} & V_{ts} & V_{tb} \end{pmatrix} \begin{pmatrix} d \\ s \\ b \end{pmatrix}, \tag{1.5}$$

To describe the 3x3 matrix of complex numbers, 18 parameters are required. As the V_{CKM} is an unitary matrix, the parameters are reduced to 9. In addition, 5 parameters can be neglected as they are relative phases between the quark fields. Hence only 4 degrees of freedom remain: the three rotation angles θ_{12}, θ_{13}, θ_{23} and the weak phase δ which corresponds to the source of $\mathcal{CP}$ violation in the SM. One of the purpose of flavour physics is to determine whether the above-mentioned scheme correctly describes the observed amplitudes and process phases.

A widely used parametrisation of the CKM matrix, that shows the hierarchy of modules $|V_{ij}|$, is the Wolfenstein parametrisation [28], which implements the following parameters: λ, A, ρ and η. It is experimentally proven that $sin(\delta_{12}) = 0.22 \equiv \lambda$, which describes the mixing between the first and second generation of quarks (also known as the Cabibbo angle [29]). Limiting to the third order of the λ parameter, the CKM matrix in the Wolfenstein parametrisation reads as:

$$V_{CKM} = \begin{pmatrix} 1 - \frac{\lambda^2}{2} & \lambda & A\lambda^3(\rho - i\eta) \\ -\lambda & 1 - \frac{\lambda^2}{2} & A\lambda^2 \\ A\lambda^3(1 - \rho - i\eta) & -A\lambda^2 & 1 \end{pmatrix}, \tag{1.6}$$

where λ, A, ρ are real parameters and η is the imaginary parameter that quantifies the size of $\mathcal{CP}$ violating effects in the SM. Since the imaginary parameter η is present in the V_{ub} element, the b-hadron decays involving this transition are particularly interesting and widely studied in the LHCb experiment. The current values of the Wolfenstein parameters, measured experimentally, are [30]:

$$A = 0.823^{+0.015}_{-0.029}, \quad \lambda = 0.22484^{+0.00097}_{-0.00018}, \quad \overline{\rho} = 0.157^{+0.036}_{-0.019}, \quad \overline{\eta} = 0.350^{+0.027}_{-0.023}, \tag{1.7}$$

where $\overline{\rho} = \rho(1 - \frac{\lambda^2}{2})$ and $\overline{\eta} = \eta(1 - \frac{\lambda^2}{2})$. The elements of the CKM matrix, that provide the probabilities of quark transitions, are currently equal to (following [30]):

$$V_{CKM} = \begin{pmatrix} 0.974390^{+0.000041}_{-0.000225} & 0.22483^{+0.00097}_{-0.00018} & 0.00368^{+0.00028}_{-0.00018} \\ 0.22470^{+0.00097}_{-0.00018} & 0.973539^{+0.000081}_{-0.000229} & 0.04162^{+0.00078}_{-0.00142} \\ 0.00855^{+0.00024}_{-0.00038} & 0.04090^{+0.00075}_{-0.00138} & 0.999127^{+0.000058}_{-0.000033} \end{pmatrix}. \tag{1.8}$$

1.2.2 Unitarity Triangle

The useful property of the CKM matrix lies in its unitarity:

$$V_{CKM} V^{\dagger}_{CKM} = V^{\dagger}_{CKM} V_{CKM} = 1, \tag{1.9}$$

which leads to a set of 6 orthogonality equations where products of different columns and rows of the CKM matrix sum up to 0. This set of conditions can be represented graphically as triangles in the complex plane where each term is identified as a side of a triangle. In particular, after applying Equation 1.9 to the first and third column of the CKM matrix, the following equation is produced:

$$V_{ud} V^*_{ub} + V_{cd} V^*_{cb} + V_{td} V^*_{tb} = 0. \tag{1.10}$$

This corresponds to the so-called Unitary Triangle, for which the lengths of each sides are of the same order of magnitude. By implementing the Wolfenstein parameters, the sides of the Unitarity Triangle are equal to:

$$\begin{aligned} V_{ud} V^*_{ub} &= A\lambda^3 (\rho + i\eta)(1 - \frac{\lambda^2}{2}), \\ V_{cd} V^*_{cb} &= -A\lambda^3, \\ V_{td} V^*_{tb} &= A\lambda^3 ((1 - \rho - i\eta) + \lambda^2 (\rho + i\eta)), \end{aligned} \tag{1.11}$$

and the corresponding angles of the Unitarity Triangle are defines as:

$$\begin{aligned} \alpha &= \arg\left(-\frac{V_{td} V^*_{tb}}{V_{ud} V^*_{ub}}\right) = \arg\left(\frac{(1 - \frac{\lambda^2}{2})(i\eta - \rho)}{1 - \rho - i\eta}\right), \\ \beta &= \arg\left(-\frac{V_{cd} V^*_{cb}}{V_{td} V^*_{tb}}\right) = \arg\left(\frac{1}{1 - \rho - i\eta}\right), \\ \gamma &= \arg\left(-\frac{V_{ud} V^*_{ub}}{V_{cd} V^*_{cb}}\right) = \arg\left((1 - \frac{\lambda^2}{2})(\rho - i\eta)\right). \end{aligned} \tag{1.12}$$

A graphical representation of a set of Equation 1.11 and Equation 1.12 is presented in Figure 1.1 in the $(\overline{\rho}, \overline{\eta})$ plane.

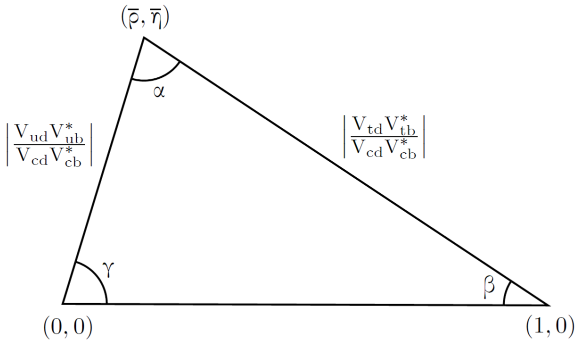

Figure 1.1: The Unitarity Triangle resulted by Equation 1.10 in the $(\overline{\rho}, \overline{\eta})$ plane.

Figure 1.2 shows the measurements of sides and angles (colored areas) of the Unitarity Triangle performed within the LHCb collaboration. The complex plane is defined as $(\overline{\rho}, \overline{\eta})$. The area in the upper vertex of the Unitarity Triangle represents the experimental uncertainties of the CKM matrix elements. If the unitarity conditions were not preserved, the Unitarity Triangle would not close and as a consequence this could lead to the presence of new phenomena (NP). The LHCb upgrade significantly increases the sensitivity of Unitarity Triangle parameters determination and narrows the experimental uncertainties substantially. The anticipated improvements by 2025, where 23 fb^{-1} is expected to be collected, are shown in Figure 1.3.

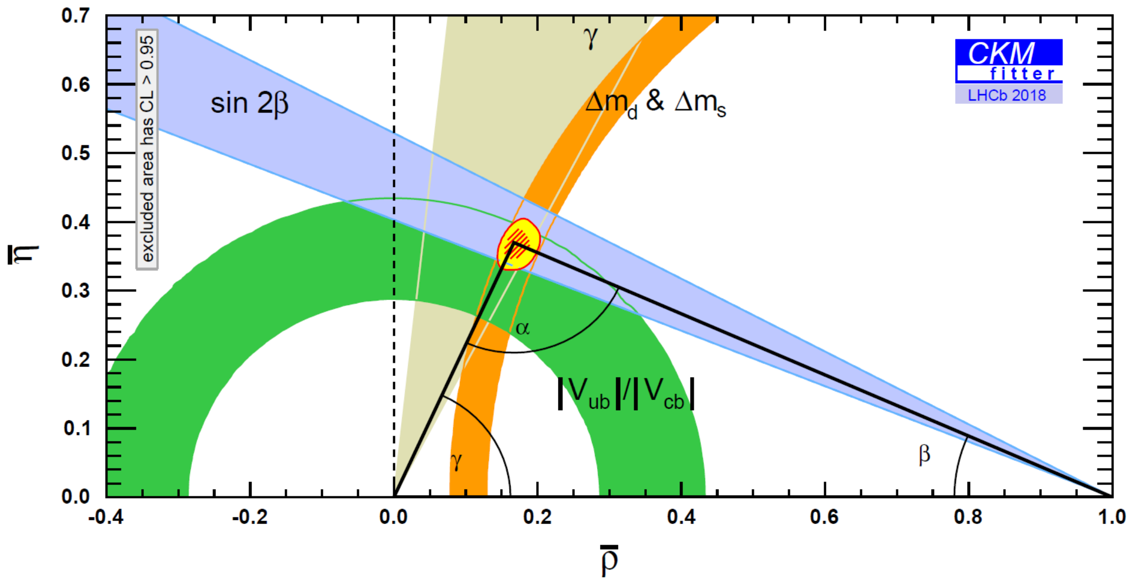

Figure 1.2: The Unitarity Triangle constrained in the complex $\overline{\rho}$-$\overline{\eta}$ plane from the data accumulated by the LHCb by 2018 (9 fb^{-1}) [31].

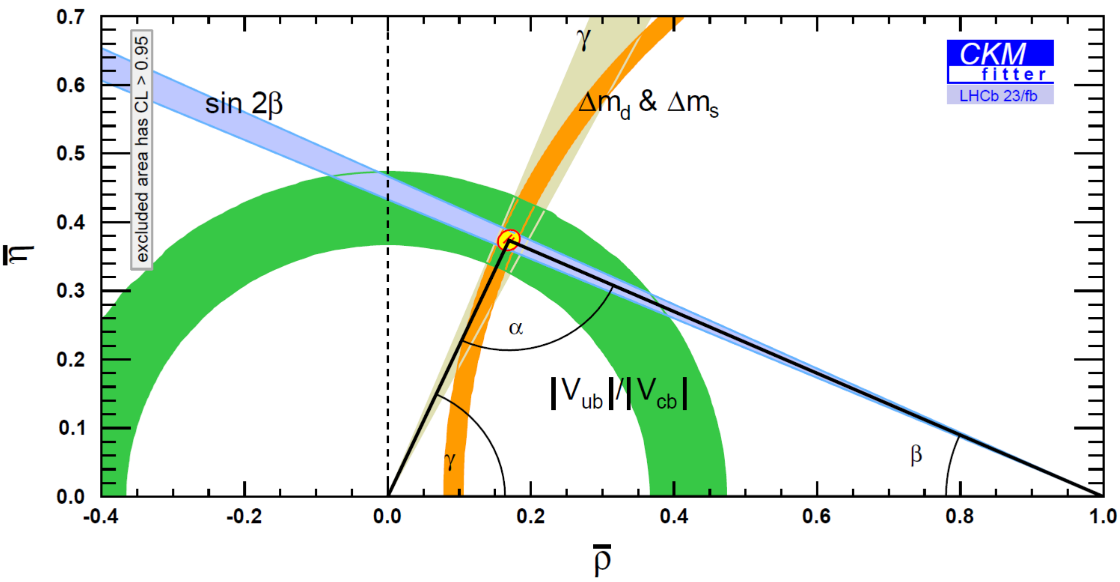

Figure 1.3: The anticipated Unitarity Triangle constrained in the complex $\overline{\rho}$-$\overline{\eta}$ plane assuming 23 fb^{-1} accumulated by the LHCb experiment by 2025 [31].

1.3 Rare Decays at LHCb

A significant part of the LHCb physics programme focuses on the so-called rare decays i.e. the decays that proceed through loop and CKM suppressed diagrams in the SM or are forbidden within it. Some examples of these measurements are: studies of the leptonic decays ($B_s^0 \to \mu^+\mu^-$ [32]), searches for lepton-flavour ($B^0 \to e^\pm\mu^\mp$ [33], $\tau^\pm \to \mu^\pm\mu^+\mu^-$ [34]), lepton-number ($B^- \to \pi^+\mu^-\mu^-$ [35]) and baryon-number violating (Ξ_b^0 oscillations [36]) decays.

One of the promising rare decays involve neutral mesons made of the b quark: B_s^0 ($\bar{b}s$) and B^0 ($\bar{b}d$). The mentioned mesons decay into a pair of muons as presented in Figure 1.4 for B_s^0. The branching fractions are predicted very accurately by the SM: $\mathcal{B}(B_s^0 \to \mu^+\mu^-)_{SM} = (3.65 \pm 0.23) \times 10^{-9}$, $\mathcal{B}(B^0 \to \mu^+\mu^-)_{SM} = (1.06 \pm 0.09) \times 10^{-10}$ [37]. Any deviation from these values would possibly indicate the NP beyond the SM. The very low branching fraction of these decays is caused by few factors. The weak interactions are responsible for the change of quark flavours. It is forbidden to change the flavour within the different generations of the same quark type, either down or up. Thus, the tree-level $b \to s$ or $b \to d$ transitions mediated by the Z^0 boson are prohibited.

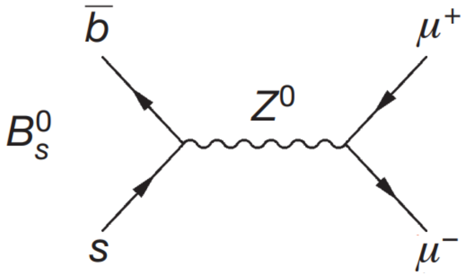

Figure 1.4: Scheme presenting forbidden direct Flavour-Changing Neutral Current (FCNC) for the $B_s^0 \to \mu^+\mu^-$ decay according to the SM.

Nevertheless, these decays can occur through the higher order transitions, as presented in Figure 1.5. The loop-level transitions are rare as they requires multiple weak interactions and presence of the Glashow-Iliopoulos-Maiani (GIM) suppression factor [38]. Furthermore, as the B_s^0 and B^0 mesons are spin zero particles, thus only those decay paths that produce a final state with zero total angular momentum are allowed. This results in additional so-called the helicity suppression at the level of $\sim 4 \times 10^{-4}$. One order of magnitude difference between predicted branching fraction for $B_s^0 \to \mu\mu$ and $B^0 \to \mu\mu$ comes from the fact, the latter is further suppressed by the ratio of CKM matrix elements $|V_{td}|/|V_{ts}|^2$.

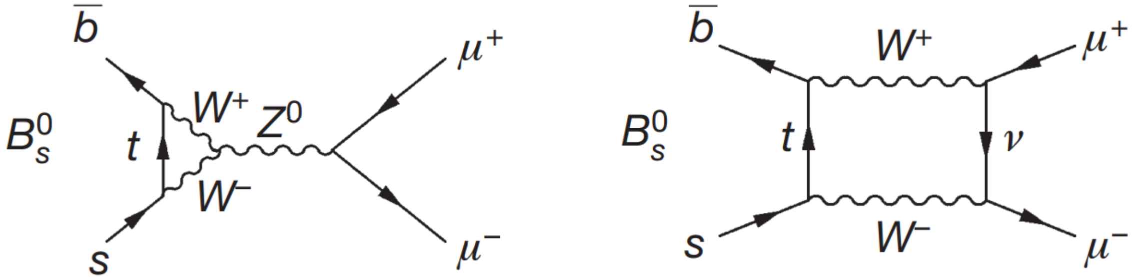

Figure 1.5: Higher-order Feynman's diagrams for the $B_s^0 \to \mu^+\mu^-$ decay allowed in the SM [39].

So far, the measurement performed by the LHCb proved the correctness of the SM predictions. The results lie in the acceptable range: $\mathcal{B}(B_s^0 \to \mu^+\mu^-) = (3.0 \pm 0.6^{+0.3}_{-0.2}) \times 10^{-9}$, $\mathcal{B}(B^0 \to \mu^+\mu^-) < 3.4 \times 10^{-10}$ [32]. More precise measurements in the future are needed to provide strong constraints (or evidence) for new flavour structures beyond the SM.

1.4 LHCb Physics Programme

A general overview of the LHCb programme of the key measurements is presented in Table 1.4. In addition, the current and future sensitivities of measurements are listed. The current LHCb upgrade provides an exceptional increase of the precision.

Table 1.4: Summary of sensitivities of measurements of selected flavour observables for the current and post-upgraded LHCb [31].

Observable	Current LHCb	LHCb 2025
EW Penguins		
$R_K(1 < q^2 < 6\ \mathrm{GeV}^2/\mathrm{c}^4)$	0.1 [40]	0.025
$R_{K*}(1 < q^2 < 6\ \mathrm{GeV}^2/\mathrm{c}^4)$	0.1 [41]	0.031
R_ϕ, R_{pK}, R_π	-	0.08, 0.06, 0.18
CKM tests		
γ, with $B_s^0 \to D_s^+ K^-$	$\left(^{+17^\circ}_{-22^\circ}\right)$ [42]	4°
γ, all modes	$\left(^{+5.0^\circ}_{-5.8^\circ}\right)$ [43]	1.5°
$\sin 2\beta$, with $B^0 \to J/\psi K_s^0$	0.04 [44]	0.011
ϕ_s, with $B_s^0 \to J/\psi\phi$	49 mrad [45]	14 mrad
ϕ_s, with $B_s^0 \to D_s^+ D_s^-$	170 mrad [46]	35 mrad
$\phi_s^{s\bar{s}s}$, with $B_s^0 \to \phi\phi$	154 mrad [47]	39 mrad
a_{sl}^s	33×10^{-4} [48]	10×10^{-4}
$\lvert V_{ub}\rvert/\lvert V_{cb}\rvert$	6% [49]	3%
$\boldsymbol{B_s^0, B^0 \to \mu^+\mu^-}$		
$\mathcal{B}(B^0 \to \mu^+\mu^-)/\mathcal{B}(B_s^0 \to \mu^+\mu^-)$	90% [32]	34%
$\tau_{B_s^0 \to \mu^+\mu^-}$	22% [32]	8%
$S_{\mu\mu}$	-	-
$\boldsymbol{b \to c l^- \bar{\nu}_l}$ **LUV studies**		
$R(D^*)$	0.026 [50][51]	0.0072
$R(J/\psi)$	0.24 [52]	0.071
Charm		
$\Delta A_{CP}(KK - \pi\pi)$	8.5×10^{-4} [53]	1.7×10^{-4}
$A_\Gamma(\approx x \sin\phi)$	2.8×10^{-4} [54]	4.3×10^{-5}
$x\sin\phi$ from $D^0 \to K^+\pi^-$	13×10^{-4} [55]	3.2×10^{-4}
$x\sin\phi$ from multibody decays	-	$(K3\pi)$ 4.0×10^{-5}

Chapter 2

LHCb Experiment

The LHCb experiment is one of the major experiments running at the Large Hadron Collider. It focuses on heavy flavour physics and seeks evidences of NP by measuring properties of b- and c-flavoured hadrons decays. In particular, the LHCb experiment aims to study the $\mathcal{CP}$ violation phenomena and search for the rare B meson decays. In this chapter, the LHC is briefly discussed. It is followed by an overview of the LHCb experiment, where technical details of the subdetectors are presented together with their planned upgrade.

2.1 Large Hadron Collider

The Large Hadron Collider (LHC) [56] is the largest ring-hadron accelerator and particle collider in the world. The LHC was developed and built by the Organisation Européenne Pour la Recherche Nucléaire (Eng. European Organisation for Nuclear Research, CERN), the international European research organisation uniting researchers from all around the world.

The machine uses ~26.7 km long circular tunnel located in the French-Swiss border close to Geneva. A geographical location is presented in Figure 2.1. The tunnel is a descendent of the Large Electron-Positron Collider (LEP) [57] operating in the years 1989-2000. Two adjacent 3.8 m wide beam pipes, parallel to each other, at depth ranging from 50 m to 175 m at 100 m average, are used for accelerating particles, such as protons or heavy ions.

The main objective of the LHC are proton-proton (pp) collisions but other types of collisions also take place, such as lead-lead (PbPb), proton-lead (pPb) and proton-helium (pHe), for the broadest possible scientific programme. Beam pipes intersect

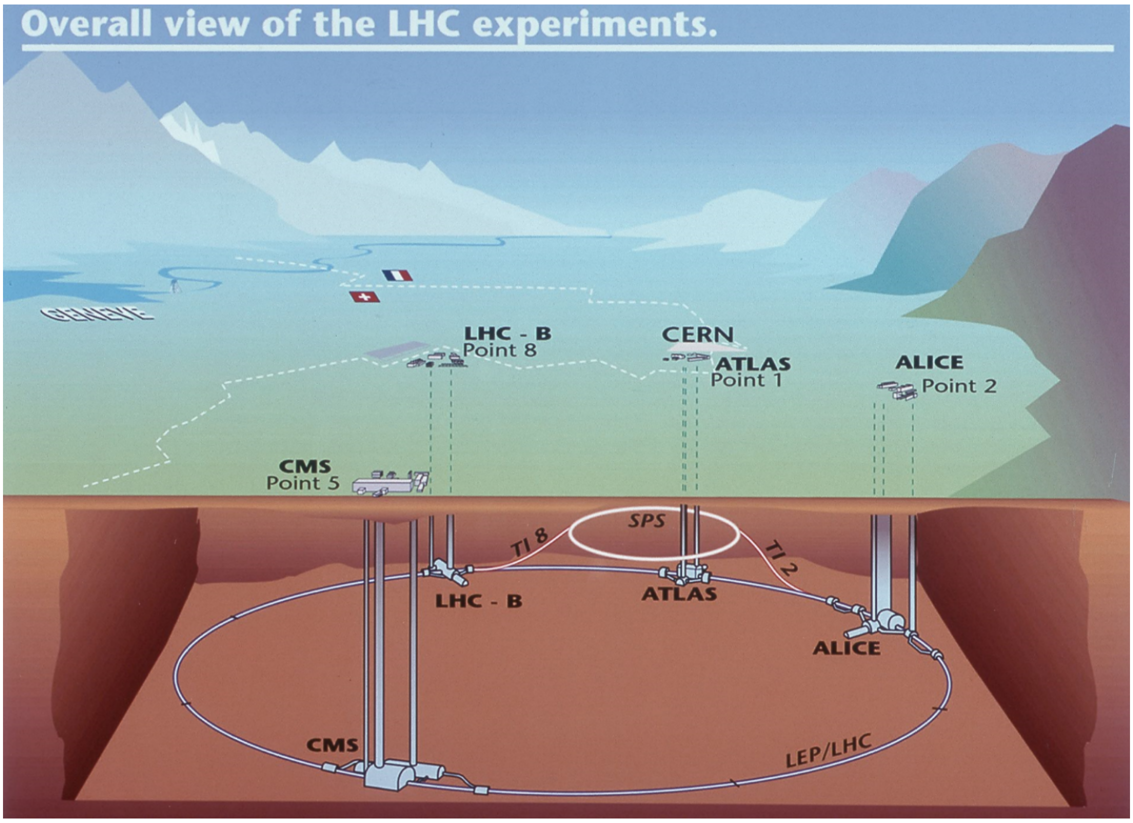

Figure 2.1: The geographical representation of the LHC accelerator ring and four main experiments CMS, ATLAS, ALICE and LHCb [58].

at four different crossing points, allowing particle bunches to collide with each other. During the first two LHC data taking periods, so-called the LHC Run I and II (2010-2018), seven unique experiments were in operation:

- ATLAS (A Toroidal LHC ApparatuS) [59] – the first general-purpose and the largest particle detector running at the LHC. It was designed to perform a large variety of analyses including the precise measurements of the Standard Model predictions, such as Higgs boson discovery [18][19] and searches of New Physics with possible detection of new particles.

- CMS (Compact Muon Solenoid) [60] – the second general-purpose detector operating at the LHC. Although, the goal is the same as in the ATLAS experiment, it uses different technical solutions and a different magnet-system design. Both ATLAS and CMS are essential for cross-checking potential observations of new phenomena.

- ALICE (A Large Ion Collider Experiment) [61] – a detector developed for heavy ions ($PbPb$) collisions to study the physics of matter at extreme energy densities, in particular a phase of matter called quark-gluon plasma.
- LHCb (Large Hadron Collider beauty) [62] – a general-purpose detector in the forward direction designed for the experiment specialising in the study of beauty quarks necessary for explanation of matter-antimatter asymmetry of the Universe. A thorough description is covered in Section 2.2.
- LHCf (Large Hadron Collider forward) [63] – a detector located near the ATLAS interaction point with the aim of studying protons themselves, such as diffractive physics occurring in the forward region of the pp collisions.
- TOTEM (TOTal Elastic and diffractive cross section Measurement) [64] – a detector located near the CMS interaction point with the same purpose as LHCf.
- MoEDAL (Monopole and Exotics Detector at the LHC) [65] – a detector, located at the LHCb, searching for a hypothetical particle with magnetic charge, called the magnetic monopole.

The LHC has the largest cryogenic system in the world [66]. Approximate number of 9300 superconducting niobium-titanium copper-clad magnets, all of them being electromagnets, keep particles at favourable tracks. There are more than 50 different types of these magnets installed in the LHC. One of them, the dipole magnets in the number of 1232, are used to bend the path of accelerating particle beams to keep them on course. They generate magnetic field equal to 8.33 T with the current of 11080 A flowing inside the magnets. The operating temperature of dipoles is equal to 1.9 K (-271.25°C). Superfluid helium-4, the only element in liquid state at such low temperature, is used to allow magnets operate in superconducting state without losing an energy to a resistance. There are also 858 quadrupole magnets that are used to squeeze the beam to achieve higher rate of collisions between two beams of particles at intersections.

The system of pre-accelerators (Figure 2.2) is used to accelerate particles close to the speed of light. Protons extracted from hydrogen gas are first subjected to Linear Accelerator (LINAC 2 [67]) where the energy of bunches reach up to 50 MeV. In the second stage, protons are accelerated to 1.4 GeV in the Proton Synchrotron Booster (PSB [68]). Subsequently, in the Proton Synchrotron (PS [69]), protons are accelerated to 26 GeV where they are passed to the Super Proton Synchrotron (SPS [70]) which accelerates protons to 450 GeV. After this chain of pre-accelerations, protons are ready for an injection into the main ring of the LHC.

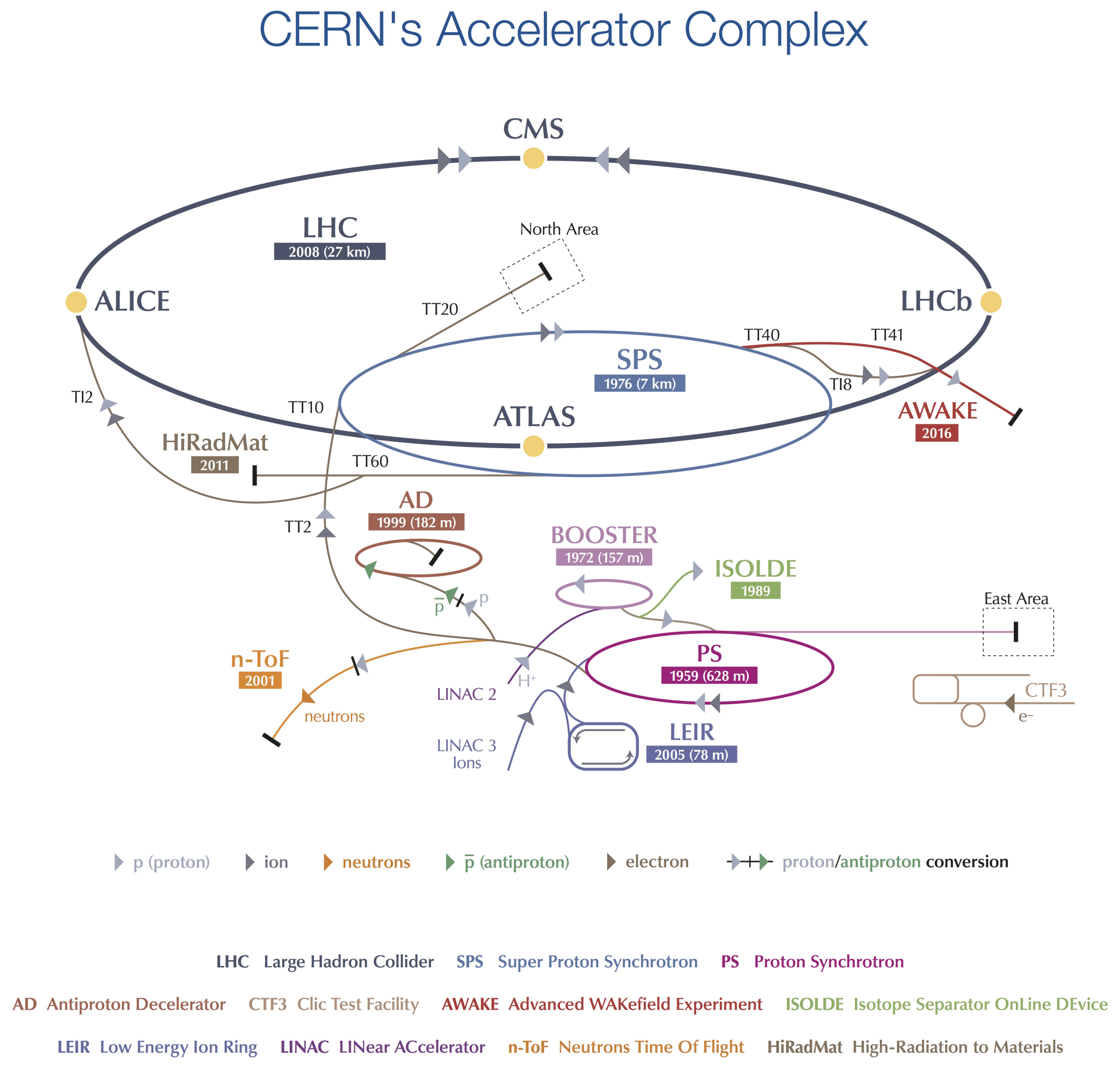

Figure 2.2: Top view scheme of the CERN's accelerator complex [71].

When a beam enters the main ring of the LHC, under the optimal conditions that allows the highest efficiency providing maximum values, it consists of about 2800 bunches of 1.15×10^{11} protons in each bunch, with the spacing of 25 ns between the bunches. The nominal energy of collisions is equal to 7 TeV with the total centre-of-mass energy being equal to 14 TeV. The LHC has never before worked at 14 TeV hence the mentioned values are the designed parameters. Such energy is expected to be delivered during the LHC Run III (2022-2024) which is about to commence in. The bunch collisions rate operates at 40 MHz and the luminosity peak equals to 2×10^{34} cm^{-2}s^{-1}. The speed of protons, which is equal almost to the speed of light, generates 11245 number of turns and 600 millions collisions per second. The average lifetime of a beam equals to 10 h.

2.2 LHCb Detector

2.2.1 Overview

The LHCb detector is a single-arm spectrometer. The coordinate system is defined as the z-coordinate along the beam line, the y-coordinate in the vertical direction and x-coordinate in the horizontal direction. The x-coordinate is used for maintenance and assembly purposes. A design strategy closely follows needs coming from the main purpose of the experiment, which is the study of bottom and charm hadrons. The b and c quarks are mostly produced due to the gluon-fusion production of $b\bar{b}$ and $c\bar{c}$ pairs along the beam axis. The geometrical acceptance covers the optimal range of b-hadron decays. In the vertical plane (bending plane) it is 10-250 mrad whereas in the horizontal plane (non-bending plane) 10-300 mrad. Another measure widely used is the pseudorapidity, which is defined as:

$$\eta = -\ln[\tan(\frac{\theta}{2})], \tag{2.1}$$

where θ is an angle between the positive direction of the beam axis and a particle momentum. For the LHCb detector, the pseudorapidity range for the particles in the LHCb geometrical acceptance lies between $1.8 < \eta < 4.9$. Figure 2.3 represents the $b\bar{b}$ pair production as a function of an angle and the pseudorapidity.

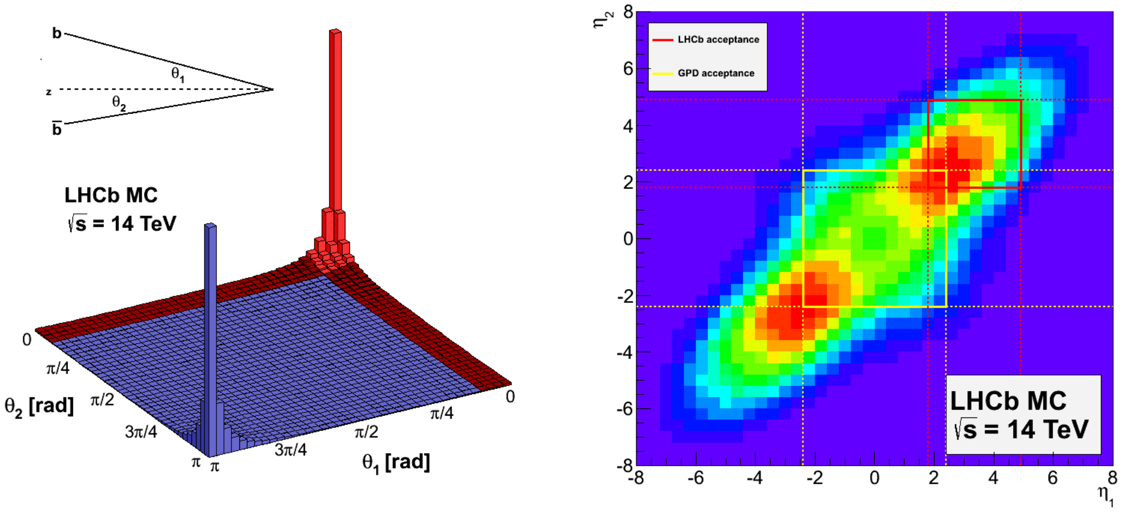

Figure 2.3: The $b\bar{b}$ pair production as a function of an angle (left) and the pseudorapidity (right) where the LHCb acceptance is marked with a red color [72].

The performance of the LHCb detector depends on two main parameters: the luminosity and the pile-up. The luminosity measures the ability of an accelerator to produce the relevant number of interactions in a unit of time and is defined as the proportionality factor between the number of events recorded in a specific time interval and the interaction cross section. The pile-up is the average number of pp interactions in visible events. The LHCb luminosity is lower in comparison to the luminosity of general purpose experiments, which use the full luminosity of $2 \times 10^{34}\ cm^{-2}s^{-1}$ provided by the LHC. In the case of the LHCb, running with maximum luminosity would not result in the gain in experimental precision due to the associated difficulties with e.g. trigger and pile up (see below). The LHCb detector is designed for the study of b- and c-hadron decays thus it is essential to precisely reconstruct the decay chain. It is crucial to correctly recognize geometrically, with high resolution, the primary and the secondary vertex between many vertices in a particular event and to efficiently reconstruct the trajectories of particles. A lower luminosity causes a decrease in the number of collisions that are registered simultaneously (so-called pile-up), which improves the overall conditions for particle and vertex reconstruction.

Historically, the initial value of the luminosity and the pile-up in 2010 was around 10^{28} $cm^{-2}s^{-1}$ and zero, respectively. During the LHC Run I (2010-2013), in the years 2010-2011, the luminosity increased to 3.5×10^{32} $\mathrm{cm^{-2}s^{-1}}$ while the pile-up raised to around 2.5 at the beam energy of 3.5 TeV, thus exceeding the design luminosity of the LHCb detector. At this point, the luminosity levelling technique was introduced which keeps the instantaneous luminosity constant during a particular LHC fill, in spite of lessening the intensity of beams. This procedure is achieved by shifting the beams with respect to each other by adjusting the optics accordingly. The transversal beam overlap can be adjusted in the maximum range of 5% for 15 hours. Such operation allows to maintain the same trigger configuration throughout a fill. Figure 2.4 shows a result of the luminosity levelling in comparison to the ATLAS and the CMS. In 2012, the luminosity of 4×10^{32} $cm^{-2}s^{-1}$ was achieved at the beam energy of 4 TeV making the luminosity twice the design value. Since then, the luminosity has not changed and continued during the LHC Run II (2015-2018). Over that time, the centre-of-mass energy increased to 13 TeV. Figure 2.5 presents an overview of the acquired integrated luminosity throughout the operation of the LHCb, where over 9 $\mathrm{fb^{-1}}$ was collected in total. During the second Long Shutdown (LS2) of the LHC (2019-2021), the LHCb detector undergoes specific upgrades that will improve the instantaneous luminosity to 2×10^{33} $cm^{-2}s^{-1}$ together with the data acquisition read-out rate of 40 MHz for the LHC Run III (2022-2024) at the beam energy of 7 TeV. More details concerning the upgrade of the LHCb detector are provided in Section 2.3.

A cross-section of the LHCb detector is presented in Figure 2.6. The LHCb spectrometer is composed of multiple components and subdetectors. Starting from the components shown on the left side of Figure 2.6:

- The Vertex Locator (VELO) detector is a silicon strip vertex tracker, built around the beam's intersection point. It determines, with a high precision, the primary interaction vertex and decay vertices of particles.

- The first Ring-Imaging Cherenkov (RICH1) detector placed behind the VELO. It is used for the identification of charged hadrons in the (1-60) GeV/c momentum range.

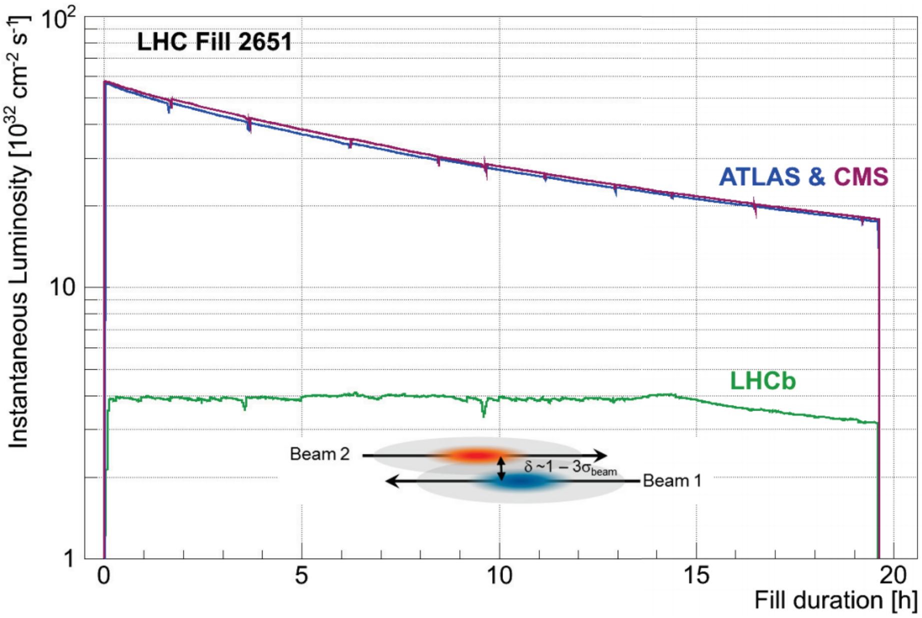

Figure 2.4: Instantaneous luminosity over time during an LHC fill for the LHCb, ATLAS and CMS [73].

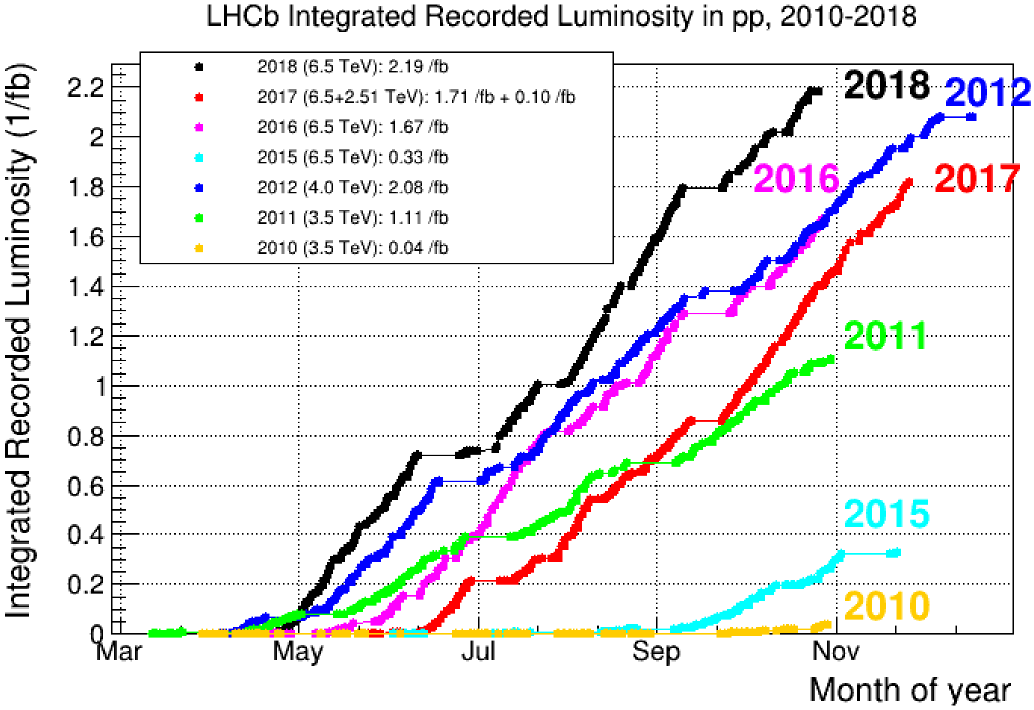

Figure 2.5: A chart representing the integrated luminosity collected at the LHCb in the years 2010-2018 [74].

- The magnet, which is a warm dipole magnet, providing the integrated field of 4 Tm that deflects charged hadrons in the horizontal plane.
- The Tracker Turicensis (TT) is a silicon strip detector used for a trajectory detection of charged particles. The tracking station is placed between the RICH1 and the magnet.
- Three stations, called T-Stations, of silicon strip detectors located behind the magnet. Each of the tracking station includes two subdetectors: the Inner Tracker (IT), which is a silicon strip detector, and the Outer Tracker (OT), which is a drift-tube gas detector.
- The second Ring-Imaging Cherenkov (RICH2) detector located behind the main tracker. Similarly to the RICH1, it is used for the identification of particles, but it covers a different momentum range, that is (15-100) GeV/c.
- The Scintillating Pad Detector (SPD) and the Preshower (PS) are used to help the calorimetry system on the requirement of good background rejection together with the detection of photons and the electron identification.
- The calorimetry system composed of the electromagnetic calorimeter (ECAL) and the hadronic calorimeter (HCAL). It measures the energy of photons, electrons and hadrons together with their spatial coordinates deposited by electromagnetic and hadronic showers. In addition, it provides information concerning the hardware trigger.
- The muon system consisting of 5 muon stations referred as M1, M2, M3, M4 and M5. It is used for the muon identification, as only these particles are able to reach up to this region. M1 is also used for the hardware trigger.

The detectors are symmetric along the x-coordinate. The sides are referred either as A-side or C-side.

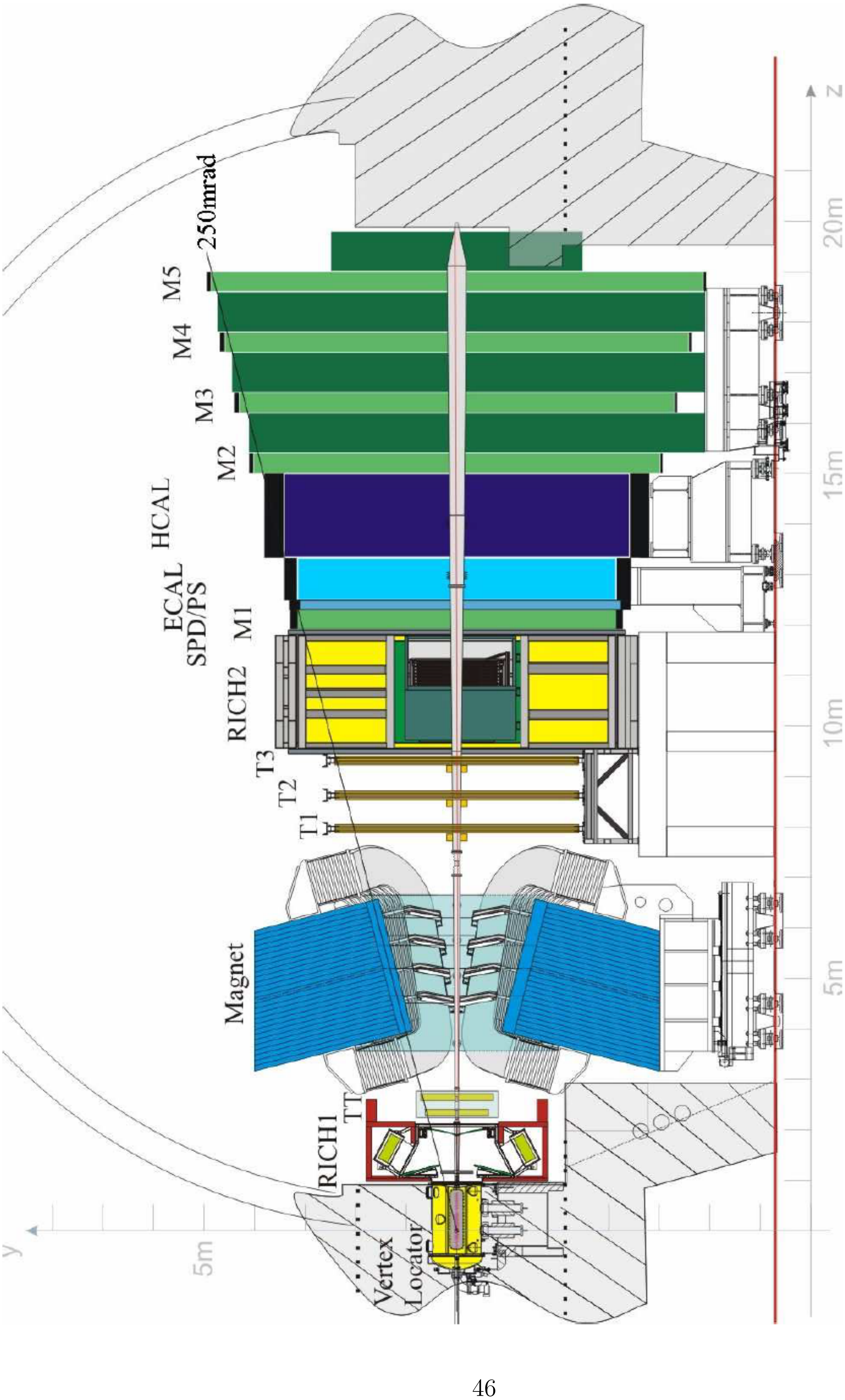

Figure 2.6: A cross-section of the current LHCb detector [62].

2.2.2 Tracking System

The LHCb tracking system is responsible for the reconstruction of the trajectories of charged particles passing through the detector. The trajectories are measured using the information coming from the VELO and the TT detectors placed downwards the magnet, and T-Stations situated upwards the magnet. Charged particles are bent in the magnetic field of the dipole magnet allowing measurements of particle's properties such as charge and momentum.

2.2.2.1 Dipole Magnet

A warm dipole magnet is used to bend a charged particle in order to determine its momentum, based on the deflection of particle's trajectory. The magnet is a non-superconductive dipole magnet with a magnetic field of 4 Tm in the y-axis. It is made of two saddle-shaped coils, mounted symmetrically on an iron frame in the span of 10 m, that are inclined by a small angle with respect to the beam axis, as shown in Figure 2.7 (left). To acquire accurate estimation of the momentum of a particle, the magnet is calibrated to 10^{-4} of relative precision. Particles passing along the z-axis are bent in the xz-plane. To reduce the detector charge asymmetry, the direction of the magnetic field can be swapped, as the polarity can be adjusted either upwards or downwards along the y-axis as shown in Figure 2.7 (right).

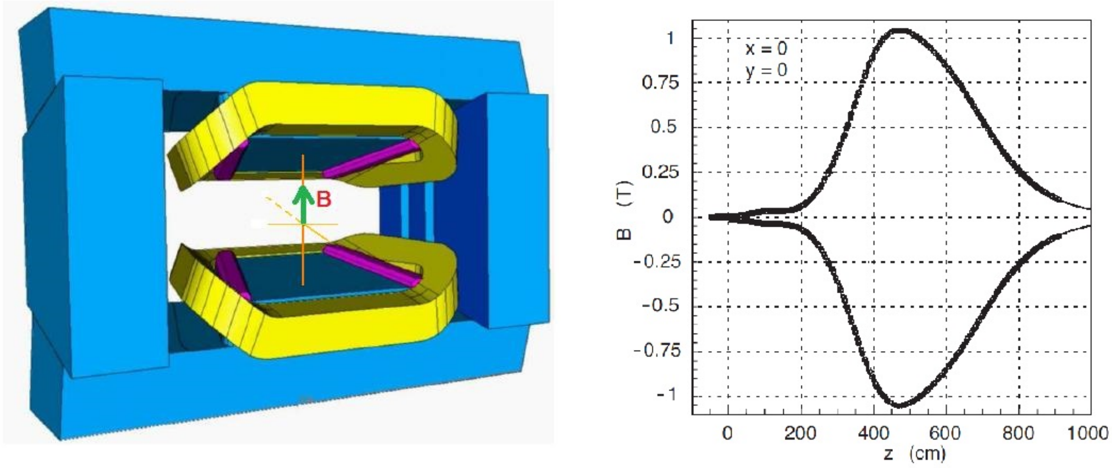

Figure 2.7: On the left side, a scheme of the LHCb dipole magnet is depicted. On the right side, the polarity of the magnetic field is presented, with the positive and negative curve referring to the downward and upward polarity, respectively [62].

2.2.2.2 Vertex Locator Detector

The VELO [75] is a silicon strip detector located as close as possible to the *pp* interaction point. The main responsibility of the subdetector is to measure precisely the trajectories of charged particles in that particular region and position of the *pp* interaction point. The accurate estimation of the track position measurements allows to distinct the locations of primary vertices, which are the results of *pp* collisions, from the secondary displaced vertices. The latter are attributed due to short lived particle decays which are typical for the particles containing b and c quarks.

The VELO is composed of two movable halves where each halve contains 21 half-circular modules of silicon strip sensors. The modules are arranged perpendicularly along the beam axis, as shown in Figure 2.8.

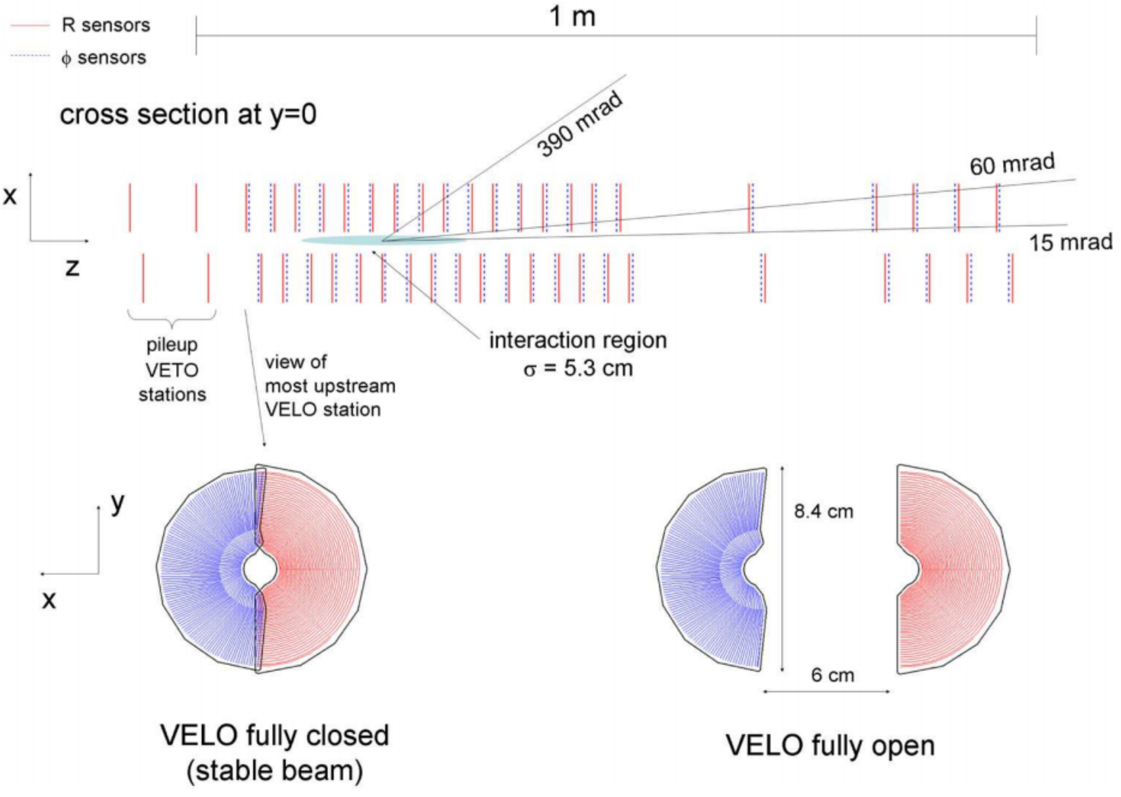

Figure 2.8: In the upper part, a scheme of the VELO sensors along the beam axis in the xz-plane is presented. In the lower part, the R- (blue) and the ϕ- (red) sensors in two configurations are shown [62].

Each module includes two different types of silicon micro-strip sensors placed on opposite sides. Each sensor consists of 2048 strips built on top of 300 μm silicon bulk for charge collection. The R-sensors are responsible for the measurements of the radial coordinate R from the beam axis. They are segmented in semi-circular strips divided into four 45° regions to reduce the occupancy. Each region contains 512 strips in the form of arcs with the approximate pitch range from 40 to 100 μm. The ϕ-sensors are used to determine the azimuthal angle ϕ, that is defined as the angle between the x-axis and a direction vector in xy-plane. Similarly to the R-sensors, in order to reduce the occupancy, the ϕ-sensors are divided into two regions. The inner one contains 683 strips while the outer one includes 1365 strips. A scheme of R- and ϕ-sensors is presented in Figure 2.9.

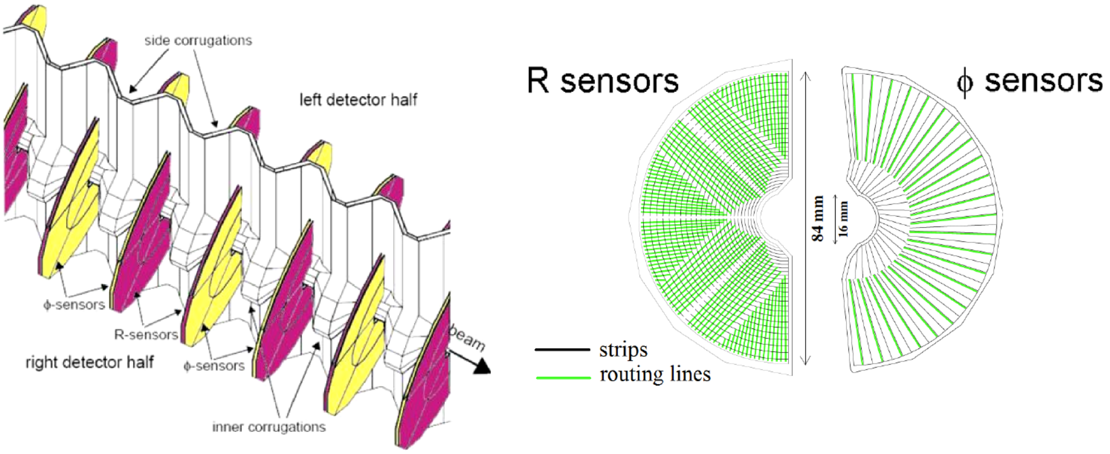

Figure 2.9: On the left, a closed configuration is presented while on the right, a geometry of the R- and the ϕ- sensors is illustrated [62].

During the data taking, the VELO is located extremely close to the beam axis, which is approximately 8.4 mm. However, during the injection of the proton beam and the ramp-up, the beam is unstable. In order to prevent any high absorption of the radiation damage, two halves of the detector are movable allowing to retreat the halves by around 3 cm, reaching the safe distance from the beam. When a beam is considered stable, the movable halves come back to the initial position.

2.2.2.3 Tracker Turicensis

The TT [76] is a silicon strip detector used to detect low-momentum particles and to reconstruct long-lived particles. The detector is divided into two stations, called TTa and TTb, that are separated by 30 cm along the beam axis. They are located upstream of the dipole magnet of about 2.5 m after the interaction region. Each station has two planar layers with approximate dimensions of about 150 cm in width and 130 cm in height, making a detection area close to 8.4 m^2, as shown in Figure 2.10. The layers between the stations are organised differently. For the TTa, the strips are arranged in the x- and u- layers whereas for the TTb, the strips are organized in the v- and x- layers. The strips of the outer layers (x) are aligned with the y-axis while for the inner layers (u and v), the strips are rotated by a stereo-angle of $-5°$ and $+5°$ respectively. The x-u-v-x layout arrangement allows a tracks reconstruction in 3-dimension through a stereo view. The strip pitch equals to 183 μm and a hit resolution to 50 μm.

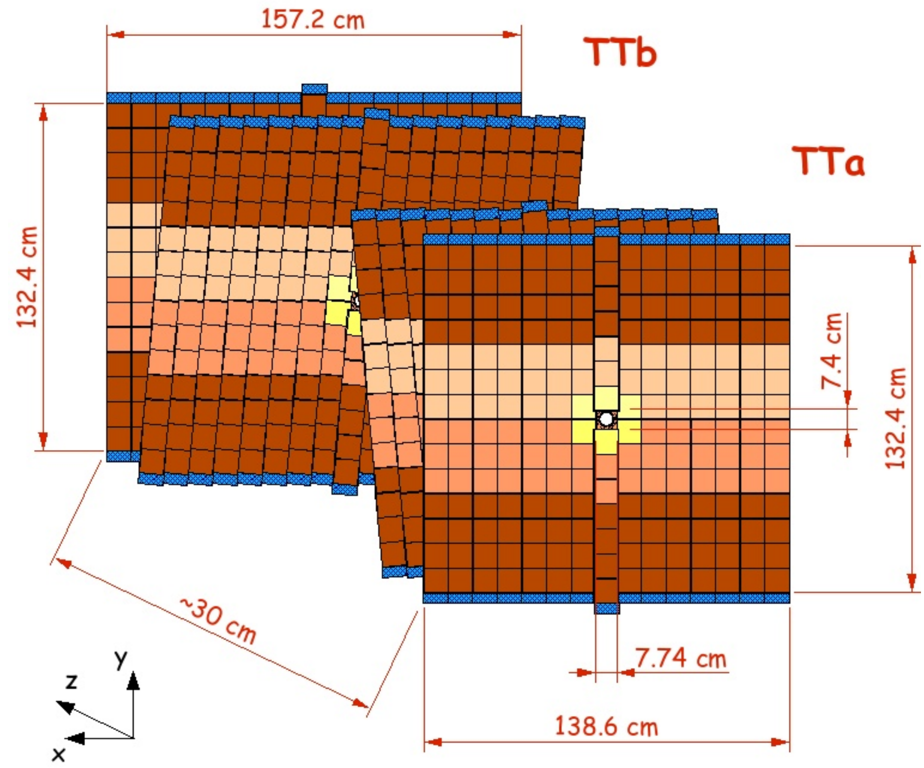

Figure 2.10: A scheme representing a geometry of the TT detector [77].

2.2.2.4 T-Stations

The T-Stations, located downstream of the dipole magnet, comprise the three tracking stations, referred as T1, T2 and T3, used to measure the momentum of charged particles. Each of the station is divided into two subdetectors named the IT and the OT.

The IT [76] is mounted in the central region of each T-station covering the regions closest to the beam axis, where the particle density is the highest. Although the IT covers less than 2% of the LHCb acceptance, it is responsible for the detection of 20% tracks acquired from *pp* collisions. It is made of silicon micro-strip sensors with the technology similar to the TT. The IT consists of four planar layers, with the same layout configuration as the TT (x, u, v, x), where two middle layers are rotated in stereo-angle by $-5°$ and $+5°$. The subdetector is arranged in four boxes: left (ASide), top, right (CSide) and bottom, as presented in Figure 2.11. The sensors in the left and the right box use silicon thickness of 410 μm while in the top and the bottom 320 μm. The strip pitch is approximately 193 μm making a hit resolution 50 μm, similarly to the TT.

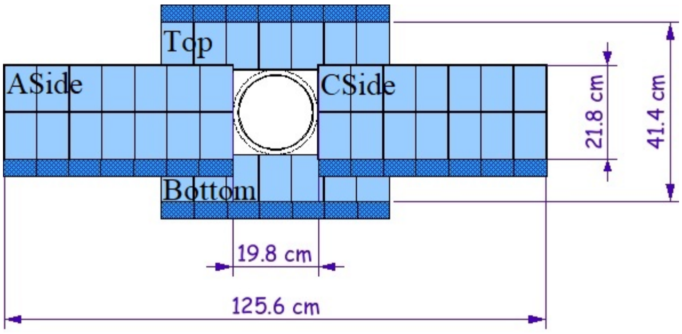

Figure 2.11: A front view of the x-layer of the IT detector. The light-blue region refers to the detector modules while dark-blue region represents the read-out electronics [77].

The OT [78] consists of drift-straw tubes surrounding the IT and covers the remaining LHCb acceptance. The subdetector consists of an array of gaseous straw-tube modules with drift-time read-out, where each module contains a double layer of drift-tubes. The gas used in the straw-tubes is a combination of 70% Argon, 27.5% CO_2 and 1.5% O_2 that allows to achieve a spatial resolution of 200 μm and a drift time below 50 ns. Exactly as in the TT and the IT, the OT follows the same layout arrangement: x, u, v, x. The geometry of the OT and straw tubes structure is presented in Figure 2.12. The drift tubes are equal to 2.4 m with an inner diameter of 4.9 mm.

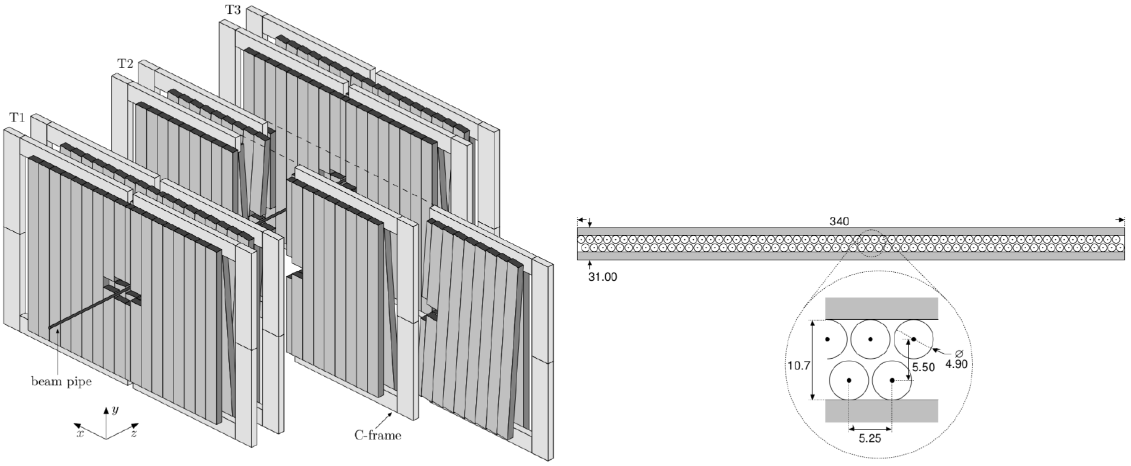

Figure 2.12: On the left side, the double layer of drift-tubes structure is presented. On the right side, a cross-section of a single OT detection plane is shown, depicting the straw-tube structure [78].

2.2.3 Particle Identification System

The LHCb Particle Identification (PID) system is responsible for proper identification of particles. The system consists of the following detectors: the RICH detectors, the calorimetry system and the muon system.

2.2.3.1 RICH Detectors

The RICH detectors [79] are placed downstream and upstream of the dipole magnet. The detectors are used for the proton, kaon and pion identification. The RICH1 detector, shown in Figure 2.13 (left), is located upstream of the dipole magnet and is used for the identification of low-momentum particles, specifically from ∼1 to 60 GeV/c over the full LHCb angular acceptance (from ±25 to ±300 mrad and ±25 to ±250 mrad along the horizontal and vertical direction, respectively). The RICH2 detector, demonstrated in Figure 2.13 (right), is placed downstream of the magnet and is used for the identification of higher-momentum particles, strictly speaking from ∼15 to 100 GeV/c over the limited angular acceptance (from ∼±15 to ±120 mrad and ±15 to ±100 mrad in the horizontal and vertical direction, respectively). A detailed description of the current system of the RICH detectors is presented in Section 3.2.

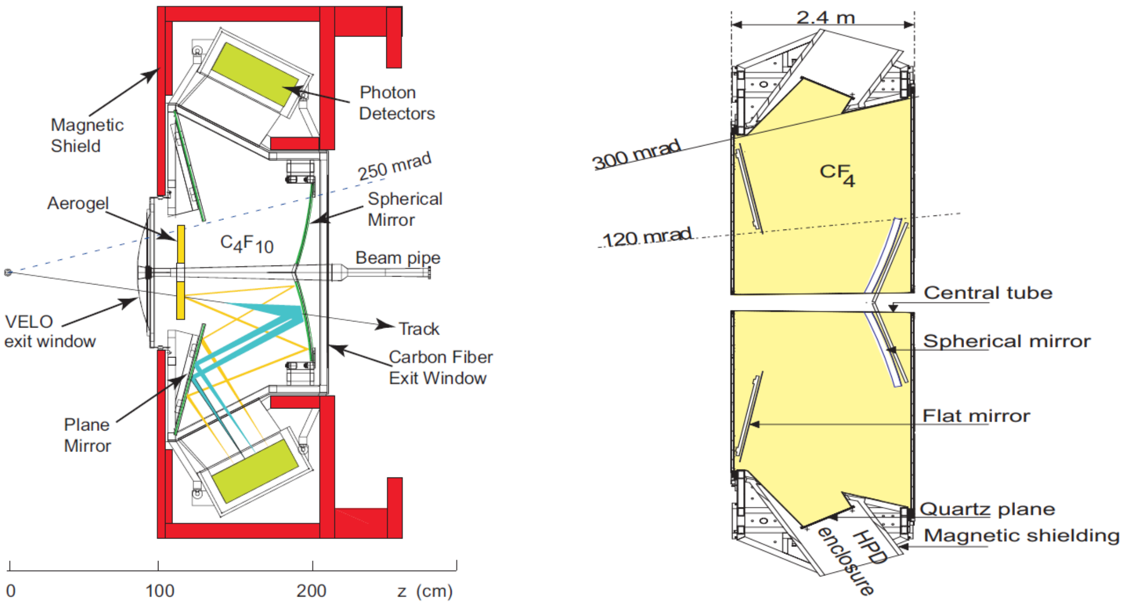

Figure 2.13: A top view scheme of the RICH1 (left) and RICH2 (right) [62].

2.2.3.2 Calorimeter Detectors

The calorimetry system [80] is responsible for the measurements of deposited energy of electrons, photons and hadrons. Moreover, it plays an important role in the first level trigger. The system (Figure 2.14) is composed of four sub-calorimeters:

- Scintillating Pad Detector (SPD),
- Preshower (PS),
- Electromagnetic Calorimeter (ECAL),
- Hadronic Calorimeter (HCAL).

The SPD [81] is positioned behind the first muon station (M1) and its role is to distinguish charged particles from neutral particles. The PS [81] is a subsequent detector that separates photons from neutral hadrons. Between these detectors, a 15 mm thick lead absorber is located that corresponds to ∼2.5 radiation lengths for electrons. Subsequently, the ECAL is used to measure deposited energy of electrons and photons. It is made of 4 mm thick scintillator tiles and 2 mm thick lead plates. The thickness corresponds to ∼25 radiation lengths that ensures electromagnetic shower containment with a good resolution. At the end, the HCAL is used to measure the energy of hadronic showers and in addition, is used as the hardware trigger for particles with high transverse energy which are typical for events containing b or c quarks. It is made of 4 mm thick scintillator tiles and 16 mm thick iron plates that corresponds to ∼5.6 interaction lengths.

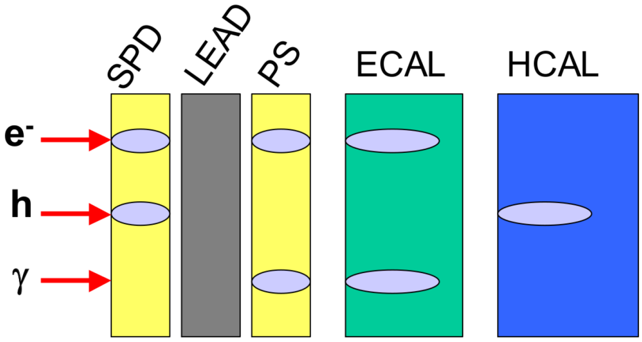

Figure 2.14: A scheme of the energy deposit for each sub-calorimeter [81].

The SPD, PS and ECAL use the same geometrical layout as presented on the left side of Figure 2.15. The dimensions that are used are 4×4 cm^2 in the inner region, 6×6 cm^2 in the middle region and 12×12 cm^2 in the outer region. The division is performed to manage the increasing occupancy near the beam axis. The HCAL uses layout divided into two section of 13×13 cm^2 and 26×26 cm^2 corresponding to the inner and outer region, respectively, as shown on the right side of Figure 2.15.

2.2.3.3 Muon Detectors

The muon detection system [82] is used for the identification of muons and provides low level triggering information of hadron decays containing muons in the final state. The system consists of five rectangular stations (M1-M5) as presented in Figure 2.16.

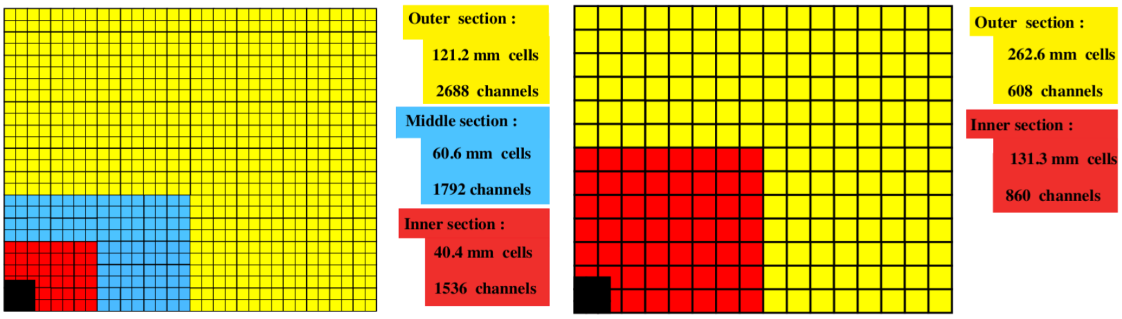

Figure 2.15: A segmentation of the SPD, PS and ECAL (left) and HCAL (right) [62].

The M1 chamber, located in the highest particle flux region - upstream of the calorimeters, is built of triple Gas Electron Multiplier (GEM) detectors and is used for the trigger measurements of p_T. The M2-M4 chambers, placed downstream of the calorimeters, are built of Multi Wire Proportional Chambers (MWPC). Between them, 80 cm thick iron absorbers are installed to filter out all particles except penetrating muons. In order for muons to cross over all the five muon chambers, their momentum needs to be at least 6 GeV/c.

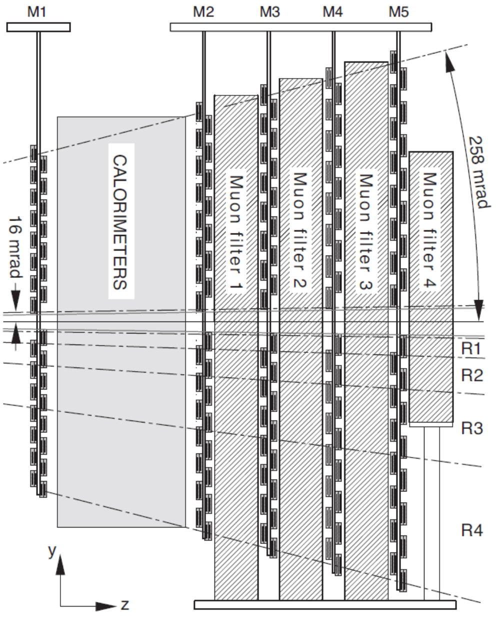

Figure 2.16: A side view of the muon system [62].

2.2.4 Trigger System

The trigger system [83] is responsible for the selection of events that are are essential in a perspective of the LHCb experiment. The multi-level trigger system allows to reject events of no interest and select events containing *b*- and *c*-hadron decays. The LHCb trigger system consists of two levels: Level-0 (L0) and High Level Trigger (HLT) that is divided into High Level Trigger 1 (HLT1) and High Level Trigger 2 (HLT2). The workflow of the trigger system can be followed in Figure 2.17.

2.2.4.1 Level-0 Trigger

The hardware-based L0 trigger reduces the event rate from 40 MHz to the maximum read-out rate of the LHCb detector which is around 1.1 MHz. The L0 consists of three sub-systems: the L0-Calorimeter trigger, the L0-Muon trigger and the L0-PileUp trigger. The measurements are acquired from the calorimetry system (PS, SPD, ECAL and HCAL) and the muon system (M1-M5 stations). Only events with high momenta and transverse energies are accepted. The information from the pile-up system in used to veto events with high background activity indicating multiple interactions.

2.2.4.2 High Level Trigger

The software-based HLT, written in C++ and python programming languages, processes the events fulfilling the L0 trigger. The HLT1 performs a partial event reconstruction online of the trajectories of charged particles going through the full LHCb tracking system, called long tracks, with p_T greater than 500 MeV/c. The data is then buffered into local disks that is read by the second trigger named HLT2 which fully reconstructs the events at the rate of 12.5 kHz (Run II). Between the stages a full real-time calibration and alignment is performed. Although the selection and reconstruction of events are produced online, the quality is comparable as they would be produced offline.

2.3 LHCb Upgrade

During the scheduled LS2 started in 2019, the LHCb detector is undergoing a major modernization [85] to be operable for the LHC Run III, that is expected to start at

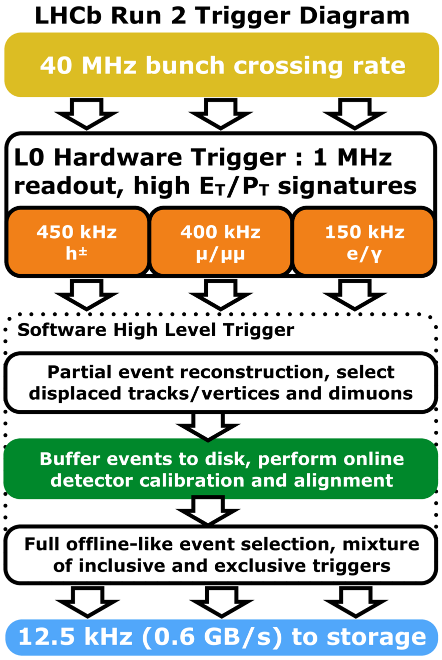

Figure 2.17: A dataflow diagram of the LHCb trigger for the Run II [84].

the beginning of 2022.

2.3.1 Overview

The implementation of cutting-edge technology and the replacement of older detectors that were exposed to the radiation damage leads to substantial increase in overall performance of the LHCb spectrometer. Most of the components and the sub-systems are replaced to improve two crucial parameters of the detector: the instantaneous luminosity and the bunch-crossing read-out rate. The instantaneous luminosity is going to be increased to $2 \times 10^{33}\ cm^{-2}s^{-1}$, which is five times more than the average value achieved in the LHCb experiment in the Run II. For the Run III and IV, the detector is planned to collect around 50 fb^{-1} of the integrated luminosity, which is ten times more than it has been collected so far since the initialisation of the operation of the detector. A new design of the LHCb detector is presented in Figure 2.18

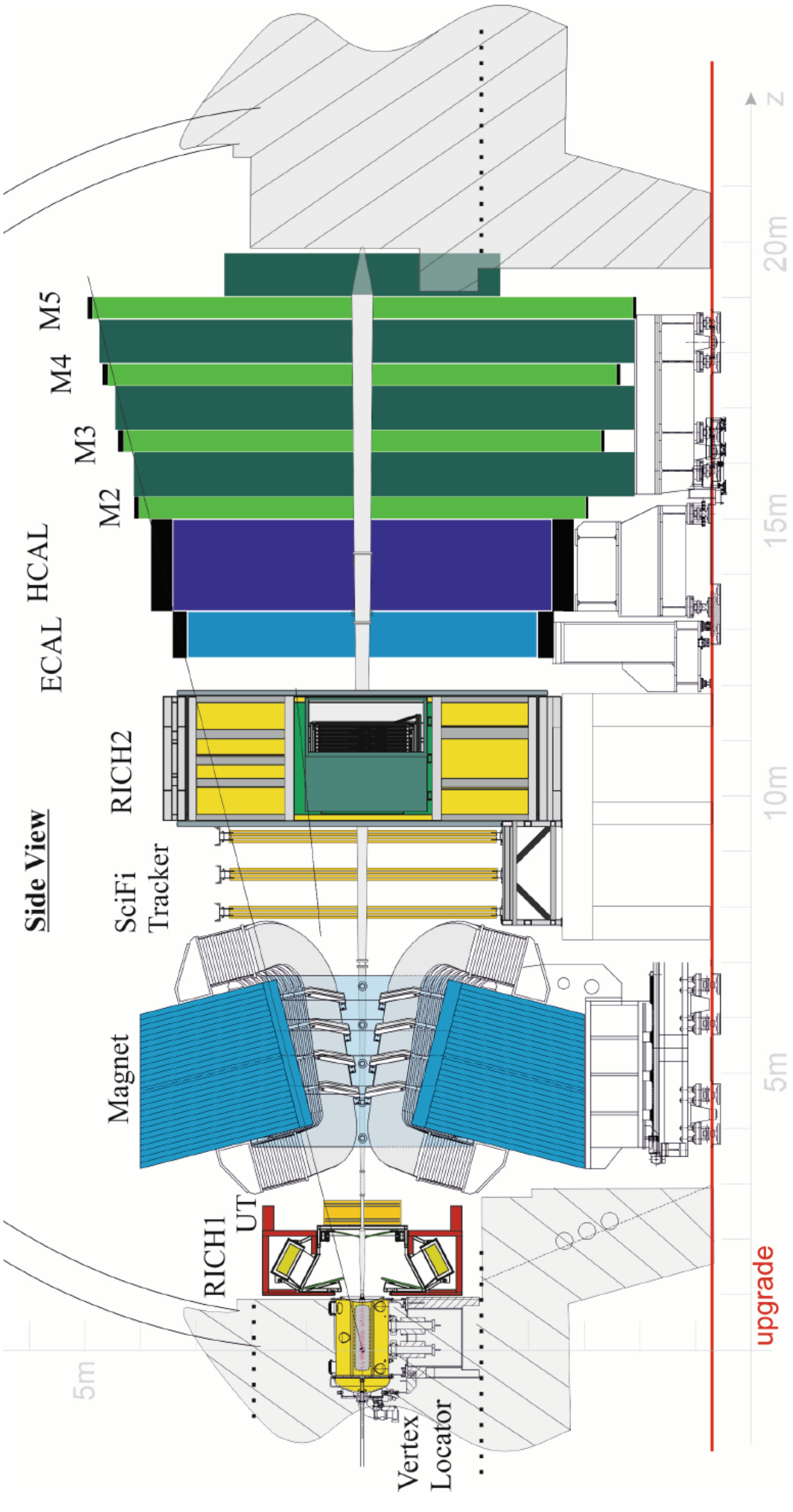

Figure 2.18: A cross-section of the upgraded LHCb detector [85].

2.3.2 Trigger System

The L0 hardware trigger, that is bottlenecking the read-out capability to 1.1 MHz, is going to be removed completely [86], thus the full event rate of 40 MHz delivered by the LHC is going to be achieved. All the front-end electronics that do not support the 40 MHz read-out are going to be replaced or upgraded to satisfy this requirement. The L0 trigger will be replaced by a fully software-based HLT trigger, that will perform a full reconstruction of events at the LHC inelastic event rate of 30 MHz. A workflow of the upgraded LHCb trigger is presented in Figure 2.19.

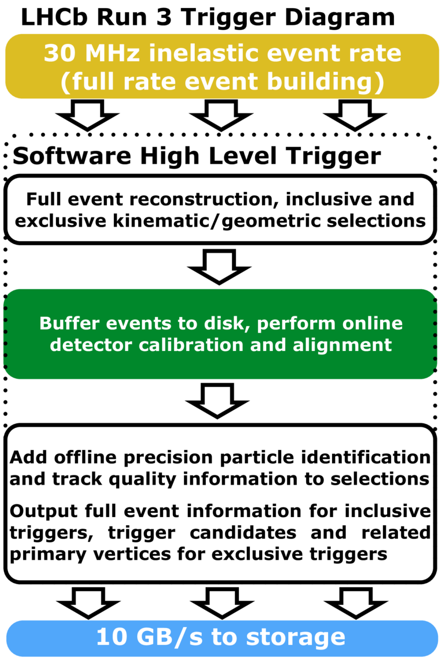

Figure 2.19: A dataflow diagram of the upgraded LHCb trigger for the Run III [84].

2.3.3 Tracking System

The current VELO, based on the silicon micro-strips technology, is replaced by 26 rectangular tracking sensors (Figure 2.20) based on 50×50 μm^2 pixel technology that enhances a hit resolution and simplifies the track reconstructions. The new VELO [87] is positioned 3.3 mm closer to the beam axis (from 8.4 mm to 5.1 mm). The incoming particles pass through less detector material as the aluminum cover and sensors are much thinner. Due to the upgrade, the detector material decreases from

4.6% to 1.7% radiation lengths. These improvements increase the impact parameter resolution by about 40%. The sensors operate at the temperature of −20°C and are cooled by micro-channel CO_2 cooling technology. As the sensors are positioned closer to the beam at the higher luminosity, the detectors are designed to withstand higher radiation damage.

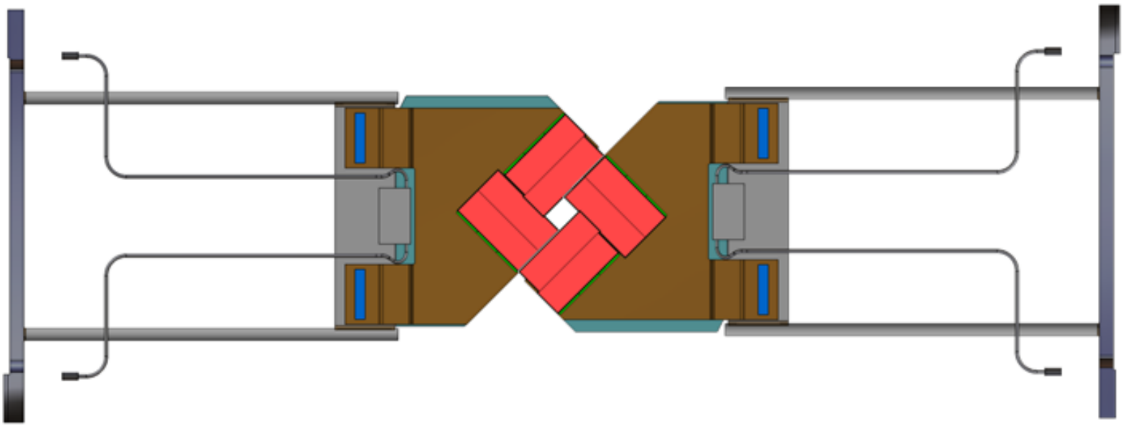

Figure 2.20: A scheme of the upgraded closed VELO modules [88].

The TT detector is replaced completely as the TT sensors would not bear higher radiation dose expected for the LHC Run III. In addition, the occupancy would be too high as the TT is not designed to work at the read-out rate of 40 MHz. The new detector, that is going to be implemented, is called the Upstream Tracker (UT) [89]. The detector enables reconstruction of long lived particles decaying after the VELO. The UT contains 4 tracking layers (Figure 2.21) based on the silicon-strip technology, placed vertically, as the tracks are bent horizontally by the magnet. The x-u-v-x layout arrangement, with u and v being rotated by -5° and $+5^\circ$ respectively, does not change. The geometrical acceptance is increased as the inner sensors are positioned closer to the beam axis in comparison to the TT. The geometry, segmentation and the technology of the sensors are designed by the foreseen particle occupancy and the radiation dose. For the outer region, the strips of 99.5 mm long with 180 μm pitch are introduced based on n^+-in-p technology to deal with higher radiation dose. For the region close to the beam, the strips of 51.5 mm long with 95 μm pitch are used in the same n^+-in-p technology.

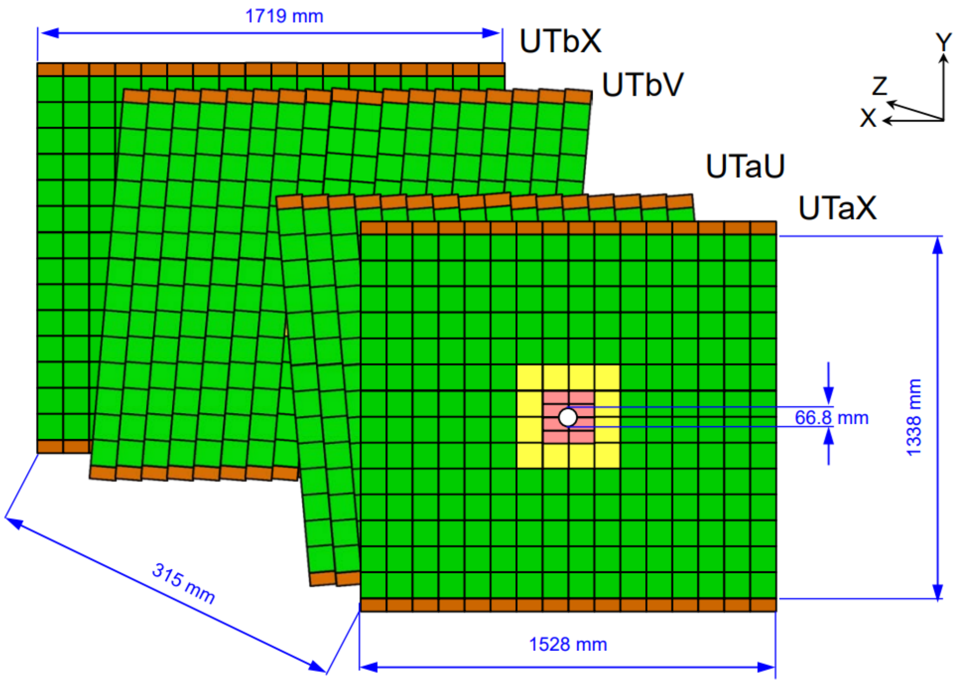

Figure 2.21: A scheme of the UT geometry from the downstream perspective [89].

Similarly to the TT detector, the T-stations comprising the IT and OT, would not handle higher radiation dose and would not operate in the upgraded read-out range. For this reason, the T-stations are replaced by the newly developed Scintillating Fiber (SciFi) [89] tracker, presented in Figure 2.22. The SciFi detector includes 12 detector layers for track reconstruction after the magnet to measure the momentum of particles. The same number of stations is used (T1, T2 and T3) and each of them includes 4 detection layers. The stations are positioned vertically, in the same way as the OT, with gaps of 20 mm between the layers. The beam pipe goes through a hole in the center of the layers. The layers are arranged in the same x-u-v-x configuration where u and v are rotated by $-5°$ and $+5°$, respectively. Each layer contains 12 modules. The SciFi is based on 2.4 m long plastic scintillating fibres. The diameter of the fibers equals to 250 μm arranged vertically. Each of the detector layer is made of 6 sub-layers of fibres with the thickness of 1.35 mm and the approximate area of 6×5 m^2. The fibers are read-out by Silicon PhotoMultplier (SiPM) detectors located on the top and bottom of the detector layers. The SiPMs are cooled to the temperature of $-40°$C to minimize the radiation effects and dark counts.

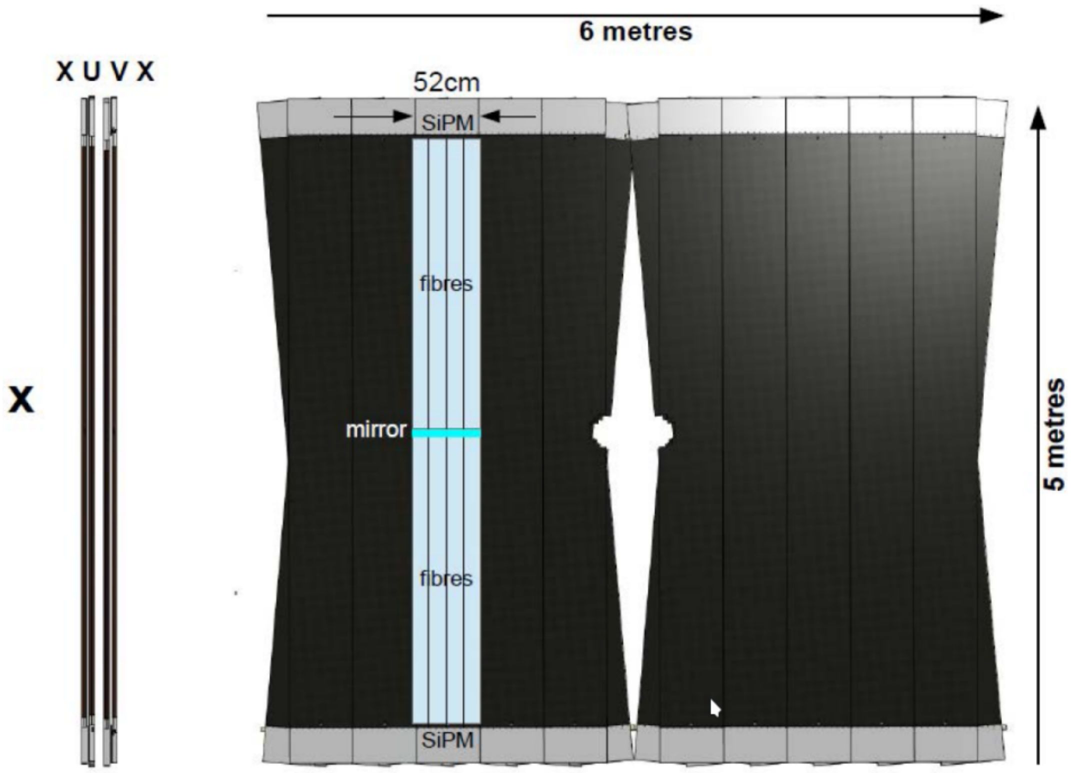

Figure 2.22: A scheme of the yz- and xy-view of one of a SciFi station. [90].

2.3.4 Particle Identification System

The RICH detectors undergo substantial upgrade [91]. For the RICH1 detector, the optimization in optics is introduced by the focal length increase of mirrors to handle higher particle occupancy. In addition, the redesign of mechanics takes place, such as new support and cooling implementation. For both RICH detectors, the current Hybrid Photon Detectors, operating at 1.1 MHz, are replaced by Elementary Cells that are designed for 40 MHz read-out rate. A thorough discussion of the upgrade of the RICH detectors is presented in Section 3.2.

The calorimetry system and the muon system undertake upgrade on their front-end electronics to meet the 40 MHz read-out rate requirement. As the L0 trigger system is no longer needed, the PS, SPD and M1 detector are completely removed.

Chapter 3

LHCb RICH Detection System

The following chapter focuses on the LHCb RICH detectors. At first, a theoretical introduction to Cherenkov radiation is presented which is followed by the discussion of the RICH detection system with a great emphasis put on its upgrade.

3.1 Cherenkov Radiation

The Cherenkov effect takes place when a charged particle travels inside a dielectric medium, of refractive index n, with a velocity higher than the speed of light in that medium. A charged particle passing through a medium, stimulates electrons of nearby atoms to excited states due to electric field. When the electrons come back to the ground state, the energy is emitted as photons (Cherenkov photons) of electromagnetic radiation (Cherenkov radiation [92]). A particle needs to have a velocity v greater than phase velocity v_p which is defined as the ratio between the speed of light in vacuum c and the medium refractive index n:

$$v_p = \frac{c}{n}. \tag{3.1}$$

Wave propagation, according to Huygens principle [93], is spherical. The emitted spherical waves, travelling at the speed of light in that medium, do not catch up a faster moving particle. The waves line up consecutively to a cone relatively to the direction of the propagation of a charged particle. Figure 3.1 presents a scheme illustrating the creation of Cherenkov radiation. The shape of a cone can take 3 forms: straight line (particle at constant velocity), concave (particle accelerating) or convex (particle decelerating). A particle moving at a constant velocity is characterised by the Cherenkov angle θ:

$$\cos\theta = \frac{v_p}{v} = \frac{1}{\beta n}, \tag{3.2}$$

where β is a ratio between the velocity of a particle and the speed of light:

$$\beta = \frac{v}{c}. \tag{3.3}$$

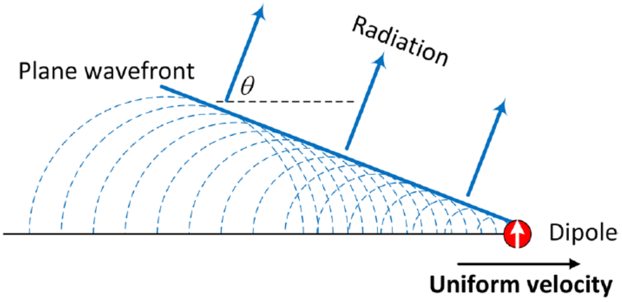

Figure 3.1: Schematic illustration of Cherenkov radiation induced by a charged particle at a constant velocity [94].

The Cherenkov angle informs about particle's speed. If a particle travels near the speed of light, the angle is low (tends to 0°) which makes the cone thick. On the other hand, when a particle is moving much faster than the speed of light, the angle is high (tends to a right angle) which makes the cone thin. By combining Cherenkov angle with the particle's momentum:

$$\cos\theta = \frac{1}{n}\sqrt{\left(\frac{m}{p}\right)^2 + 1}, \tag{3.4}$$

it is possible to determine the mass of a particle:

$$m = p\sqrt{n^2\cos^2\theta - 1}. \tag{3.5}$$

The Cherenkov angle θ is measured by Cherenkov detectors while a particle's momentum p is determined by the tracking system. Combining this information with the refractive index $n = \frac{c}{v_p}$ of a particular medium, a particle's mass can be calculated. In Figure 3.2, the Cherenkov angle depending on the momentum of tracks is presented. As shown in the graph, different particles (muons, pions, kaons and protons) have different characteristics, which allows for their precise identification. The Cherenkov effect occurs when the threshold condition $\beta = \frac{1}{n}$

referred as Cherenkov threshold is fulfilled, resulting in the Cherenkov angle θ being equal 0. For extreme high-momentum particles, the Cherenkov angle θ is at the maximum when β is close to 1.

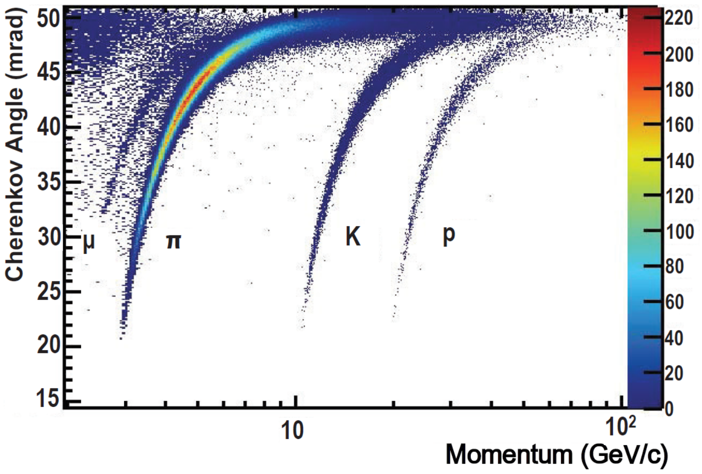

Figure 3.2: Reconstructed Cherenkov angle as a function of track momentum in the C_4F_{10} radiator for muons, pions, kaons and protons [73].

The importance of the PID in the physics analyses based on the $B_s^0 \to D_s^{\mp} K^{\pm}$ decays is discussed in Chapter 4.

3.2 LHCb RICH Detector

In the followed section, the design and structure of the RICH detectors, used for the LHC Run II (2015-2018), is presented.

3.2.1 Overview

The LHCb RICH detectors are essential for the separation of pions from kaons in b- and c-hadron decays. To cover the full momentum range, the RICH detection system consists of two detectors. The upstream RICH1 detector is used for the low momentum charged particle range of ∼(1-60) GeV/c and covers the full LHCb acceptance from ±25 mrad to ±300 (horizontal) and ±250 mrad (vertical). The downstream RICH2 detector is used for high momentum particles range of ∼(15-100) GeV/c and covers the limited LHCb acceptance from ∼±15 mrad to ±120 (horizontal) and ±100 mrad (vertical).

3.2.2 Structure and Design

Both the RICH detectors, presented in Figure 2.13 (2D) and Figure 3.3 (3D), consist of three main elements: a radiator medium to produce Cherenkov radiation, an optical system of mirrors to deflect Cherenkov photons on the photodetector planes and actual photodetectors.

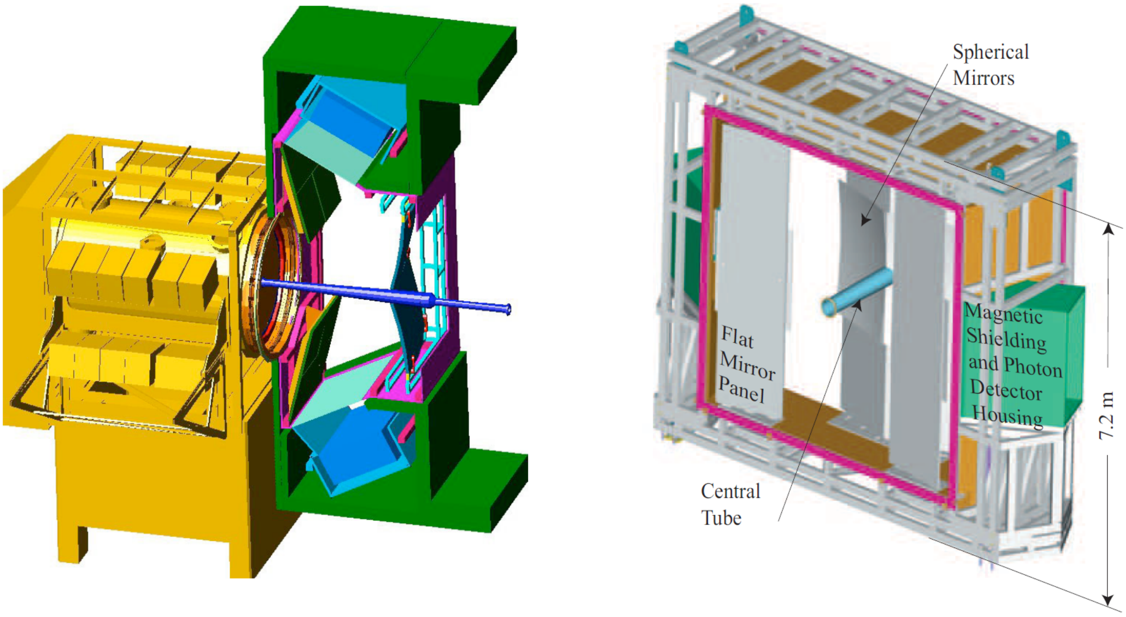

Figure 3.3: Schematic representation of the RICH1 (left) with gas-tight seal connected to the VELO tank, and the RICH2 (right) [62].

A gas enclosure contains a radiator medium which is essential for the production of Cherenkov radiation. A radiator medium, dependent on the energy of photons, is a medium that has a known refractive index. The fluorocarbon gases C_4F_{10} and CF_4 are used as radiators for the RICH1 and RICH2, respectively. Their refractive indices are equal to 1.0014 and 1.0005, for C_4F_{10} and CF_4 respectively, at wavelength of 400 nm, temperature of 0 °C and pressure of 101325 Pa [62].

Cherenkov photons, created in a radiator medium, are projected by an optical system. Both the RICH detectors use similar concept and design of spherical and flat mirrors. Cherenkov photons are focused using tilted spherical mirrors to obtain the 3D Cherenkov cone on the 2D ring image. The spherical mirror system is placed inside the acceptance of the experiment. Subsequently, the ring image is reflected on two planes of the photodetectors, positioned on both sides of the beam pipe. The photodetectors are surrounded by the magnetic shielding which reduces the stray field of the dipole magnet. The photodetector planes are positioned above and under the beam pipe for the RICH1, and on the left and right of the beam pipe for the RICH2. The difference in the arrangement between the RICH1 and RICH2 comes to the magnetic shielding as the RICH1 is positioned closer to the magnet.

The spatial positions of produced Cherenkov photons are measured by the dedicated photodetectors called Hybrid Photons Detectors (HPDs) [95]. A typical HPD is a vacuum photodetector where a photoelectron is accelerated by an applied voltage on a reverse-biased silicon detector. Photoelectron energy is dissipated in silicon resulting in a creation of electron-hole pairs, with an average 3.6 eV of deposited energy per pair. The detection of a single photoelectron is performed by read-out electronics. The HPDs, introduced in the RICH detectors (Figure 3.4), are segmented into 1024 pixels, in the matrix of 32 rows × 32 columns, where each pixel has a size of $500 \times 500\ \mu\text{m}^2$. The pixels altogether cover a surface of 2.5×2.5 mm^2 at the photocathode. A nominal operating voltage is 20 kV which corresponds to around 5000 electron-hole pairs released in the silicon. The HPD consists of quartz-fabricated entrance window (7 mm thickness and 55 mm inner radius of curvature), a tube diameter of 83 mm with an active diameter of 75 mm and a multi-akali type photocathode deposited internally on the quartz surface. A total number of 484 tubes (196 for the RICH1 and 288 for the RICH2) are installed on the four photodetector planes (two for each detector) to cover the RICH photodetection surface of around 3.5 m^2.

Figure 3.4: Image of a single HPD (left) and the RICH1 HPD plane (right) [62][96].

3.3 Upgraded LHCb RICH Detector

During the LHC LS2 (2019-2021), the LHCb detector undergoes a major modernization. The latter involves a replacement of the components that were exposed to the high radiation damage during the Run I and Run II, as well as an introduction of the upgraded system to meet the new requirements of the new LHCb detector. The upgrade allows for the data taking at the significantly increased instantaneous luminosity: from 4×10^{32} $\mathrm{cm}^{-2}\mathrm{s}^{-1}$ to 2×10^{33} $\mathrm{cm}^{-2}\mathrm{s}^{-1}$ and the data acquisition rate increased from 1.1 MHz to 40 MHz.

3.3.1 Overview

Both the RICH detectors are upgraded and the entire opto-electronic system is redesigned to cope with the higher read-out rate and the increased occupancy.

The PID performance is defined in terms of the efficiency of the identification of a particle under its own hypothesis (e.g. a kaon as a kaon) and its misidentification probability (e.g. a pion as a kaon or a proton). The change in the geometry (with respect to the current one) will increase the PID efficiency and decrease the wrong misidentification, improving overall performance of the system. Figure 3.5 presents the expected improvement of the PID performance (a kaon identification and a misidentification of a pion as a kaon) for the current and upgraded geometrical setup. `Lumi4` refers to the instantaneous luminosity of 3.9×10^{32} $\mathrm{cm}^{-2}\mathrm{s}^{-1}$, `Lumi10` to 10×10^{32} $\mathrm{cm}^{-2}\mathrm{s}^{-1}$ and `Lumi20` to 20×10^{32} $\mathrm{cm}^{-2}\mathrm{s}^{-1}$. The last-mentioned luminosity is the luminosity at which the LHCb detector will operate during the Run III. As it can be seen, the upgraded geometry (green color) highly surpasses the current geometry (red color) for the `Lumi20` in terms of the PID performance. Thanks to the upgrade, the PID performance of the new detector will be similar to the PID performance for the Run II of the `Lumi4` (black color).

The LHCb RICH detectors upgrade involves a modification to the optics and mechanics, a change of the read-out electronics and a replacement of the photodetectors. Depending on particle flux, two distinctive regions of the occupancy can be distinguished which require different needs of precision. For these regions, two kinds of photodetectors are implemented, referred as R-type and H-type. The first one covers a region of higher occupancy (the whole RICH1 and the center of the RICH2)

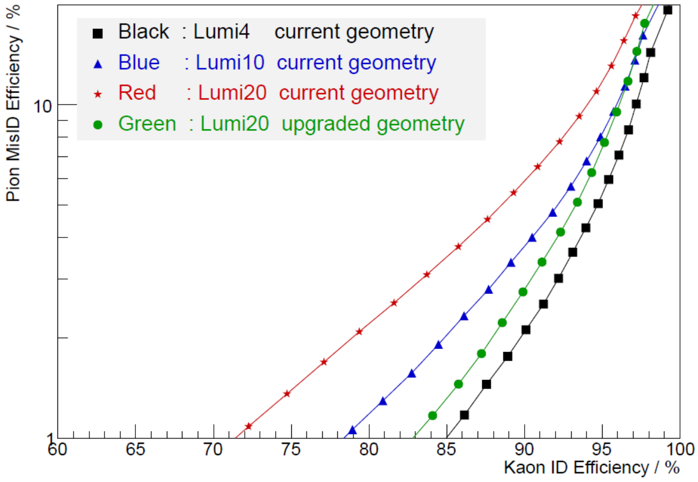

Figure 3.5: The PID performance of the current geometry at Lumi4, Lumi10, Lumi20 and the upgraded geometry at Lumi20 [91].

while the latter one covers a region of lower occupancy (borders of the RICH2).

3.3.1.1 Optics and Mechanics

The upgrade of the RICH encompasses optical and mechanical changes as well. A new optical system is implemented together with the mechanical structure modification to decrease the photon occupancy in central regions of the detector and to improve the Cherenkov ring angular resolution. At the higher luminosity, the photon occupancy is foreseen to be over 30% of the peak occupancy, which significantly decreases the PID performance. For these reasons, the focal plane is moved backwards. Two different kinds of mirrors are installed: plane and spherical. The new spherical mirrors exhibit larger radius of curvature by a factor of $\sim\sqrt{2}$: from 2700 to 3800 mm. Figure 3.6 presents the current and upgraded optical geometries of the RICH1. The optimization in optics and the redesign of mechanics keep the occupancy below 30% and increase the ring size. In addition, a magnetic shield is modified and a larger gas enclosure is manufactured. An introduction of the new photodetectors, together with their read-out electronics, entails the implementation of the new mechanical support and cooling system to keep temperature below 35 °C.

Similarly for the RICH2, a new support and cooling system is designed for the two new photodetector arrays. However, the vessel, gas and optical systems remain unchanged.

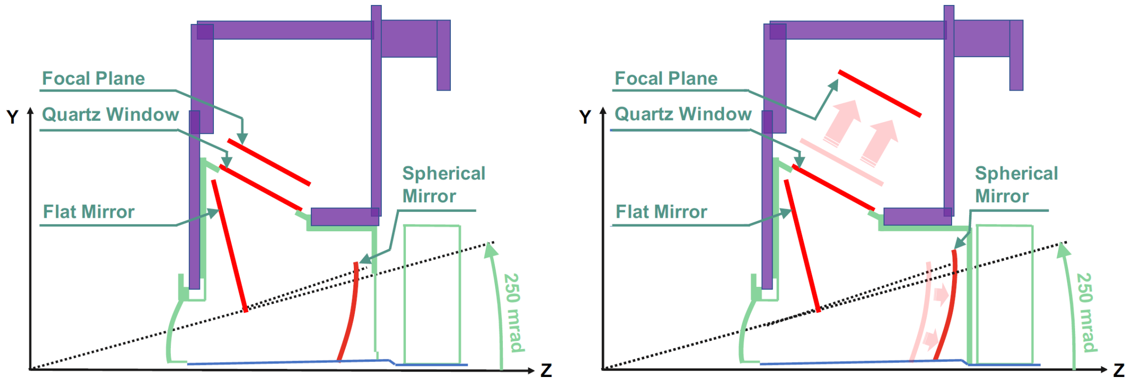

Figure 3.6: The current (left) and upgraded (right) optical geometry of the RICH1 detector. [97].

3.3.1.2 Read-out Electronics

The removal of the L0 hardware trigger (maximum read-out capability of 1.1 MHz) and the introduction of the software trigger (read-out capability of 40 MHz equivalent to the LHC bunch crossing) requires most of the read-out electronics to be changed. In addition, to withstand the higher radiation levels due to the increased instantaneous luminosity, new front-end (FE) electronics needs to be radiation-tolerant in the new environment. These challenges required the preparation of a new custom-made ASIC FE chip named CLARO. The CLARO is the core of the new photodetectors and is described thoroughly in Chapter 3.3.2. The CLARO chips are incorporated on custom boards, called front-end boards (FEBs), that are connected to the baseboards (Bbs) where Multi-Anode Photomultiplier Tubes (MaPMTs) are installed. The CLARO creates a digital pulse when a photon hits a corresponding MaPMT pixel. The signals coming from CLAROs, are transferred to the field-programmable gate arrays (FPGAs) mounted on the Photon Detector Module Digital Board (PDMDB) that handles four Elementary Cells (ECs), as presented in Figure 3.7. Digital boards (DBs) send the acquired packets out of the detector, configure the operational parameters of the CLARO chips and host a low voltage power supply circuitry.

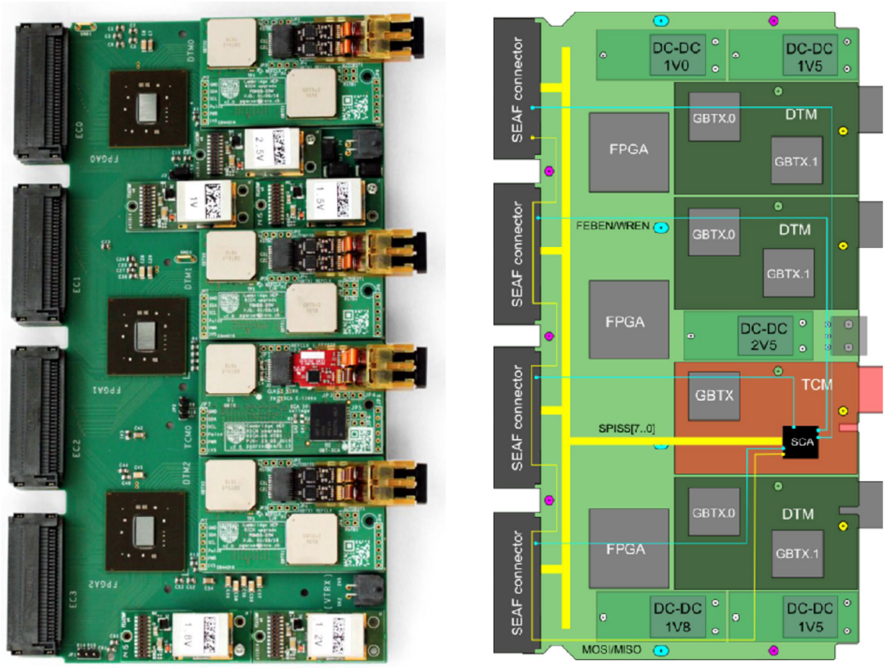

Figure 3.7: A representation of the fully equipped R-type PDMDB module that operates four ECs of R-type. On the left, a prototype configuration is presented while on the right, a scheme is shown [98].

3.3.1.3 Photodetectors

The requirements for a new photodetector involve:

- a single photon counting in the wavelength range of 200-600 nm,
- a pixel size not exceeding 3×3 mm^2 in the regions of the highest occupancy,
- negligible cross-talk between neighboring pixels,
- negligible dark current with respect to the signal intensity,
- being not affected by magnetic field of up to 30 mT.

For these reasons, the current HPDs are replaced by the MaPMTs. A picture on the left of Figure 3.8 represents two types of the MaPMTs (R-type and H-type) that are introduced for both the RICH detectors. A detailed specification of the new photodetectors is given in Section 3.3.3. By combining the MaPMTs with the

FE electronics, a basic unit of the RICH detection system is created, called the Elementary Cell. The ECs are described in more details in Section 3.3.4.

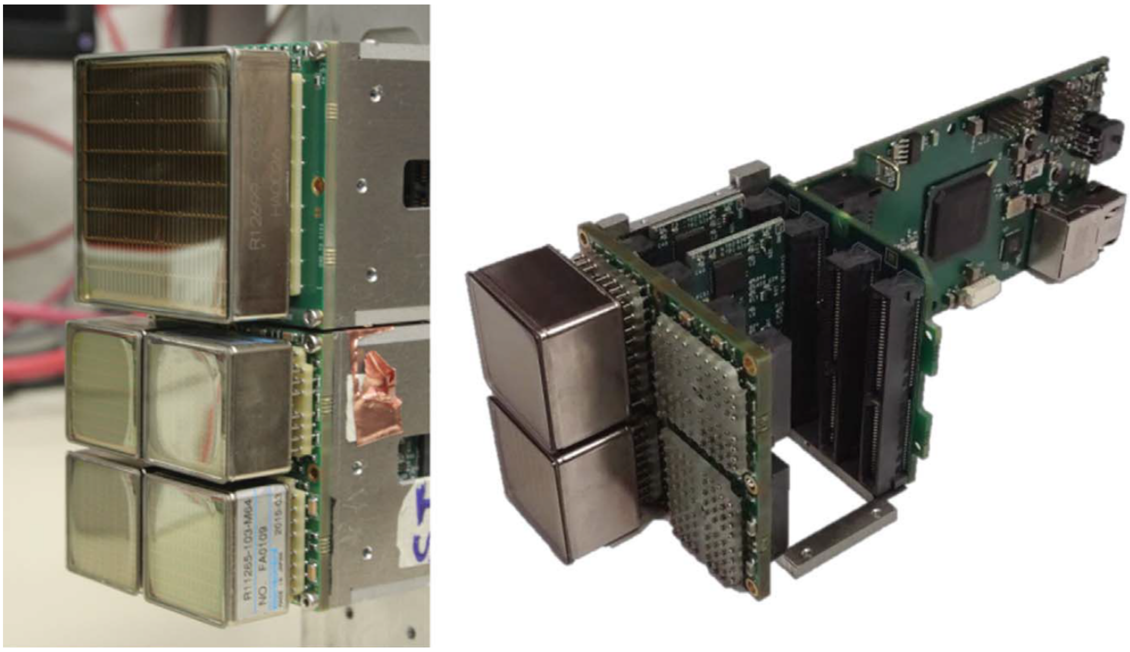

Figure 3.8: On the left side, a picture of the H-Type (upper) and R-type (lower) MaPMT. On the right, a half-assembled EC of R-type. [99].

A standard Photomultiplier Tube (PMT), filled with vacuum, converts photons to photoelectrons due to the photoelectric effect. Incoming photons strike the photocathode ejecting electrons from the surface that, due to electrostatic fields, are directed and accelerated towards a single electron-multiplier unit (dynode). Each dynode has higher potential than the preceding one using resistors. The accelerated photoelectrons reach the first dynode that produces low energy secondary electrons which are accelerated again towards the next dynode and so on. The multiplied electrons arriving to the anode produce a current pulse that is detectable. Two parameters describe a PMT: the quantum efficiency which is the probability of producing photoelectrons when a photon strikes the photocatode, and the gain which is the ratio between the output current of the anode and the photoelectric current produced by the photocathode. The MaPMTs are equivalent to incorporating multiple PMTs in a single housing as presented in Figure 3.9.

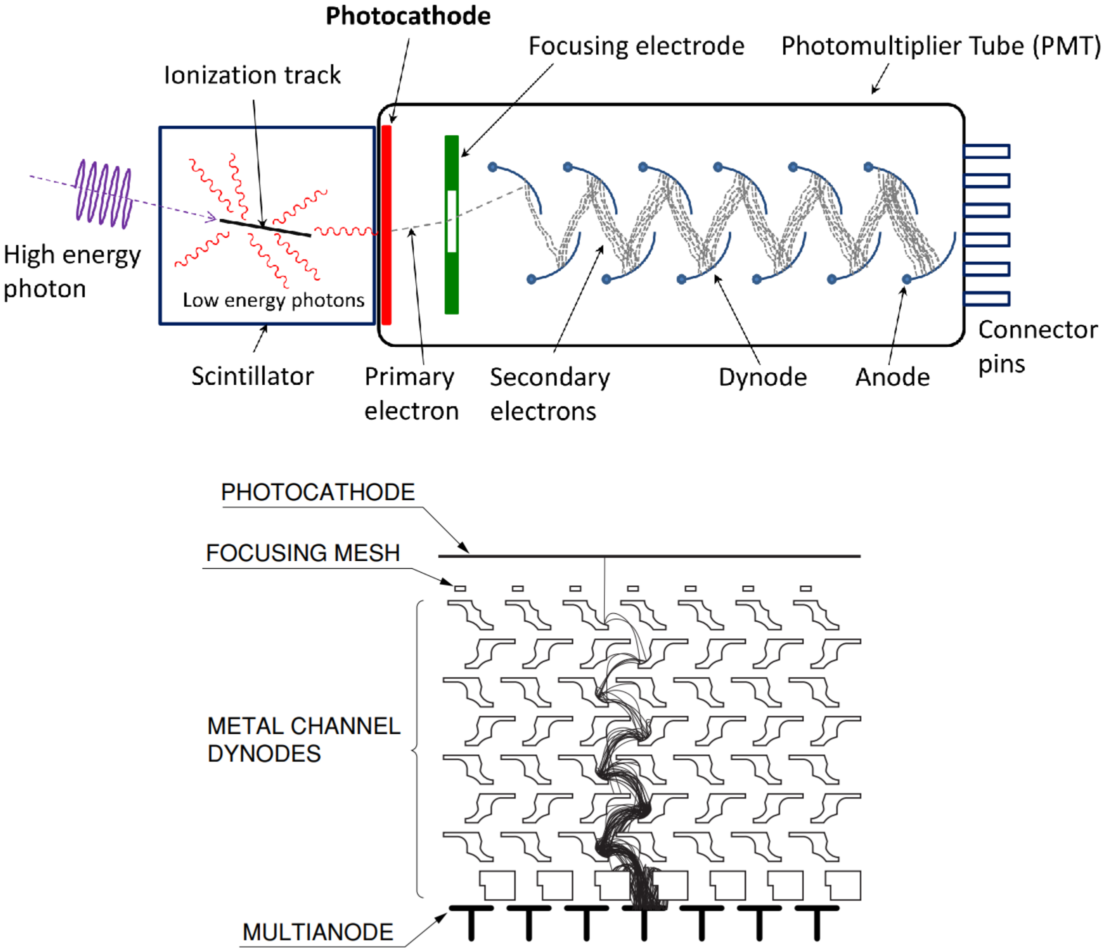

Figure 3.9: A schematic structures presenting a PMT (top) and an MaPMT (bottom) with electron trajectories [100].

3.3.2 CLARO ASIC

The CLARO [101] is a customized FE read-out chip particularly tailored for the R11265 MaPMTs that was designed by INFN Milano Bicocca, INFN Ferrara and AGH Kraków. The application-specific integrated circuit (ASIC) chip is specially designed for a single photon counting up to 40 MHz. The CLARO comprises 8 channels with an amplifier and a discriminator. A schematic diagram of a single channel of the CLARO is presented in Figure 3.10. Each CLARO channel is supplied with an analogue pulse shaper amplifier and a binary discriminator. The purpose of the preamplifier is to read provided current pulses and convert them to voltage signals with amplitudes proportional to deposited charges. The signals are analysed by the discriminator with a configurable threshold. If the amplitude of a signal is higher than the established discriminator threshold, a digital pulse is produced.

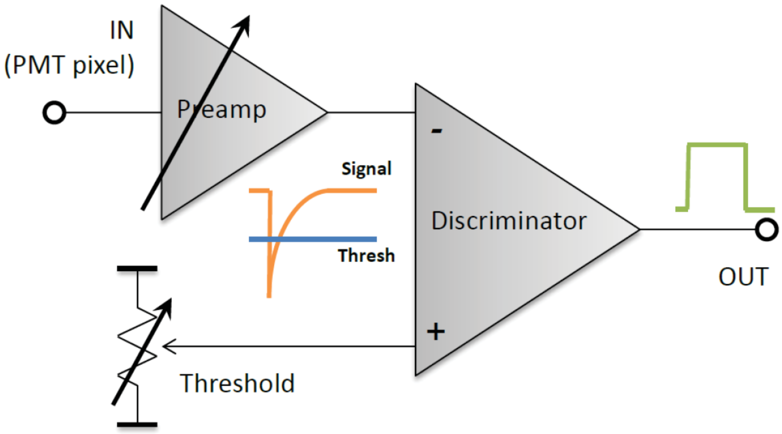

Figure 3.10: Schematic diagram of a single channel of the CLARO chip [91].

The CLARO, shown in Figure 3.11, is designed in 0.35 μm CMOS technology from Austria Microsystems (AMS) company [102] to operate at 2.5 V supply voltage. The technology is inexpensive, widely used and with a high yield that meets the LHCb RICH upgrade requirements (e.g. radiation tolerance and the speed of response). In order to satisfy the demand of a single photon signal counting at high rate of 10^7 hits per second, the CLARO has a baseline recovery time (time required for sensors to go back to the baseline signal) and peaking time (time required for a shaped pulse to go from the baseline to the peak) lower than 25 ns and 5 ns, respectively. No additional cooling is needed as the CLARO has low power consumption at the level of 0.7 mW (for idle mode) and 1.5 mW (for high speed and low input impedance mode) per channel. Such introduction is crucial since the ECs are tightly assembled leaving not much space for other installations. The CLARO is capable of withstanding expected radiation levels in the upgraded environment throughout the 10 years of future operation. At the RICH photodetector planes, it is foreseen that each year the accumulated doses are 40 krad Total Ionising Dose (TID), 6.1×10^{11} cm^{-2} 1-MeV equivalent neutrons and 2.3×10^{11}cm^{-2} hadron fluence above 20 MeV.

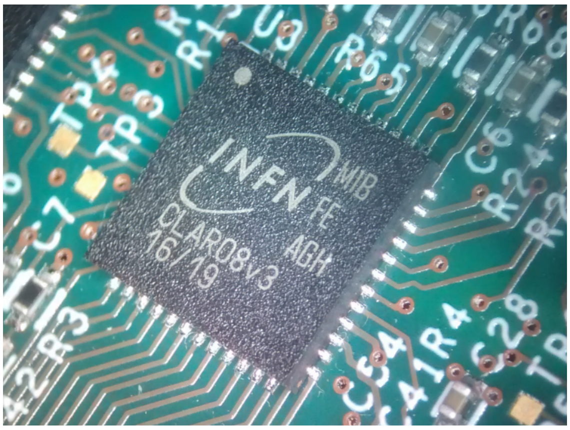

Figure 3.11: A picture showing the CLARO chip [101].

The configuration of the CLARO is stored in a 128-bit register which can be accessed by a Serial Peripheral Interface (SPI). Triple Modular Redundancy (TMR) protects the register long term storage against the configuration register bit flip called Single Event Upsets (SEUs). Three copies of the configuration register are kept in separate cells at different locations in the chip. If one register copy is compromised due to a SEU, the other two cells correct the register configuration.

Each CLARO channel is adjustable with a 12 bits configuration register, with a possibility to read/write (R/W), as presented in Table 3.1. The first six bits select a threshold ranging from 0 to 63 units. The next two bits corresponds to attenuation which reduces the channel gain by the factor of $1/2^n$:

- n = 1, reduction of 1/2 - 6-bit disabled and 7-bit enabled,
- n = 2, reduction of 1/4 - 6-bit enabled and 7-bit disabled,
- n = 3, reduction of 1/8 - both bits enabled,
- n = 0, no reduction - both bits disabled.

Without attenuation, the usual threshold step is $\sim$30 ke$^-$ that ranges up to $\sim$2 Me$^-$. The 8-bit position turns the channel on or off. The 9-bit position switches on or off the hysteresis parameter. The hysteresis is used to avoid output oscillations in channels with thresholds established too close to the baseline. The next bit enables the injection of charge from internal capacitors which is useful for the calibration of

CLARO channels (Section 3.4.4.1). The last bit enables the offset which shifts the threshold by half (-32) to reach negative threshold steps (Section 3.4.4.2).

Table 3.1: Configuration bits of CLARO channels.

Bit Position	Name	Mode
0:5	Threshold	R/W
6:7	Attenuation	R/W
8	Input Enable	R/W
9	Hysteresis Disable	R/W
10	Test Pulse Disable	R/W
11	Offset Enable	R/W

The development of the CLARO started in 2011. The ultimate version, that is going to be implemented in the upgraded LHCb RICH system, is the CLARO8v3 where the configuration register is synthesized using the Radiation Hardened By Design (RHBD) digital cell library introduced by Instituto de Microelectrónica de Sevilla IMSE-CNM. The CLARO chips are incorporated in the FEB modules. Each FEB consists of 8 CLARO chips as presented in Figure 3.12. They are installed equally on both sides of a FEB (four by four). For the identification purpose, a QR code is placed on one of the CLARO chip of each FEB modules.

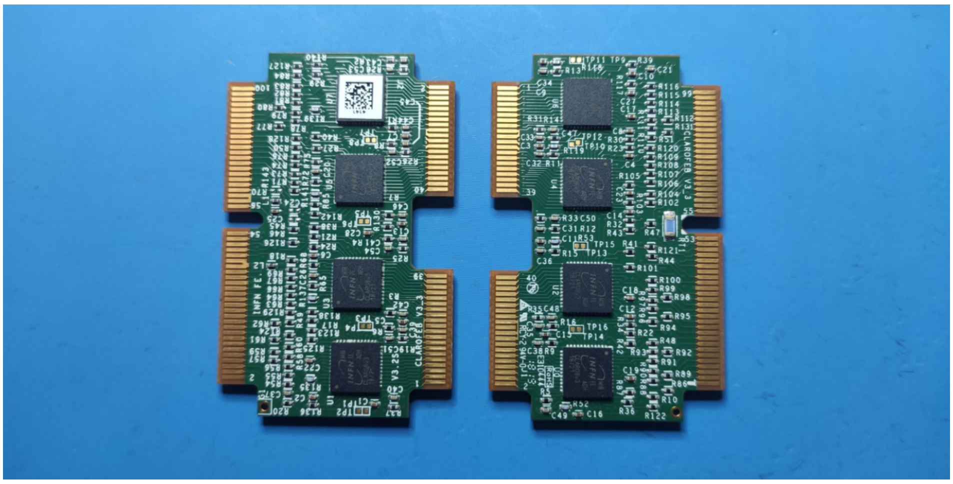

Figure 3.12: A picture representing the front and back of a FEB module. Each FEB comprises 8 CLARO chips (black squares). On one CLARO chip (white square) of each FEB, a FEB QR code is attached.

3.3.3 Multi-Anode Photomultiplier Tube

The MaPMT is a new photodetector dedicated for the RICH upgrade that was designed by Hamammatsu Photonics company [103]. The two models, shown in Figure 3.13, are optimized for a single photon detection, and are introduced in the new RICH system.

In the inner region, the `R13742` MaPMT model from R11265 series, referred also as the R-Type MaPMT, is going to be installed. The new unit is a 26.2 mm square device comprising 64 silicon pixels (8×8 matrix) under a 0.8 mm thick UV/borosilicate entrance window. A pixel size is approximately 2.9×2.9 mm^2. It has a super/ultra bi-akali (SBA/UBA) photo-cathode and a tube with 12 stages of dynodes. The minimum active area for a photon detection is 23×23 mm^2. A very narrow inactive border around the device ensures a geometrical acceptance of 77% for each tube. At 1000 V operating voltage, a typical gain is 10^6 e^-. The photo-electron collection efficiency is about 90% at the first dynode. Four MaPMTs are installed on a custom Bb in 2×2 matrix.

In the outer regions of the RICH2, the `R13743` model from R12699 series, referred also as the H-Type MaPMT, will be implemented. In comparison to its cousin, this particular model is four times bigger with the active area equal to 48.5×48.5 mm^2. It exhibits the same 8×8 pixel matrix where each pixel size is 6×6 mm^2. Similarly to the R-Type MaPMT, the same gain is expected of 10^6 e^- at 1000 V.

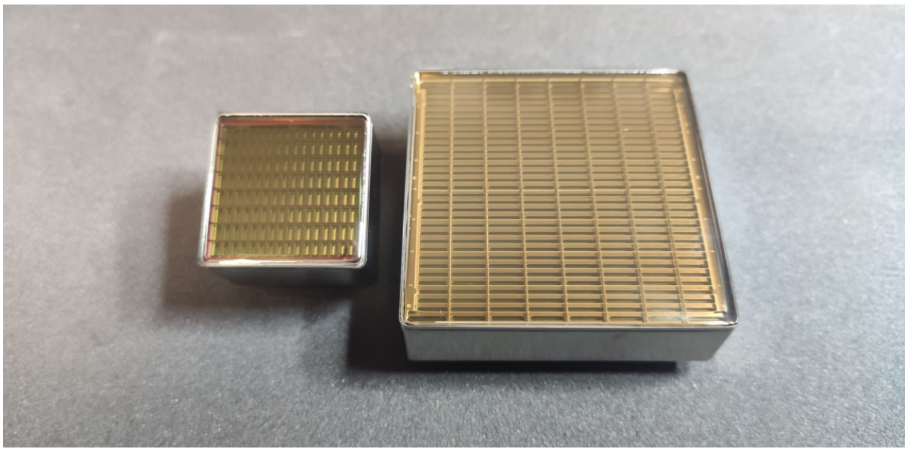

Figure 3.13: On the left side, the R13742 MaPMT model (R-Type) is presented. On the right side the R13743 MaPMT model (H-Type) is shown.

3.3.4 Elementary Cell

The EC is a complete, autonomous building unit of the upgraded RICH detection system comprising the FE read-out electronics and MaPMTs. Depending on the type of the MaPMT, there are two types of EC.

3.3.4.1 Structure

The R-type EC contains four R-type MaPMTs which are installed on four sockets (2×2 matrix) of R-type Bb. On the other side of a Bb, four FEB modules are included. Each FEB contains eight CLARO chips. Each CLARO chip contains eight CLARO channels. This way, 256 MaPMTs channels correspond to 256 CLARO channels. From the other side, FEBs are closed with R-type back board (Bkb) which joins the CLARO to the FPGA digital boards. A four units of aluminum chassis encloses the FEBs and works as a support for the Bb and Bkb. Residual magnetic fields from the LHCb dipole magnet are 30 G and 15 G in RICH1 and RICH2 respectively (1 G = 10^{-4} T). As magnetic fields causes loss of gain and photodetection efficiency, the R-type ECs dedicated for the RICH1 are supplied with a cross-shield μ-metal modules as presented in Figure 3.14. This introduction lowers the intensity of the dipole residual and allows a full recovery in the central pixels and >85% recovery for pixels at the edges [97].

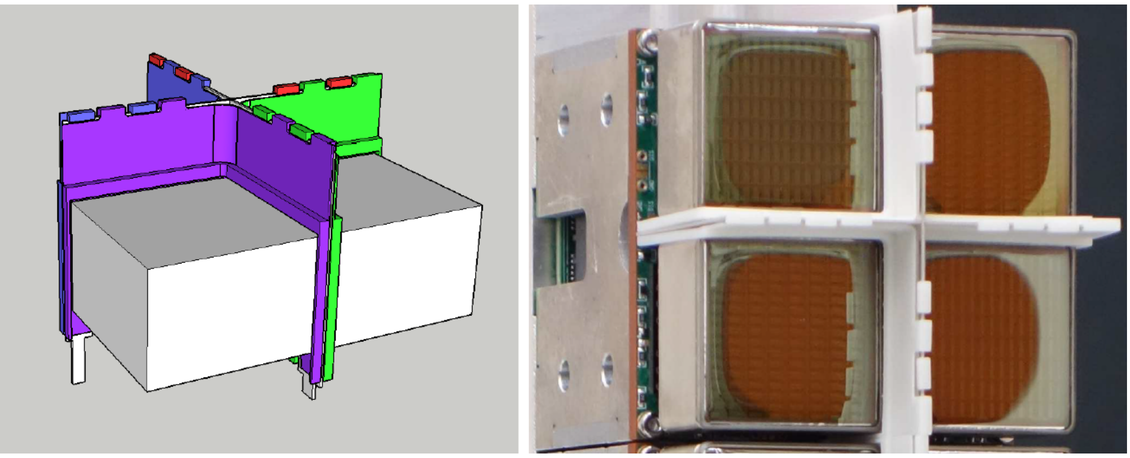

Figure 3.14: A cross-shaped local shielding added to the EC of R-Type for the RICH1 detection plane [97].

The H-type EC has the same mechanical concepts as R-Type EC but with a few exceptions. It contains one H-type MaPMT which is installed on one socket of H-type Bb. Two FEB modules are included together with H-type Bkb. Theoretically, one FEB module is sufficient to read-out 64 MaPMT channels but rather than that, halves of two FEB modules are used. The unused half of CLARO channels have a 1 nF capacitance making the signals not possible to be registered.

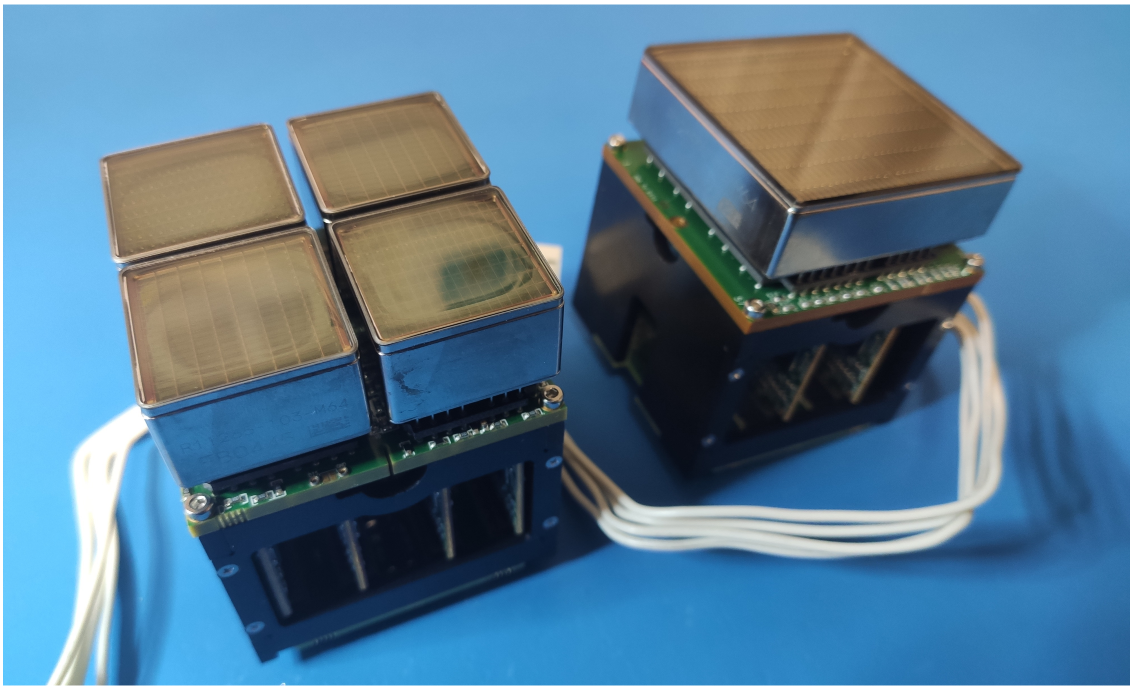

Figure 3.15: A picture presenting a fully mounted R-type (left) and H-type (right) EC.

3.3.4.2 Photodetector Planes

The ECs will be installed on dedicated columns that will form a Photon Detector Assembly (PDA) planes of area of 1.6 m^2 and 2.1 m^2 in the RICH1 and RICH2, respectively. For the RICH1, two PDA of 10 columns × 22 rows and 1 column × 20 rows are implemented and contain 480 EC of R-type only. For the RICH2, two PDA of 12 columns × 24 rows where 8 central rows are dedicated for 192 R-Type ECs and the upper and lower rows for 384 H-Type [104]. A quantity of ECs and corresponding MaPMTs for RICH upgrade is presented in Table 3.2.

Table 3.2: A quantity of ECs and MaPMTs required for the RICH upgrade.

	ECs		MaPMTs	
	R-Type	H-Type	R-Type	H-Type
RICH1	480	-	1920	-
RICH2	192	384	768	384
RICH1 + RICH2	672	384	2688	384
	1056		3072	

To cover a 3.7 m^2 plane, an exact number of 672 R-type and 384 H-type ECs will be used which is equivalent to 2688 R-Type and 384 H-Type MaPMTs. In addition, 20% of spare ECs and MaPMTs has been assumed which gives a total number of ECs and MaPMTs to be tested about 1300 ECs and 5000 MaPMTs. The total number of MaPMTs pixels that will cover RICH planes equals 196608. A PDM comprising two DBs containing FPGAs will operate four ECs. A graphical representation of the RICH2 plane with PDM is presented in Figure 3.16.

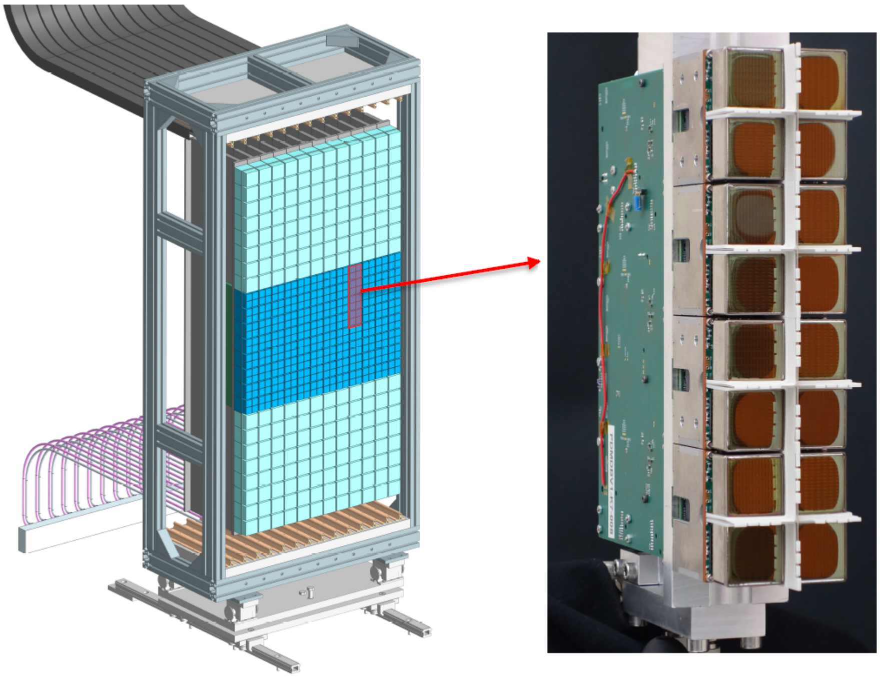

Figure 3.16: A schematic representation of the photodetector array of the RICH2 with an exemplary indication of a PDM with magnetic cross-shielding [105][106].

3.3.4.3 Characterisation

DAC Scan

The Digital Analog Converter (DAC) scan is a measurement performed on the FE electronics, as the signal is delivered directly to the CLARO channels. A fixed single photon counting threshold is set (Table 3.1), from the 64 DAC steps (0-63), that can be converted to a charge using the following formula:

$$Q_{inj} = DAC\_step \times 1.22\,\mathrm{mV} \times 640\,\mathrm{fF} \cong DAC\_step \times 4.874\,\mathrm{ke}^{-}. \tag{3.6}$$

A known charge Q_{inj}, defined as a number of pulses of equal amplitudes, is injected at the CLARO input. The calibration is performed using the mentioned DAC which generates an analog signal of known amplitude. If the injected charge is lower than the established discriminator threshold, there is no triggering and the output is equal to 0. By sending increasingly higher amplitudes over time, at certain point, the injected charge exceeds the discriminator threshold. All the pulses at the input are then recorded and for each one the output equal to 1 is produced. As a result, the number of detected signals as a function of the DAC voltage can be observed (Figure 3.17). Theoretically, a perfect step distribution should be obtained but when taking into account the electronic noise, the shape tends towards the letter "S" hence the name "S-Curve". The derivative of an S-Curve is a Gaussian distribution where its centre is a transition point, which corresponds to the threshold equivalent input charge, and its width is a noise (also called spread) of a charge. One of the methods used to acquire both of these parameters is by fitting an S-Curve with a translated error function (erf). The standard erf is defined as:

$$erf(x) = \frac{2}{\sqrt{\pi}} \int_0^x e^{-t^2} dt \tag{3.7}$$

and the translated erf is determined as:

$$f(x) = \frac{1}{2}[1 + erf(\frac{x - x_{tr}}{\sigma})] \tag{3.8}$$

where x_{tr} is a transition point at which the distribution reaches half of its height and the σ is the width of the curve slope that is equivalent to noise.

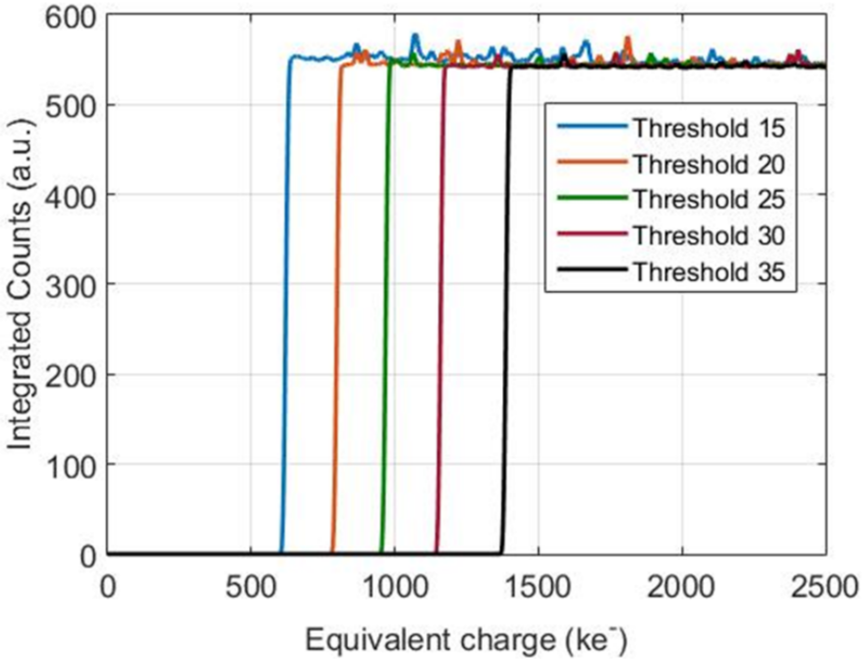

Figure 3.17: S-Curve at different discriminator threshold values [107].

Threshold Scan

The threshold scan is a measurement performed to calibrate the MaPMTs. On the contrary to the DAC scan, where the discriminator threshold is fixed and the amplitude of the signal gradually increases, in the threshold scan the threshold changes at the constant amplitude of the signal. The MaPMTs are powered on at a certain voltage. Each anode of the MaPMTs is conjugated with the corresponding CLARO channel and is illuminated by a blue LED light. The initial threshold is set to its maximum, equal to 63. The CLARO channels start to acquire the signals which are above the threshold and the total number of events is recorded. The process is repeated, each time decreasing the threshold by 1 until it reaches the last threshold at 0. As a result, the distribution of above-threshold events can be produced (Figure 3.18) that corresponds to the integral distribution of the single photoelectron spectrum. The distribution allows to determine the working point of a CLARO channel which is the most optimal threshold that separates the signal from the noise. The pedestal shown in above-demonstrated Figure (right one) represents the electronic noise. The working point is the threshold at the first edge after the pedestal. To have a certainty that the noise is cut off completely, the working point is established slightly higher, usually by few threshold steps higher to the one obtained. Such operation cuts slightly the signal but blocks the electronic noise substantially. The majority of the CLARO channels do not possess the pedestal at the offset bit 0 even on the lowest possible thresholds. By setting the offset bit to 1, the thresholds are shifted by -32 (to the left) where all the CLARO channels have the pedestal and by so the working point is possible to be determined.

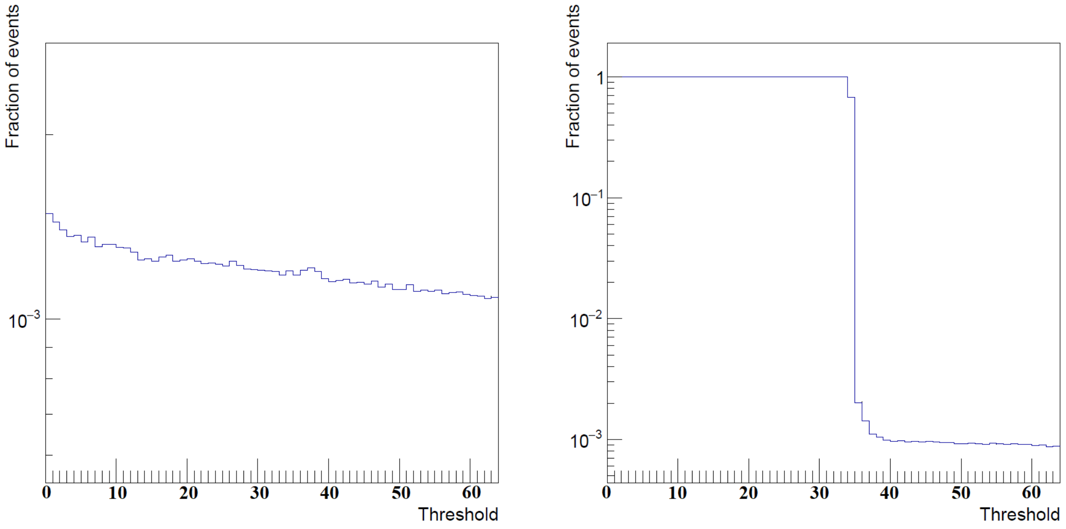

Figure 3.18: Threshold scan distributions. On the left hand side the offset bit of CLARO channels is set to zero while on the right hand side the offset bit is set to one.

Dark Count Rate

The dark counts are signals not generated by photon events but rather due to spontaneous electron emission such as thermal emission from the photocathode. The dark count rate (DCR) is the average rate of recorded events without any provided source of light. For each MaPMT anode, the dark counts are registered within a certain period of time:

$$DCR = \frac{events}{t} \tag{3.9}$$

The DCR provides a distinction of anodes with high counts and an illustration of the uniformity of the MaPMTs.

Signal Induced Noise

There is non-negligible probability of having noisy signals from the MaPMTs in a time window of few μs after the main signal. The Signal Induced Noise (SIN) measurement is used to quantify the constitution of the after-pulses with respect to the true signal generated by an LED light. Figure 3.19 presents the SIN distribution where each step is equivalent to $25ns$. After calculating the integrated signal and the integrated SIN, the SIN Fraction can be calculated using the following formula:

$$SIN\ Fraction = \frac{noise}{signal + noise}, \tag{3.10}$$

together with the Signal to Noise (S/N) ratio:

$$S/N\ Ratio = \frac{signal}{noise}. \tag{3.11}$$

Both parameters provide an information of the intensity of the SIN to the signal for each anode of the MaPMT.

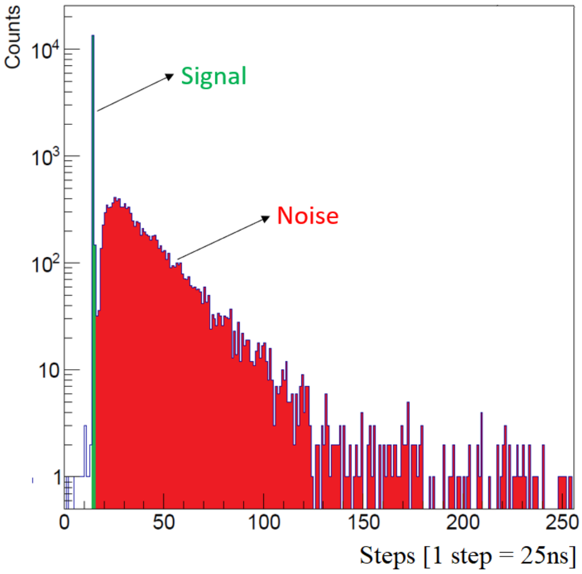

Figure 3.19: SIN distribution. The true signal occurs for the steps 14-15 while everything after (steps 16-254) is considered as a SIN.

Chapter 4

Importance of the Particle Identification in the Physics Analysis

In this chapter, the importance of the PID information in the physics analyses is discussed on the example of the studies of the $B_s^0 \to D_s^{\mp} K^{\pm}$ decays. A simplified analysis of this decay channel, oriented for the demonstration of the importance of the RICH particle identification, was performed by the Author.

4.1 Introduction

The operational time of the LHC Run III will largely overlap with data taking period of the Belle II experiment [108] at the SuperKEKB asymmetric e^+e^- collider [109]. The latter assumes collecting about 50 fb^{-1} of data by 2025, when the experiment will be concluded. Due to different collision environments two experiments are considered complementary. The SuperKEKB will operate at the centre-of-momentum energy close to the mass of $\Upsilon(4S)$ resonance. This offers several advantages in particular for the studies of the τ lepton properties as well as decays with neutral final state particles or missing energy. On the other hand, a high energy collision at LHC allows to reconstruct larger yields of events in the LHCb detector, including the B_s^0 mesons. However, the environment of hadronic collisions requires a significant reduction of 30 MHz inelastic input rate (Figure 2.19) to the acceptable values of 10 GB/s which meets computing resources limitations [110]. In the HLT1, the decays are selected based on the kinematic and geometric properties, while the excellent performance of the PID achieved in the HLT2 is necessary to reduce the cross-feed background contamination. Introduced during the LHCb Run II the real-time reconstruction and analysis paradigm [111][112] let to store only the subset of information needed for the physics analysis, reducing event size and saving higher statistic and/or more selections. Similarly, the reduction of background contamination allows higher signal statistics being saved on disks. Therefore, the excellent PID performance is necessary for the physics analyses.

4.2 Combined Particle Identification Information

Various charged particles are created from an individual *pp* collision, such as electrons, protons, muons, pions and kaons. The proper identification is essential for the reconstruction of hadron decays. To achieve that, the difference in logarithmic likelihood is stated as:

$$DLL(A - B) = ln\mathcal{L}_A - ln\mathcal{L}_B, \tag{4.1}$$

where $\mathcal{L}_A$ and $\mathcal{L}_B$ represent the likelihood of a particle to be identified under the A and B hypotheses, respectively. If $DLL(A - B) > 0$, the particle is more likely to be A while if $DLL(A - B) < 0$, then the particle is more probable to be B. The likelihood for a specific particle hypothesis is acquired by RICH detectors together with calorimeter and muon systems.

4.3 Particle Identification in the Run II data

The LHCb experiment measures quantities of a large variety decays with kaons and pions final state particles. These are the $\mathcal{CP}$ violation measurements [113] or searches for rare decays [114]. As an example the charmless, oppositely charged two-body final states h^-h^+ are considered, where $B^0_{(s)}$ meson can decay either to two kaons K^+K^-, a kaon-pion pair $K^\pm\pi^\mp$ or two pions $\pi^+\pi^-$ as shown in Figure 4.1. In each of the considered decays, the signal yields are of the same order of magnitude (Table 4.1). Therefore, if not suppressed, the decays would significantly contaminate each other being the dominant cross-feed background. Their separation is achieved with usage of the PID requirements showing its importance for the physics analyses.

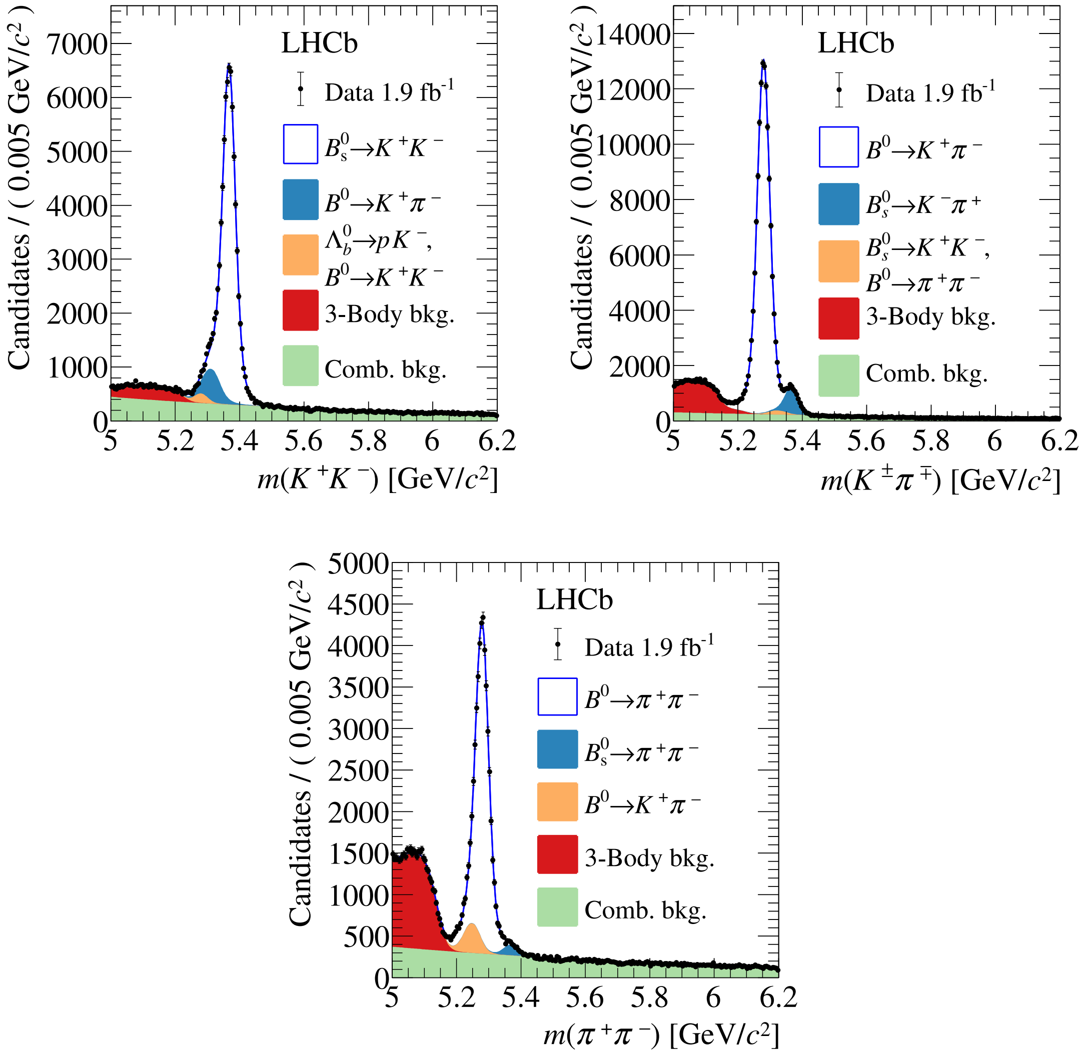

Figure 4.1: Invariant mass distribution for a pair of oppositely charged kaons (top-left), kaon-pion (top-right) and pions (bottom) [113].

Table 4.1: The signal yields for the $B \to h^+h^-$ decays [113].

Decay	Yield
$B^0 \to \pi^+\pi^-$	45620 ± 260
$B_s^0 \to K^+K^-$	70310 ± 320
$B^0 \to K^+\pi^-$	140340 ± 420
$B_s^0 \to K^-\pi^-$	10580 ± 150

4.4 The example of the $B_s^0 \to D_s^\mp K^\pm$ decays

Measurement of the CKM angle γ (Chapter 1.2) is one of the key analyses performed by the LHCb collaboration. In the majority, these analyses are performed using the decay-time-integrated methods [115][116] and decay-time-dependent methods [117][118] where decay-time relates to the reconstructed lifetime of neutral b-hadron particle. The LHCb experiment gives an unique opportunity to obtain this quantity from the $B_s^0 \to D_s^\mp K^\pm$ decays (Figure 4.2).

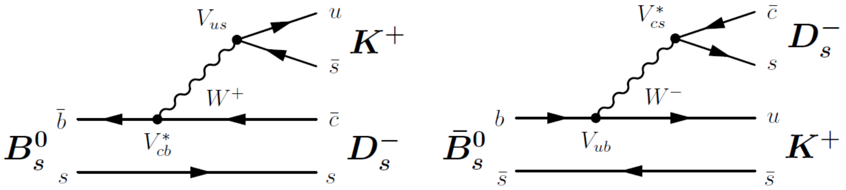

Figure 4.2: Feynman tree diagrams for the $B_s^0 \to D_s^\mp K^\pm$ decay.

Due to a small branching fraction, at the level of 10^{-4} (Table 4.2), and a very fast $B_s^0 - \overline{B}_s^0$ oscillations analysis of these decays is very challenging. The sample is significantly contaminated by the backgrounds coming from the mis-identification of one or more final state particles. Thus, usage of the PID requirements is necessary in order to obtain a pure signal sample.

Table 4.2: The branching fractions for the decays in question, as given by the [2].

Channel	Branching fraction
$B_s^0 \to D_s^\mp K^\pm$	$(0.23 \pm 0.02) \times 10^{-3}$
$B_s^0 \to D_s^- \pi^+$	$(3.04 \pm 0.23) \times 10^{-3}$
$B^0 \to D^- \pi^+$	$(2.57 \pm 0.13) \times 10^{-3}$
$\overline{\Lambda}_b^0 \to \overline{\Lambda}_c^- \pi^+$	$(4.9 \pm 0.4) \times 10^{-3}$
$D_s^- \to K^- K^+ \pi^-$	$(5.45 \pm 0.17) \times 10^{-2}$
$D_s^- \to \pi^- \pi^+ \pi^-$	$(1.09 \pm 0.05) \times 10^{-2}$
$D^- \to K^+ \pi^- \pi^-$	$(9.38 \pm 0.16) \times 10^{-2}$
$\overline{\Lambda}_c^- \to \overline{p} K^+ \pi^-$	$(6.28 \pm 0.32) \times 10^{-2}$

The following case uses a data set gathered by the LHCb detector in 2018. The corresponding integrated luminosity equals to 2.19 fb^{-1} (Figure 2.5) of pp collisions collected at the centre-of-mass energy of 13 TeV. Throughout the data taking, all components of the detector were functional. The main properties of the particles considered in this discussion are presented in Table 4.3.

Table 4.3: The main properties of the particles considered in the analysis [2].

Particle	Quarks	Mass [MeV/c^2]	Lifetime [ps]
$B_s^0/\overline{B}_s^0$	$s\bar{b}/\bar{s}b$	5366.77 ± 0.24	1.512 ± 0.007
D_s^+/D_s^-	$c\bar{s}/\bar{c}s$	1968.30 ± 0.11	0.500 ± 0.007
K^+/K^-	$u\bar{s}/\bar{u}s$	493.677 ± 0.016	12380 ± 21
π^+/π^-	$u\bar{d}/\bar{d}s$	139.57018 ± 0.00035	26033 ± 5

In order to select a pure signal sample, candidates must fulfill several requirements. First, they pass an online selection in the trigger, which is composed of two stages: a hardware and software. The former is based on information from the calorimeters and muon systems, while the latter applies a full event reconstruction [119]. After the trigger selection, a loose preselection is applied to the reconstructed candidates ensuring a good quality of b- and c-flavoured hadron candidates. Then, a kinematic vertex fit [120] is performed which forms a two-body $B_s^0 \to D_s^{\mp}K^{\pm}$ decay from the 4-track final state of pions and kaons. At first, $D_s^- \to K^-K^+\pi^-$ candidates are created from the reconstructed charged tracks. Then, the D_s^- candidate is further combined with an additional kaon track, forming a B_s^0 candidate. However, the data sample is contaminated by the three major sources:

- combinatorial background, which corresponds to the random combination of the final state particles, not originating from the true B_s^0 or D_s^- candidates,
- fully reconstructed background, where some of the final state particles are misidentified and/or originate from the decay of other particle. Usually these backgrounds are dangerous as they lie under the signal peak.
- partially reconstructed background, when during the reconstruction some particles are missing in the decay chain. Due to missing particles usually the invariant mass tends towards lower value, thus these backgrounds are less dangerous.

To further increase the signal to background ratio, an offline selection is applied. A combinatorial background is suppressed with a usage of the Multivariate Analysis (MVA) technique [121]. The invariant mass distribution of the $m(D_s^{\mp}K^{\pm})$ candidates is presented in Figure 4.3.

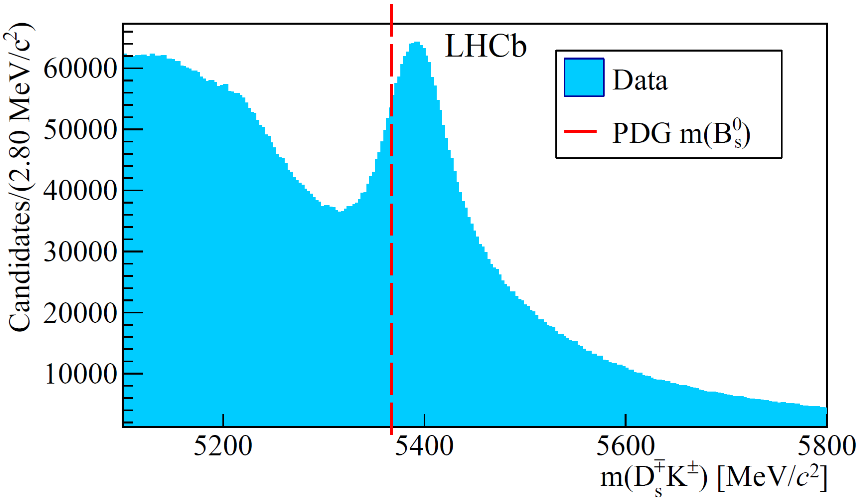

Figure 4.3: The $m(D_s^{\mp}K^{\pm})$ invariant mass distribution after the trigger, preselection and MVA requirements.

The above-presented figure shows the $m(D_s^{\mp}K^{\pm})$ invariant mass distribution after the preselection step and after applying the MVA technique, which reduces the combinatorial background. The red line indicates expected invariant mass of the B_s^0 meson. However, the mass is significantly shifted toward higher values, and does not match expected value of 5366.77 MeV/c^2 [2]. In the consideration of the B_s^0 meson decay, there are many different types of potentially misidentified backgrounds. The first misidentification can occur on the companion track when a kaon $K^{\pm}$ is wrongly identified as a $\pi^{\pm}$. The substantial peaking background is due to $B_s^0 \to D_s^- \pi^+$ decay with much higher (more than one order of magnitude) branching fraction to the $B_s^0 \to D_s^{\mp}K^{\pm}$ as indicated in Table 4.2. During the reconstruction process the π mass (139.57 MeV/c^2 [2]) is substituted by a higher K mass (493.68 MeV/c^2 [2]) pushing the invariant $m(D_s^{\mp}K^{\pm})$ mass towards higher values which explain the peak shift. The $B_s^0 \to D_s^- \pi^+$ decays are suppressed to a sufficient level by requiring the $DLL(K-\pi) > 5$ on the companion track.

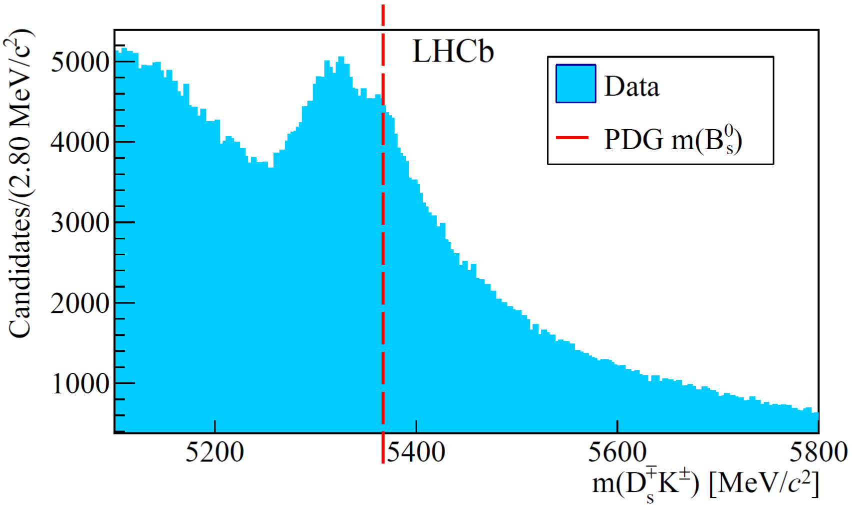

Figure 4.4: The $m(D_s^{\mp}K^{\pm})$ invariant mass distribution after the trigger, preselection, MVA and $DLL(K-\pi) > 5$ on $K^{\pm}$ companion requirements.

After applying an additional $DLL(K-\pi) > 5$ requirement, a great improvement can be seen in Figure 4.4. However, this time the peak is shifted towards lower invariant masses due to lack of the PID requirements on the D_s^- final state particles. Another two background contributions must be considered involving the D_s^- meson misidentification to either the $\overline{\Lambda}_c^-$ or D^- particles. Similarly to the $B_s^0 \to D_s^-\pi^+$ mode, branching fractions of the decays $\overline{\Lambda}_b^0 \to \overline{\Lambda}_c^-\pi^+$ and $B^0 \to D^-\pi^+$ are of the order of 10^{-3} (Table 4.2), i.e. a one order of magnitude higher than the signal mode. If a kaon K^- with the same charge as the D_s^- meson is misidentified as a π^-, then it forms the $D^- \to \pi^-K^+\pi^-$ meson. On the other hand, when a kaon K^- with the same charge as the D_s^- is misidentified as the antiproton $\bar{p}$, a contribution from the $\overline{\Lambda}_c^- \to \bar{p}K^+\pi^-$ should be considered. The D^- ($\overline{\Lambda}_c^-$) misidentification changes the invariant mass towards lower (higher) value. The first order suppression of these days might be achieved by requiring the PID selection on the D_s^- final state particles. These are: $DLL(K-\pi) > 5$ for both kaons and $DLL(K-\pi) < 5$ for a pion. The $m(D_s^{\mp}K^{\pm})$ invariant mass after the additional PID selection is shown in Figure 4.5.

While a signal peak is in an expected place (red line), the contributions from the $\overline{\Lambda}_b^0 \to \overline{\Lambda}_c^-\pi^+$ and $B^0 \to D^-\pi^+$ decays are not fully suppressed. Especially, the contribution from the $\overline{\Lambda}_b^0 \to \overline{\Lambda}_c^-\pi^+$ is well noticeable on the right side of signal peak. On the other hand, a tighter full phase-space PID requirement would significantly reduce the signal yield. Even if the $DLL(K-\pi) > 10$ requirement suppresses more

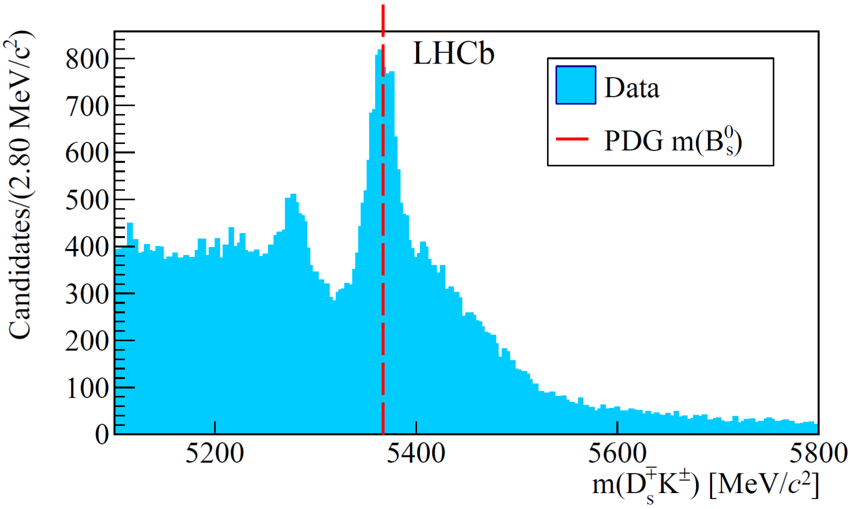

Figure 4.5: The $m(D_s^{\mp}K^{\pm})$ invariant mass distribution after the trigger, preselection, MVA, the $DLL(K-\pi)>5$ on $K^{\pm}$ companion track and the generic PID selection for D_s^- final state particles requirements.

misidentified $\pi^{\pm}$ particles, its efficiency on the kaon sample is about 10% lower than a looser requirement of $DLL(K-\pi)>5$. Therefore, instead of full phase-space requirements additional dedicated vetoes are applied. The $K^-K^+\pi^-$ invariant mass is calculated under the $\pi^-K^+\pi^-$ ($\bar{p}K^+\pi^-$) hypothesis substituting the mass of the kaon K^- by a mass of the pion π^- (antiproton $\bar{p}$). Respective invariant masses are shown in Figure 4.6 for the $\pi^-K^+\pi^-$ (left) and $\bar{p}K^+\pi^-$ (right) distributions.

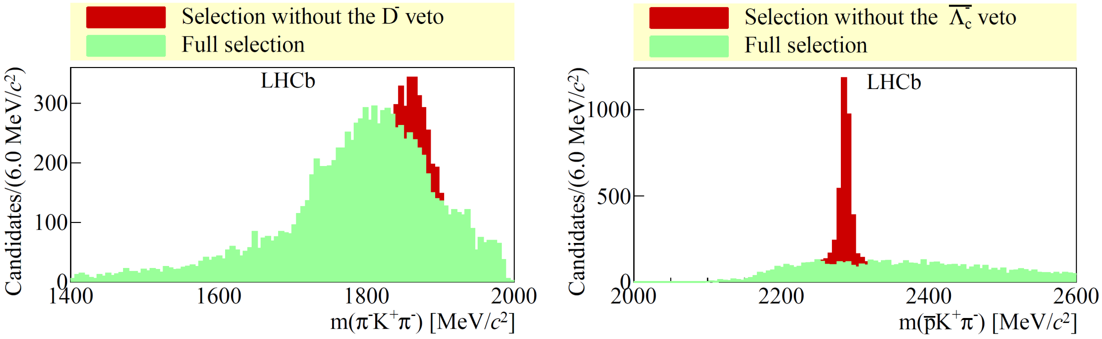

Figure 4.6: The $m(\pi^-K^+\pi^-)$ (left) and $m(\bar{p}K^+\pi^-)$ (right) invariant masses distributions before and after applying the dedicated vetoes.

Before applying dedicated vetoes, and after the full phase-space PID selection, a peaking structures are still visible. The veto applies tighter PID requirements for the candidates falling 30 MeV/c^2 around the nominal $D^-/\overline{\Lambda}_c^-$ masses [122]. This requirements are $DLL(K-\pi) > 5$ for the candidates falling within $[1839, 1899]$MeV/c^2 (D^- veto) and $DLL(K-\pi)$ - $DLL(p-\pi) > 5$ for the events within $[2255, 2315]$ MeV/c^2 ($\overline{\Lambda}_c^-$ veto).

The invariant mass distribution after the full selection is shown in Figure 4.7. At this stage, all dominant fully reconstructed background contributions are suppressed to the level which allows performance of the measurement. As shown with a usage of this example, the distinction power of the PID requirement plays a crucial role in performing physics analyses in the LHCb experiment. Keeping the PID performance in Run III at the same level as in Run II (Figure 3.5) should allow sufficient background suppression.

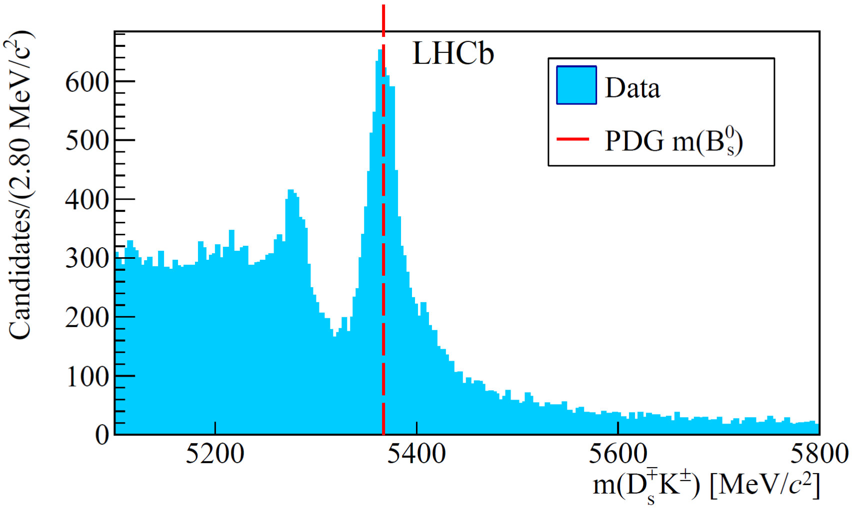

Figure 4.7: The $m(D_s^\mp K^\pm)$ invariant mass distribution after the trigger, preselection, MVA, $DLL(K-\pi) > 5$ on the $K^\pm$ companion track, the generic PID selection for D_s^- final state particles and veto requirements.

Chapter 5

Elementary Cell Quality Assurance

The following chapter presents the main part of the thesis, which is the overview of the Elementary Cell Quality Assurance (ECQA) that was performed at the University of Ferrara. At the beginning, the experimental test setup used for the EC quality control is presented. It is followed by the EC assembling procedure and the ECQA test protocol. Subsequently, the development of the automated software used to validate the ECs is described. At the end, the offline data analysis is discussed with a great emphasis put on the SIN.

5.1 Overview

For the LHCb upgrade, the RICH detectors are completely redesigned by replacing the current HPDs by the MaPMTs. The MaPMTs are installed on the FE electronics that compose a final product called the EC, which is a basic building unit of the new detection system. In order to assure the highest possible reliability, consistency and efficiency of the new system, the ECQA is performed. The ECQA provides crucial information whether an EC is suitable for the installation inside the RICH detectors or is rejected. The measurements characterising the FE electronics and the MaPMTs are performed. The acquired data is analysed to find out how the new photodetectors perform before reaching their final destination at CERN. The ECQA takes place in two facilities: Ferrara, Italy and Edinburgh, United Kingdom. The total amount of ECs to be tested is split in half between these two institutions. The required components (i.e. Bbs, Bkbs, FEBs, metal chassis and MaPMTs), shipped in batches, are assembled and tested simultaneously on-site providing uninterrupted process of quality assurance.

5.2 Test Setup

There are in total four identical test stations that operate in the test facilities. The first facility, located in Ferrara, is a host to the Station 1 and 2 while the second one, located in Edinburgh, is a host to the Station 3 and 4. Each setup (Figure 5.1) consists of a dark box (Figure 5.2) which is a light-proof box where up to four ECs can be mounted at once.

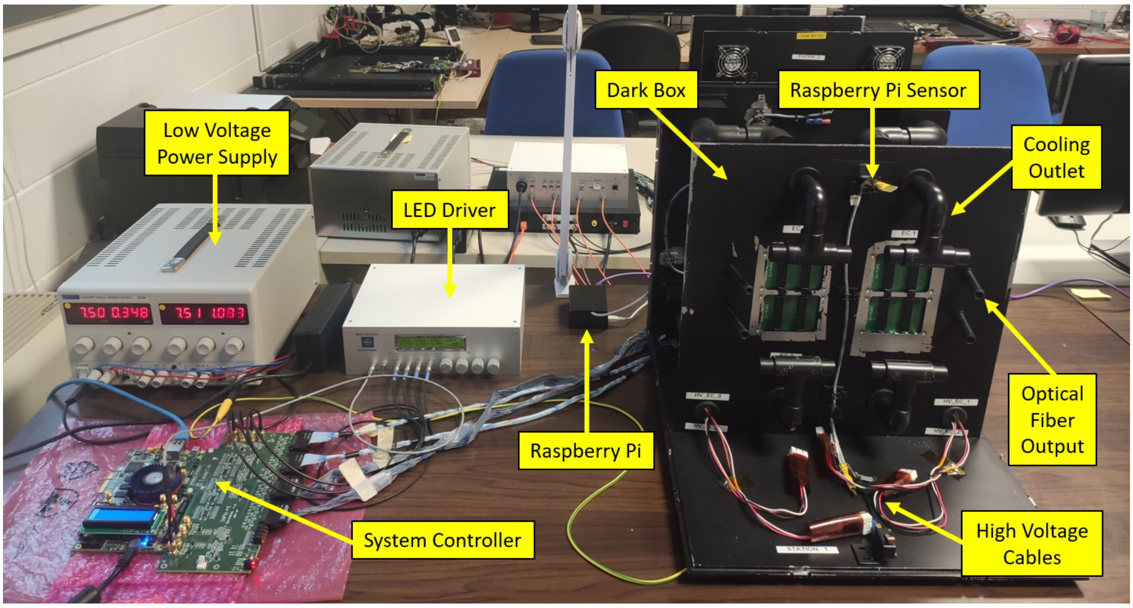

Figure 5.1: The Station 1 test setup. On the right, an unsealed dark box is shown.

The box, engineered by the Edinburgh group, is designed to be light-tight as it is essential to create conditions that cannot harm MaPMTs during the measurements at the high voltage (HV). A possible source of a light leakage that exposes photodetectors (e.g. an environmental light during the HV operation) could consequently contribute to irretrievable damages. The internal structure of the dark box is divided into two equal spaces separated by a black panel in the middle. The black panel is an additional protection from light as it suppresses potential photons from passing through cables and service holes. The front half of the box is a space dedicated for the measurements of the ECs whereas the back half is a space devoted to electronics, e.i. two DBs containing two ALTERA MAX10 FPGAs for each DB. The backside of the dark box, where cables and service holes are placed, is covered by a black mat that enhance the impermeability of the box to light. Photons are transferred to the dark box only in a controlled way from an LED driver. The LED driver is connected to four optic fibers that are inserted in the backside of the dark box and are extended to the second half of the box. The optic fibers face the wall where a mirror is installed, allowing photons to reflect directly on top surfaces of MaPMTs providing uniform illumination.

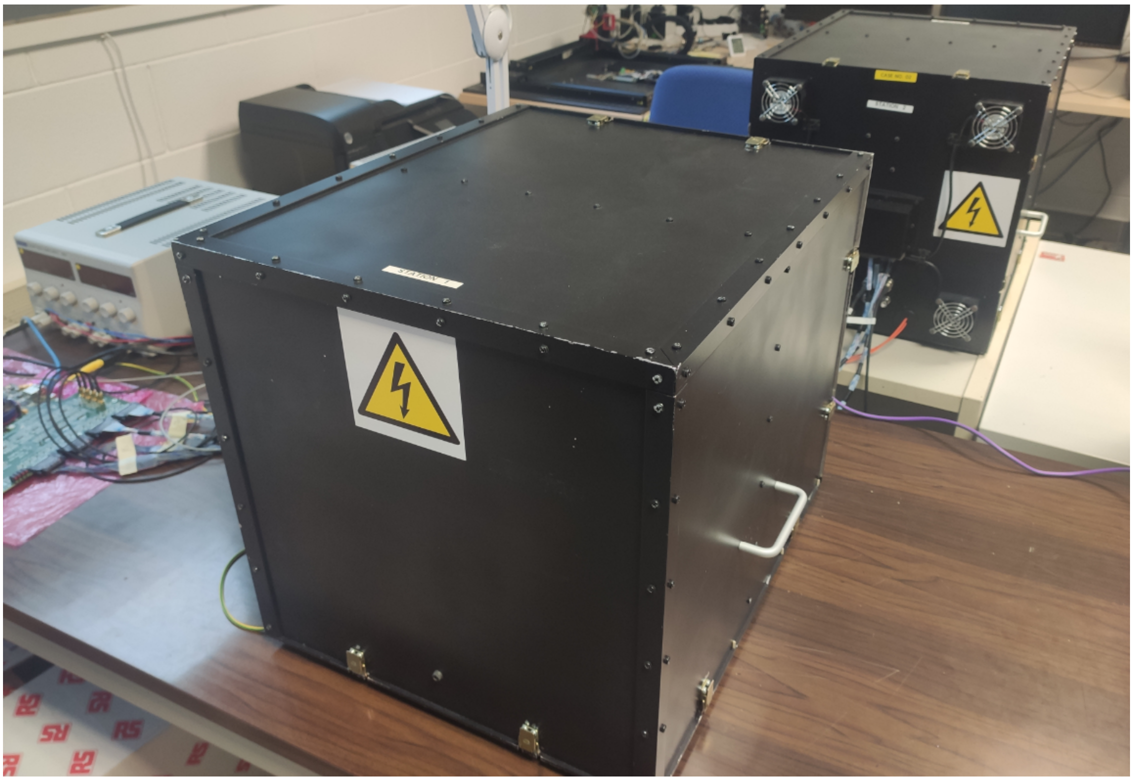

Figure 5.2: Two identical dark boxes used for the ECQA procedure in Ferrara: the dark box of Station 1 (foreground) and the dark box of Station 2 (background).

The MaPMTs are connected to the HV which is delivered from the HV ISEG ECH 242 [123] crate equipped with the ISEG crate controller model CC24 Master [124] and the two 8-channels HV power supply ISEG boards EHS 8020n [125]. Both stations are connected to a single HV crate, but to different boards. The first four channels of the first board are reserved for four Bbs installed in the first station while the second four channels of the second board are occupied by four Bbs installed in the second station. As environmental temperature and humidity influence the MaPMTs performance, they are monitored by Raspberry Pi (RPI) mini computer and controlled by the air-cooling fan system. The environmental readings are recorded every ten seconds by a RPI using a dedicated LabVIEW software (Figure 5.3), which is incorporated in the automated ECQA system. The program extracts the data from a RPI using Transmission Control Protocol (TCP) and every hour saves environmental measurements in a separate output file. Airflow provided by the fan system, is directed on ECs from underneath that goes out in the upper part of a box allowing a proper air circulation. The cooling system is also provided for the DBs equipped with built-in fans. The DBs and the fans, are powered by a low voltage (LV) power supply Aim TTi EX354RT [126], located outside of the dark box. In front of the LV power supply, a system controller, based on Cyclone V GT FPGA development board, is placed. It is connected to a pc via Gbit Ethernet interface and to the DBs through a Universal Asynchronous Receiver/Transmitter (UART) interconnection module. The data acquisition (DAQ) is done by an automated control software described in Section 4.6. The software configures the CLAROs and DBs, controls the HV crate, triggers the LED driver to generate light pulses and manages the validation measurements.

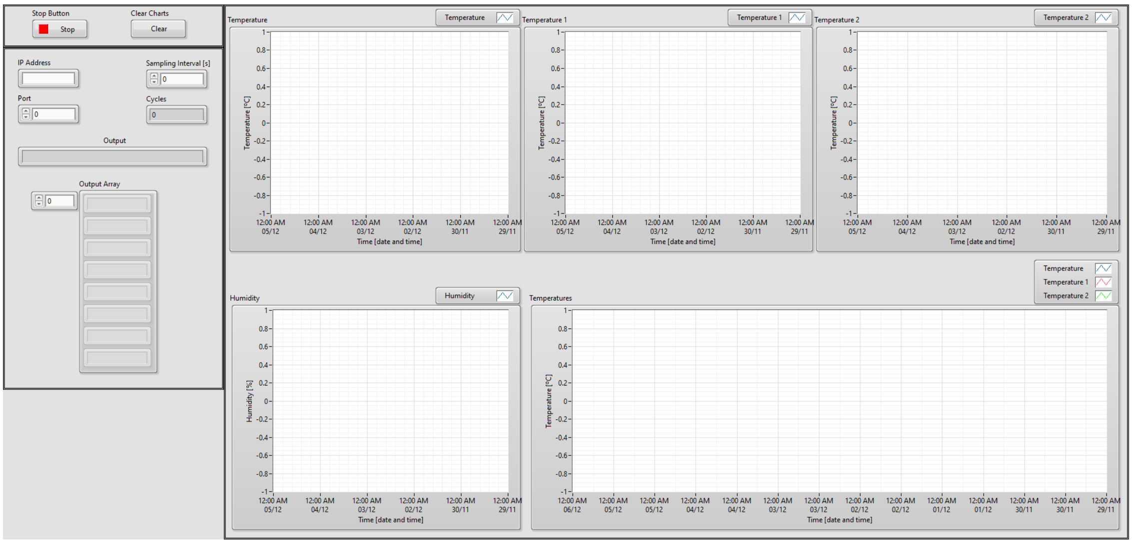
Sampling Interval [s] 0
Port 0
Cycles 0
Output Array 0

Figure 5.3: The temperature and humidity reading software. The three upper panels are used to plot temperature in time. They are combined and shown together in the bottom right panel. On the lower left side, a panel for humidity is presented. The readings are acquired from four sensors placed inside a dark box. To the most left, a panel for parameters and output readings obtained from RPI is located.

5.3 Assembling Procedure

Due to high sensitivity and fragility of the EC's components, a detailed assembling procedure has been created. It requires usage of an electrostatic discharge (ESD) safe equipment together with protection gloves during the manipulation of components. As the orientation of components is essential during the assembly, it is necessary to navigate the bottom and top side of each component (i.e. Bb, FEBs and Bkb). The orientation is found by localising the ground that indicates the top side or white line which corresponds to the bottom side (Figure 5.4). The mentioned components have to be always mutually oriented top-to-top and bottom-to-bottom.

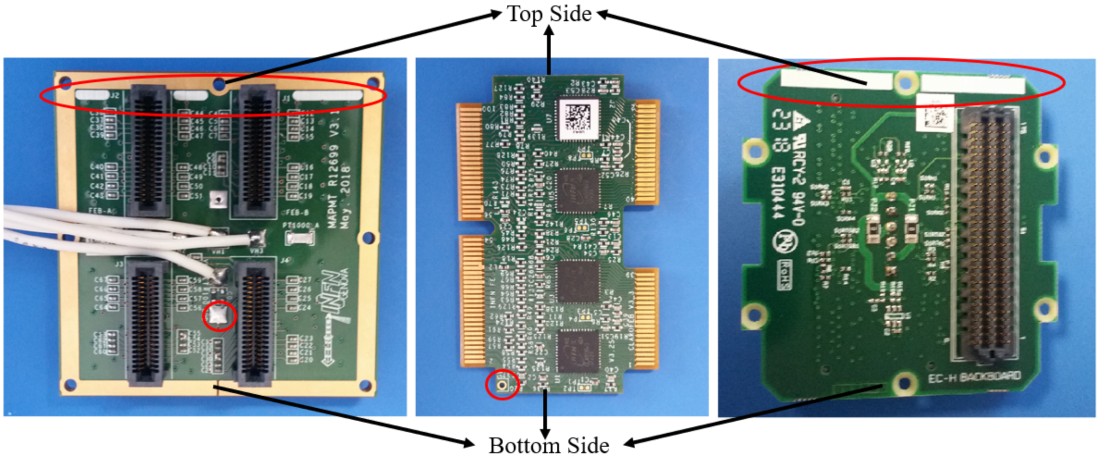

Figure 5.4: The orientation of components of an H-type EC (from left: Bb, FEB module, Bkb).

Subsequently, either four FEBs (for an R-type EC) or two FEBs (for an H-type EC) are mounted on a Bb (R-type or H-type). The next step consists of assembling an aluminum case with adequate type of screws and required torque. More details of this procedure are described in the Appendix A. After a Bkb is put together, a built unit is ready to be inserted in a dark box. The first measurements are strictly related to the electronics hence no MaPMTs are installed yet. During the ECQA process, either four 1" MaPMTs (R-type) or one 2" MaPMT (H-type) are introduced composing the final product called the EC.

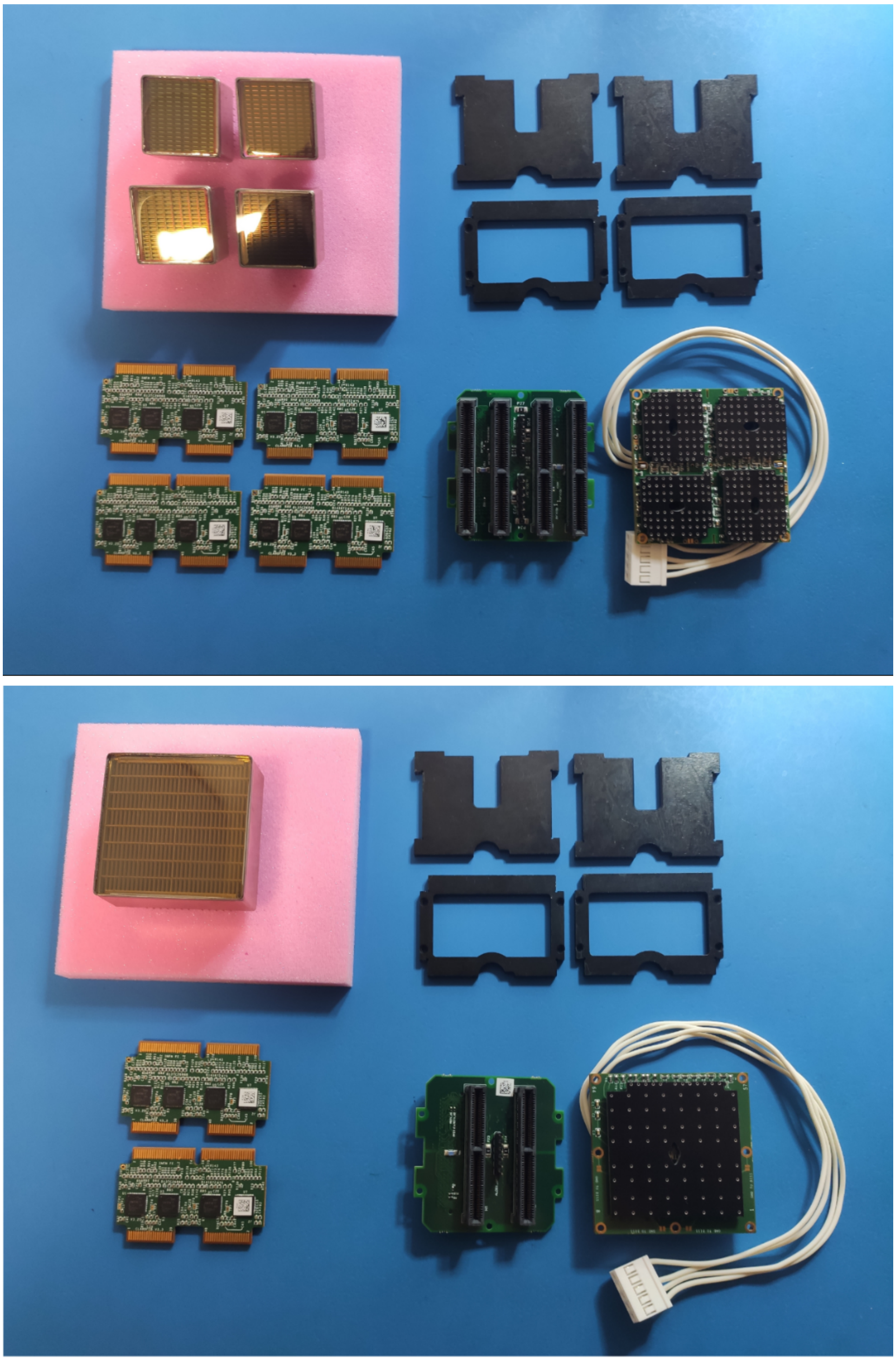

Figure 5.5: Pictures presenting components for the R-type (upper picture) and H-type (lower picture) EC. Either four or two FEBs (bottom-left), four or one MaPMT (top-left), four aluminum cases (top-right), Bkb and Bb (bottom-right) are required to fully assemble EC-R or EC-H.

5.4 Organization

Each set of ECs, mounted in a dark box, is called a load and a four-digit identification number is assigned to it. A load usually represents four ECs as it is the maximum capacity of a dark box but if necessary, fewer ECs can be applied. As there are two possible types of an EC, it is required to provide the type of a load, either with a letter "R" for the R-Type or a letter "H" for the H-Type. It is not possible to test mixed ECs as the ECQA software works in a binary way when it comes to the type of ECs. The third and the last information, that is required, is the station number which can be either S1 or S2 (for the stations in Ferrara) or S3 or S4 (for the stations in Edinburgh). The loads are numbered consecutively and the numbering is station and EC-type independent. All this key-information are separated by an underscore symbol composing the main directory of a specific load.

Load_number_type_station

As an example, a 50th H-type load mounted in the second station is named Load_0050_H_S2. Inside this directory, the acquired data of each test is stored. Additionally, there are two folders. The first one named "PDF" is responsible for storing the generated analysis plots in the pdf format obtained during the measurements, while the second folder named "QR_Codes" is accountable for storing quick response (QR) codes of a related set of ECs' components of that load.

Each electronic component and each MaPMT have their unique QR code. The QR codes are scanned in order to know which components compose a particular EC. A dedicated software (Figure 5.6) has been developed that encodes the QR codes in separate text files. A file name depends on the QR code of a scanned Bkb. It is necessary to provide an operator's name, a facility location, a type of the EC, a load number, a station number and the EC position. Upon providing all the information, the QR codes of the components can be scanned during the assembly procedure. The sequence is initialised with the QR code of a Bb, followed by the FEB 0, 1, 2, 3 (R-type) or FEB 0, 1 (H-type) and is finished by scanning the QR code of a Bkb. The numbering of FEBs can be followed by examining Figure 5.7. A position of the EC can be set to four different places, that is: 0 (TL - Top-Left), 1 (TR - Top-Right), 2 (BR - Bottom-Right) and 3 (BL – Bottom-Left).

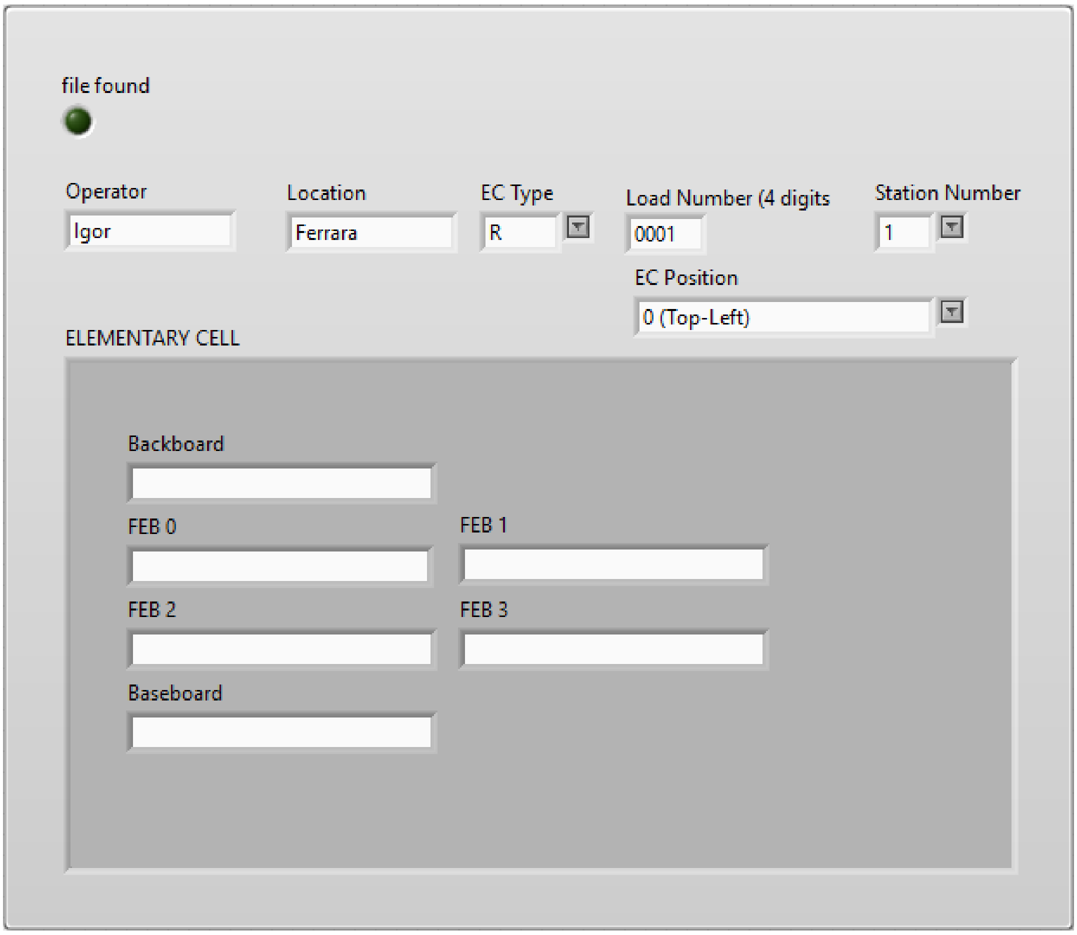

Operator: Igor

Location: Ferrara

EC Type: R

Load Number (4 digits: 0001

Station Number: 1

EC Position: 0 (Top-Left)

Backboard:

FEB 0:

FEB 1:

FEB 2:

FEB 3:

Baseboard:

Figure 5.6: The QR code scanning software for the components of the ECs.

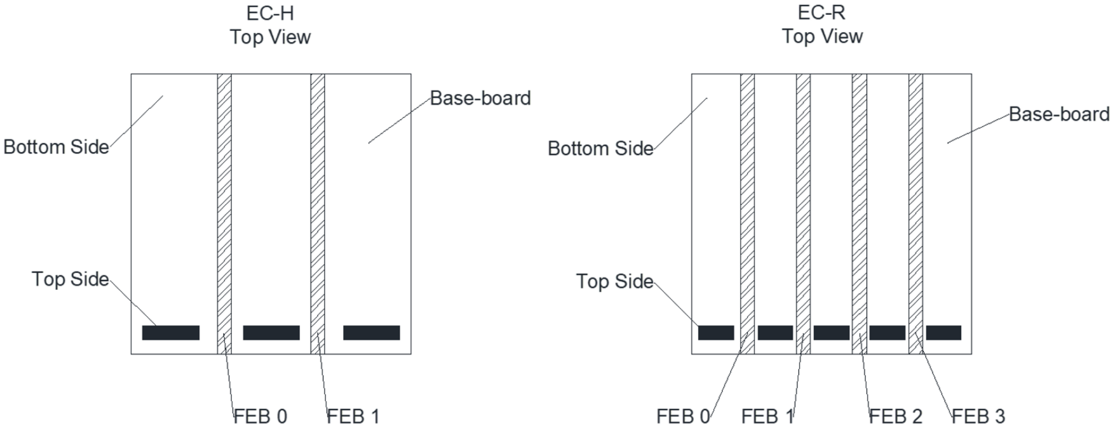

Figure 5.7: A scheme representing the numbering of FEBs of the H-Type and the R-Type EC. Black rectangles between the FEBs indicate a white line that corresponds to the top side.

5.5 Test Protocol

When a load is assembled and mounted in a dark box, the ECQA software is launched. After specifying the load number, its type and the station number, a connection between the software and the system controller is established. The software connects to the HV crate in order to monitor the applied voltages and to the RPI for the environmental humidity and temperature monitoring. The references to the output filenames of each test are collected in the Appendix B.

5.5.1 Communication Check

After assembling and mounting a load into the station, the first test, so-called `S-Curve Comm Check` is performed. The test derives directly from the S-Curve test (point 4), with the modification of the DAC step parameter set to 50 (61mV). Such parameter modification checks a properly working communication with CLARO ASICs and ensures that a transition is present in every CLARO channel. The number of pulses are provided in the range from 0 to 1000. After the data is acquired, a dedicated script checks the first and the last DAC step. The test fails if the first step has more than 5 counts or if the last step has less than 950 counts. The thresholds vary slightly from the exact range values as there might occur unexpected oscillations in the channels. The script also verifies if a channel is functional - when the counts of a channel equal always to 0, then the channel is likely to be broken, whereas when the counts of a channel yield always 1000 or more, then the channel is noisy. Additionally, the script checks if there are any high variations between the steps. The test is flagged as positive if no above-mentioned errors appear. The problematic EC needs to be dismounted from the station and their connectors cleaned using a compressed air. Then the EC can be mounted back and the test is performed again. If the following series of actions do not solve the problem, the defective channel has to be navigated and the corresponding FEB needs to be replaced by a new FEB module. The QR code of the substituted FEB needs to be updated. The defective component is then put aside for the future investigation as it is likely that during the assembly of the aluminium frame, a resistor located in the corner of a FEB got damaged.

5.5.2 Low Voltage (LV) Measurements

The FPGAs 12 bit, 8-channel analog-to-digital converter (ADC) channels are read-out and the values of temperature for FEB 0, FEB 1, Bkb and two temperatures of Bb together with the current of FEB couple and the CLARO V_{dd} for the FEB 0 and FEB 1 are recorded. The measurements are performed two times in total, for the CLARO channels that are not configured at all, and for CLARO channels that are configured at `0x314` (threshold 20). The hexadecimal configuration (e.g. `0x314`) sets the whole CLARO register. It is converted to the binary configuration where first six bits correspond to the threshold (Table 3.1). The corresponding decimal notation of the threshold (e.g. threshold 20) is used in the ECQA analysis.

5.5.3 HV Measurements and Installation of MaPMTs

The first HV measurement is performed on the ECs that are incomplete as the MaPMTs are not installed yet. The HV is turned on at 1000 V with the ramp-up speed of 50V/s and is left for 1 minute for the currents to stabilize. Subsequently, the actual measurements take places. The currents of a Bb and applied voltages are monitored for 1 minute. Then, the average current of a Bb and applied voltage is calculated for each EC. At the end, the HV is turned off and the photodetectors are ready to be scanned and installed. Figure 5.8 presents the interface of the scanning software for the MaPMTs incorporated in the main automated software.

EC 0
EC CODE
R2118902012900
PMT CODE
PMT 0 FB0718
PMT 1 FB0100
PMT 3 FA1935
PMT 2 FB0655

EC 1
EC CODE
R21190304052000
PMT CODE
PMT 0 FA1402
PMT 1 FB0060
PMT 3 FB0837
PMT 2 FB0054

Test RESULT
DONE OK

EC 3
EC CODE
R21190303031800
PMT CODE
PMT 0 FA1526
PMT 1 FA1957
PMT 3 FA1181
PMT 2 FA1744

EC 2
EC CODE
R21190304056500
PMT CODE
PMT 0 FA0812
PMT 1 FA1976
PMT 3 FB0783
PMT 2 FB0811

Figure 5.8: The interface of the MaPMTs scanning software. A green color of inputs refer to the installed ECs, otherwise they are marked as a red color.

The QR code scanning and the installation of the MaPMTs are done in a succession, one after another. For the R-Type ECs, the MaPMTs are mounted and scanned in the following sequence: 2 (bottom-right), 1 (top-right), 3 (bottom-left) and 0 (top-left) starting from the EC 2, 1, 3, 0. Having mounted all the MaPMTs (Figure 5.9), it is necessary to perform the Communication Check (point 1) again to ensure that during the MaPMTs installation process, no communication between CLARO channels is lost as well as to check if the connectors work impeccably. After passing the initial procedure, it is mandatory to seal a dark box as the next HV measurement is done on the full ECs with the installed MaPMTs. The second HV measurement is done in exactly the same way as the first HV measurement but this time MaPMTs are present. After the second measurement is completed, the last step requires the HV to be set to 1050 V for 1 minute to calculate the average current of Bbs, which are then used as the current limits for future HV training (point 5).

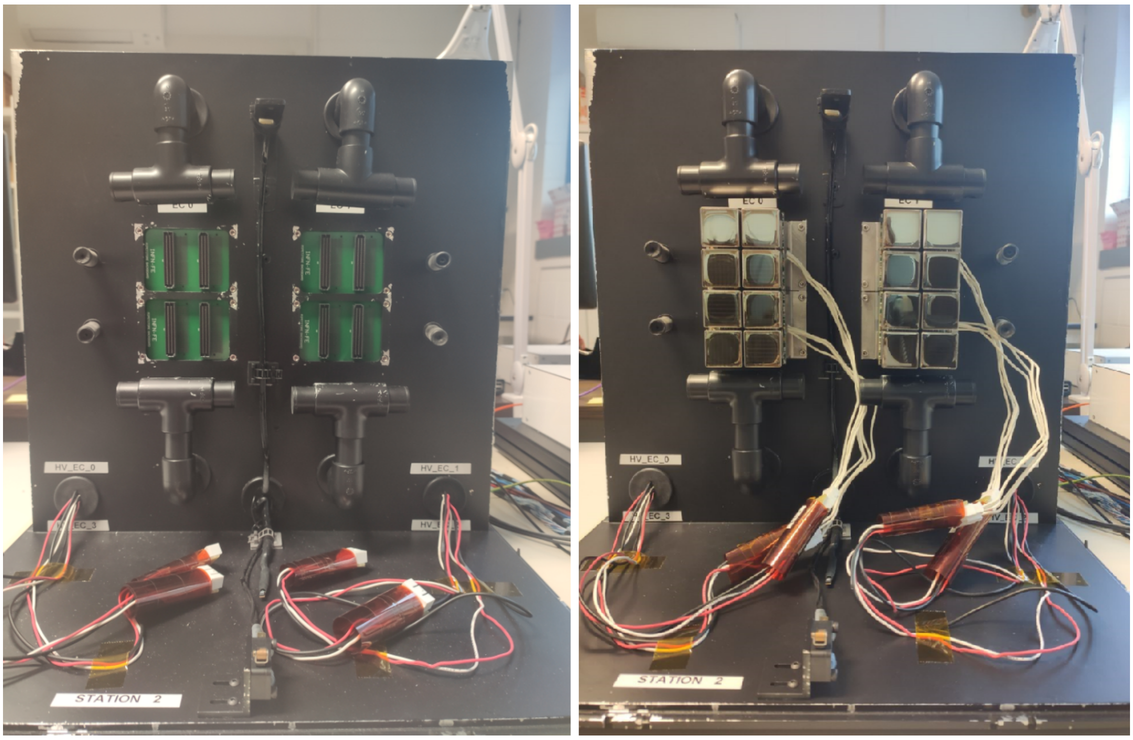

Figure 5.9: Picture presenting the empty station (left side) and fully mounted station with four ECs of type-R (right side).

5.5.4 DAC Scan Test

All the CLARO channels undergo the DAC Scan test from 0 to 600 DAC (0 to 732mV) with a DAC step equal to 1 DAC (1.22mV). The injected charge from 0 to 1000 number of pulses is provided. The test is performed for six different configurations. The first three thresholds for the offset bit 0 are set as 10 20 and 30, which are the configurations `0x30A`, `0x314` and `0x31E` respectively and the next three thresholds for the offset bit 1 are set as 42, 52 and 62 which are the configurations `0xB2A`, `0xB34` and `0xB3E`. When the measurement is finished and the data acquired, six text files for all the thresholds are generated. A dedicated script fits the S-Curves and finds the transition points for all the CLARO channels. In addition, the results are presented graphically in the pdf format. It is unlikely that there is a CLARO channel with no transition since the `S-Curve Comm Check` test has been already passed at this point. However if that occurrence appears, the problematic CLARO channel is navigated and the corresponding FEB is replaced.

5.5.5 HV Training

As the next measurements are related to the MaPMTs specifically, the ECs are powered with HV set at 1050V for 10 hours with the current limit established at the end of HV measurements. The stand-by allows the MaPMTs to discharge substantial amount of electronic noise thus providing better performance during the DCR and SIN measurements.

5.5.6 Threshold Scan Test

After the HV training is finished, the HV is decreased to 1000 V. During the test, the threshold ranges from 63 to 0 and is done two times for offset bit 0 and 1. The LED driver sends 100 k pulses at a 100 kHz frequency for each threshold step. After the measurement is finished, a dedicated script is executed and determines the threshold corresponding to the first edge after the pedestal for all the CLARO channels. Then the working point of each CLARO channel is calculated as a sum of the corresponding threshold and five more thresholds. Additional five thresholds ensure perfect balance between the noise and the signal as the noise is omitted significantly and the signal is not cut much. For the offset bit 0, only small portion of the CLARO channels have a pedestal hence the working points are established for the offset bit 1. If for some reasons the working point cannot be determined, then the automated software prints an error and the corresponding faulty FEB has to be put aside.

5.5.7 Dark Count Rate Test

As in the previous test, the HV stays at 1000 V. The measurement is executed two times for two different configurations. At first, all the CLARO channels are set to a configuration equal to `0x307` (threshold 7), while the second measurement loads the optimised threshold (working points) that have been obtained during the Threshold Scan, meaning that each CLARO channel might have a different configuration. The measurements are performed in 100 s time window. After the test is finished, a dedicated script produces the overview of the uniformity of the DCR for all the MaPMTs and checks if the DCR does not exceed 1 kHz per channel.

5.5.8 Signal Induced Noise Test

As SIN depends greatly on the provided HV, the test is performed four times at four different voltages - 1000 V, 950 V, 900 V and 850 V. This time, there is no fixed configuration and only optimised configuration is loaded for the CLARO channels. The time interval is DAC-dependent and one step (period between two consecutive signals) is equal to 25 ns. The whole spectrum is established to 256 steps (6.4 μs). When the test is finished, a dedicated script generates the overview of the histograms of the SIN, SIN Fraction (Equation 3.10) and S/N Ratio (Equation 3.11). In addition for each CLARO channel, a corresponding SIN spectrum is produced. There are no constraints concerning the SIN.

When all the measurements are performed, it is essential to check the software logs and revise the generated plots to determine if a tested EC passes the ECQA test protocol. The scripts responsible for the data analysis, mentioned in the test protocol, are covered in the Section 4.7. The usual time of the complete ECQA procedure takes approximately 16 hours (with the 10 hours of HV training). The assembly of the ECs is done during the measurements not requiring manual interference and is performed in advance to the load that is to be put in the next days.

5.6 Software

The DAQ is managed by a control software that has been created in python language and National Instrument LabVIEW 2017 64-bit environment on CentOS7 operating system. The fully automated software performs the required tests mentioned in the procedure, initialises the scripts responsible for the data analysis, controls the HV and configures the DBs and CLARO chips through a system controller. The development of the software is divided and organised into four stages: the development of the low-level python functions, LabVIEW commands, standalones and the final ECQA software. The phases of the development are at the same time the architectural structure of the software. An illustrative workflow, presenting how the sectors communicate with each other, is reported in Figure 5.10.

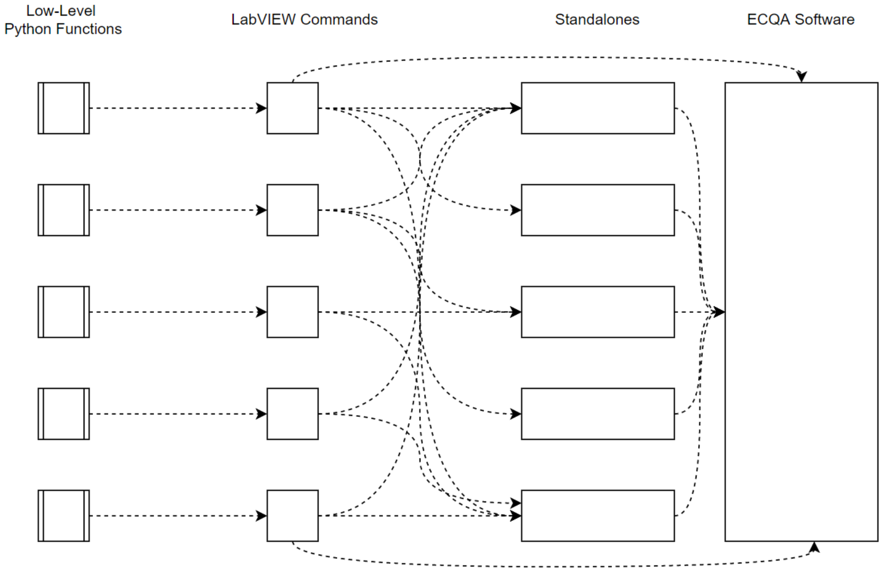

Figure 5.10: An illustration of the workflow in the ECQA control software.

5.6.1 The Low-Level Python Functions

The base core of the ECQA software constitutes of the low-level python functions, that perform strictly defined commands. Their task is to communicate with a system controller and subsequently a DB, which executes the initialised command. Depending on a function, the parameters can be provided and if applicable, the output is expected. As an example, the `cmd_CFG` function configures selected CLARO chips with a provided input parameter, whereas the `cmd_RCFG` function reads a configuration of selected CLARO chips, hence the output parameter is returned. There are also functions that require input and output parameters simultaneously while there are some that do not require parameters at all. There are 28 low-level python functions that are used for the test procedure.

5.6.2 LabVIEW Commands

To comfortably navigate through the low-level python functions in a LabVIEW environment, a graphical user interface (GUI) has been designed as an upper hierarchy level. For each python function, its equivalent Virtual Instrument (VI), called "LabVIEW command", is created. The VIs take the exact same dimensions of vectors and clusters as their python counterpart and are created in one-to-one compliance. As an example, a python function that reads the counter of CLARO chips named `cmd_HITCOUNT_READ` is linked directly to LabVIEW command `cmd_HITCOUNT_READ_ECQA.vi` and no other VI can initialise that command. A graphical representation of this particular VI is shown in Figure 5.11.

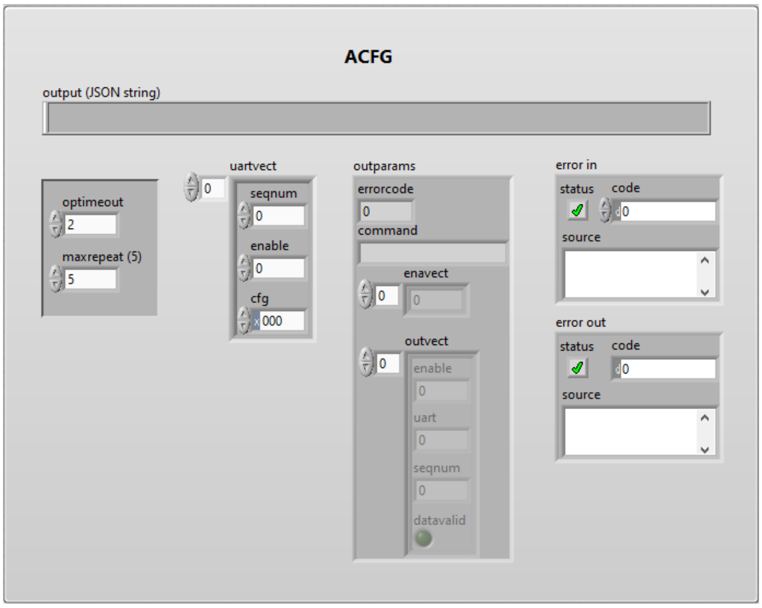
ACFG

output (JSON string)

optimeout: 2
maxrepeat (5): 5

uartvect: 0
seqnum: 0
enable: 0
cfg: x000

outparams
errorcode: 0
command:
enavect: 0 | 0
outvect: 0
enable: 0
uart: 0
seqnum: 0
datavalid

error in
status: ✓
code: 0
source:

error out
status: ✓
code: 0
source:

Figure 5.11: A control panel of the `cmd_ACFG_ECQA.vi` that operates directly on the `cmd_ACFG` function which configures all the channels of selected CLARO chips with the provided configuration parameter.

The low-level python functions and the LabVIEW commands are able to communicate with each other and are able to perform predefined tasks by initialising `syscmd_opens_ECQA.vi` and `cmd_NET_OPEN_ECQA.vi` (Figure 5.12). The `syscmd_open` function initiates the python daemon that creates a python-LabVIEW interface whereas the `cmd_NET_OPEN` launches the communication with a system controller after specifying its IP address and communication port. They are initialised at the beginning of the procedure.

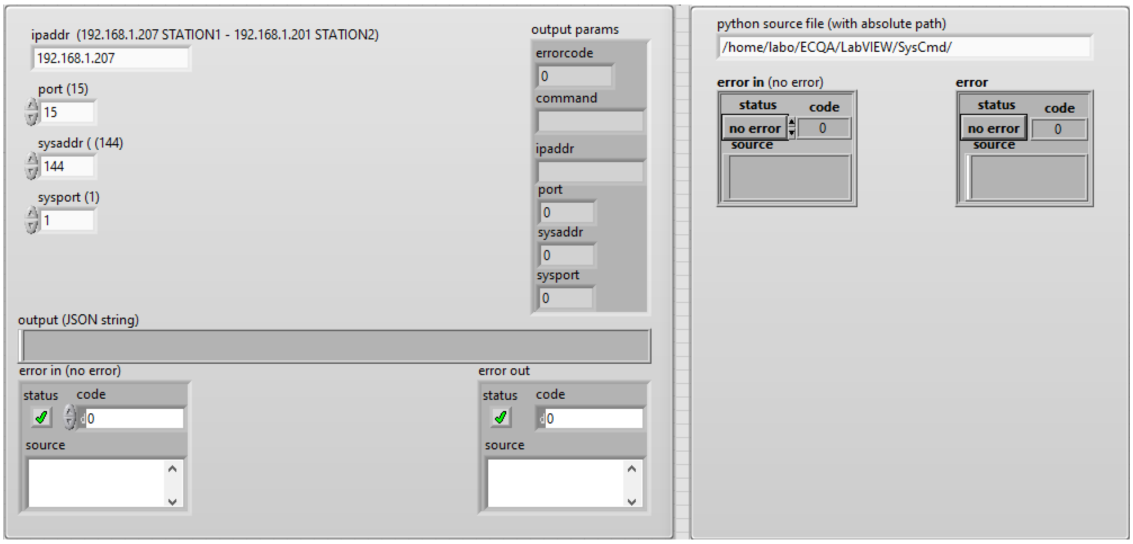

ipaddr (192.168.1.207 STATION1 - 192.168.1.201 STATION2): 192.168.1.207
port (15): 15
sysaddr ((144): 144
sysport (1): 1
output params
errorcode: 0
command:
ipaddr:
port: 0
sysaddr: 0
sysport: 0
output (JSON string):
error in (no error): status ✓ code 0 source
error out: status ✓ code 0 source

python source file (with absolute path): /home/labo/ECQA/LabVIEW/SysCmd/
error in (no error): status no error code 0 source
error: status no error code 0 source

Figure 5.12: Control panels of the communication LabVIEW commands. On the left side, the VI for opening the communication with a system controller is shown whereas on the right side, the VI for initialisation of python-LabVIEW daemon is presented.

5.6.3 Standalones

Another upper level of hierarchy in LabVIEW environment has been created to run the actual measurements. The so-called "standalones" are built on top of the LabVIEW commands and are used to perform the required ECQA tests. The standalones correspond directly to the actual tests presented in the test protocol:

- `S_Curve_Comm_Check_Standalone.vi` - Communication Check,
- `Current_Meausrements_Stanalone.vi` - LV and HV Measurements,

- `S_Curve_Standalone.vi` - DAC Scan Test,
- `Threshold_Scan_Standalone.vi` - Threshold Scan Test,
- `CFG_Loader_Standalone.vi` - Threshold Configurator,
- `Dark_Counts_Standalone.vi` - DCR test,
- `SIN_Standalone.vi` - SIN test.

The `Configurator_Standalone.vi`, not mentioned in the test protocol, configures the CLARO channels for the optimised configuration obtained in the Threshold Scan. The standalones are able to run a specific measurement without any interruption. As an example, the control panel of the `SIN_Standalone.vi` is reported in Figure 5.13. It is necessary to provide information concerning a load path (load number, EC type and station) and all the other parameters required for the SIN measurement. Each iteration of the test (four different voltages) is needed to be launched separately, one after another, each time specifying all the required parameters. It is inconvenient due to time inefficiency and possibility of making errors.

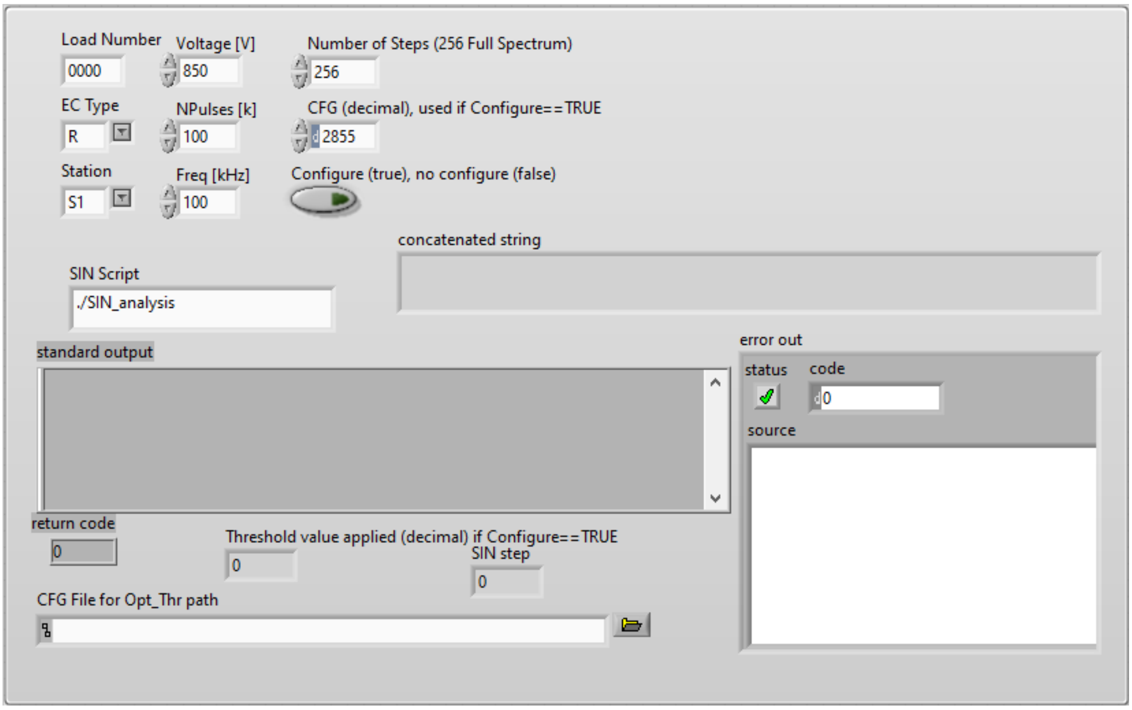
Load Number: 0000
Voltage [V]: 850
Number of Steps (256 Full Spectrum): 256
EC Type: R
NPulses [k]: 100
CFG (decimal), used if Configure==TRUE: 2855
Station: S1
Freq [kHz]: 100
Configure (true), no configure (false)
concatenated string
SIN Script: ./SIN_analysis
standard output
error out
status: ✓
code: 0
source
return code: 0
Threshold value applied (decimal) if Configure==TRUE: 0
SIN step: 0
CFG File for Opt_Thr path

Figure 5.13: A control panel of the `SIN_Standalone.vi`.

5.6.4 The ECQA Software

To solve the above-mentioned obstacles, the highest level of hierarchy has been developed. The ECQA software is based on the LabVIEW commands and the standalones. The software is totally automated with an exception of the MaPMTs installation and sealing of a dark box. A load number, the type of a load and a station number is provided upon initialisation of the software. The test sequence and all the required parameters are provided once, just before running the ECQA, in the dedicated panel reported in Figure 5.14. It is required to provide all the information mentioned in the previous points for the python-LabVIEW interface and the connection to the system controller together with the IPs and ports of RPI and HV crate. In the most right side, the actual ECQA tests are presented that are needed to be selected (green color) for the fully automated operation. The remaining parts of the control panel are reserved for the parameters of the tests. Subsequently, the main control panel is displayed, reported in Figure 5.15, where all the necessary information and notifications concerning the ECQA occur. The bottom-left window (highlighted in a green color) shows a tab where possible warning and error notifications are displayed during the procedure. This tab is also reserved for the QR code scanning part of MaPMTs (Figure 5.8) mentioned before. The "MAIN CONTROL" in the upper left corner, is responsible for managing the tests. The software is run in two modes. The "AUTO" mode runs the tests sequence, initialised at the very beginning, and is stopped only when a critical error occurs. The phases of the procedure and their current status are reported in the window to the right of "CONFIRM STEP" button. The "MANUAL" mode allows to select the desired test out of a sequence and permits the test to be repeated as many times as needed. To the right of the "MAIN CONTROL" panel, the "RPI" system demonstrates the current readings of environmental temperature and humidity recorded by the sensors placed inside a dark box. In the upper-right window, a panel is located that presents an overview of tests that have been executed so far. In the lower-right corner, the HV panel shows the status and the current values of the HV that is applied.

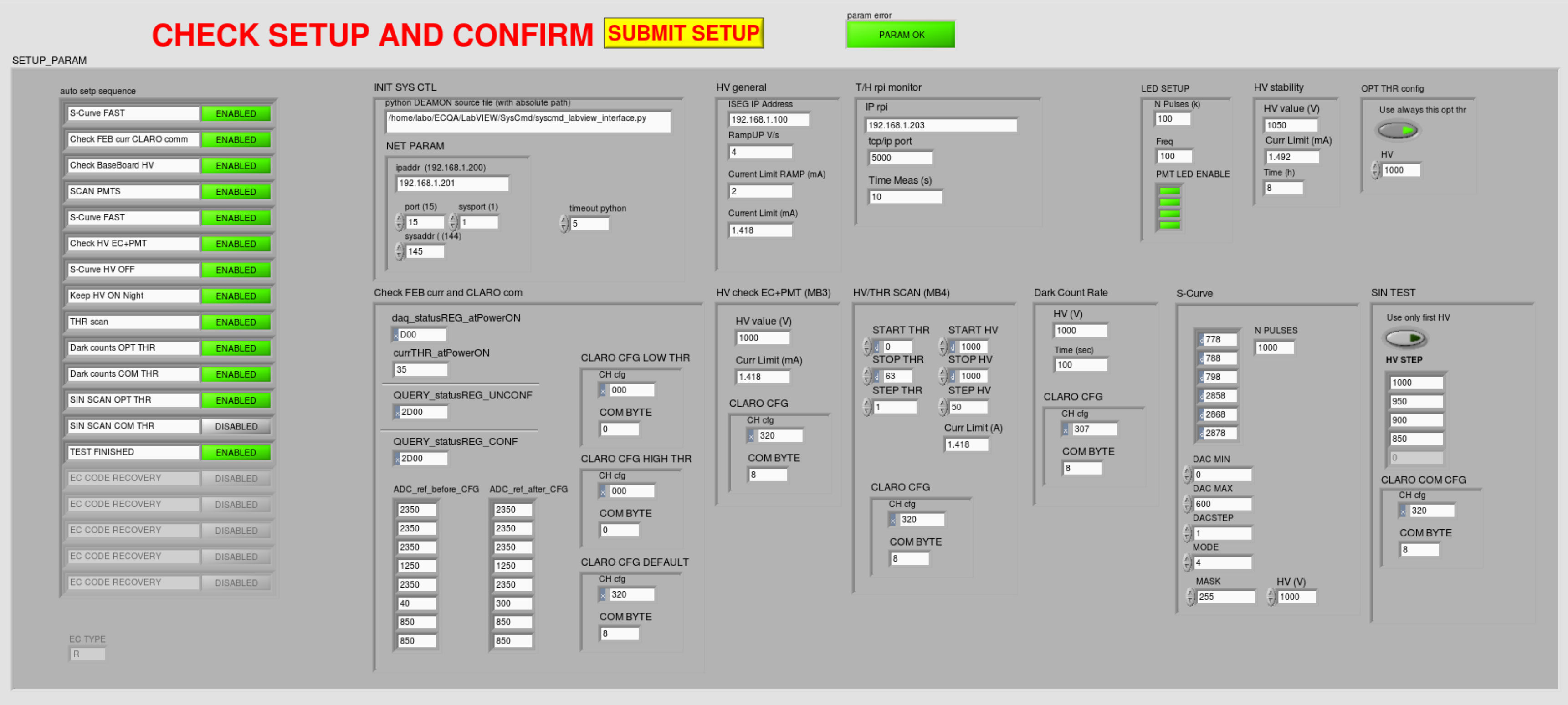

auto setp sequence
- S-Curve FAST: ENABLED
- Check FEB curr CLARO comm: ENABLED
- Check BaseBoard HV: ENABLED
- SCAN PMTS: ENABLED
- S-Curve FAST: ENABLED
- Check HV EC+PMT: ENABLED
- S-Curve HV OFF: ENABLED
- Keep HV ON Night: ENABLED
- THR scan: ENABLED
- Dark counts OPT THR: ENABLED
- Dark counts COM THR: ENABLED
- SIN SCAN OPT THR: ENABLED
- SIN SCAN COM THR: DISABLED
- TEST FINISHED: ENABLED
- EC CODE RECOVERY: DISABLED
- EC CODE RECOVERY: DISABLED
- EC CODE RECOVERY: DISABLED
- EC CODE RECOVERY: DISABLED
- EC CODE RECOVERY: DISABLED

EC TYPE: R

INIT SYS CTL
python DEAMON source file (with absolute path): /home/labo/ECQA/LabVIEW/SysCmd/syscmd_labview_interface.py
NET PARAM
ipaddr (192.168.1.200): 192.168.1.201
port (15): 15
sysport (1): 1
sysaddr ((144): 145
timeout python: 5

HV general
ISEG IP Address: 192.168.1.100
RampUP V/s: 4
Current Limit RAMP (mA): 2
Current Limit (mA): 1.418

T/H rpi monitor
IP rpi: 192.168.1.203
tcp/ip port: 5000
Time Meas (s): 10

LED SETUP
N Pulses (k): 100
Freq: 100
PMT LED ENABLE

HV stability
HV value (V): 1050
Curr Limit (mA): 1.492
Time (h): 8

OPT THR config
Use always this opt thr
HV: 1000

Check FEB curr and CLARO com
daq_statusREG_atPowerON: D00
currTHR_atPowerON: 35
QUERY_statusREG_UNCONF: 2D00
QUERY_statusREG_CONF: 2D00

ADC_ref_before_CFG	ADC_ref_after_CFG
2350	2350
2350	2350
2350	2350
1250	1250
2350	2350
40	300
850	850
850	850

CLARO CFG LOW THR
CH cfg: 000
COM BYTE: 0

CLARO CFG HIGH THR
CH cfg: 000
COM BYTE: 0

CLARO CFG DEFAULT
CH cfg: 320
COM BYTE: 8

HV check EC+PMT (MB3)
HV value (V): 1000
Curr Limit (mA): 1.418
CLARO CFG
CH cfg: 320
COM BYTE: 8

HV/THR SCAN (MB4)
START THR: 0
STOP THR: 63
STEP THR: 1
START HV: 1000
STOP HV: 1000
STEP HV: 50
Curr Limit (A): 1.418
CLARO CFG
CH cfg: 320
COM BYTE: 8

Dark Count Rate
HV (V): 1000
Time (sec): 100
CLARO CFG
CH cfg: 307
COM BYTE: 8

S-Curve
778
788
798
2858
2868
2878
N PULSES: 1000
DAC MIN: 0
DAC MAX: 600
DACSTEP: 1
MODE: 4
MASK: 255
HV (V): 1000

SIN TEST
Use only first HV
HV STEP
1000
950
900
850
0
CLARO COM CFG
CH cfg: 320
COM BYTE: 8

Figure 5.14: ECQA Software parameters panel. A detailed description provided in the text.

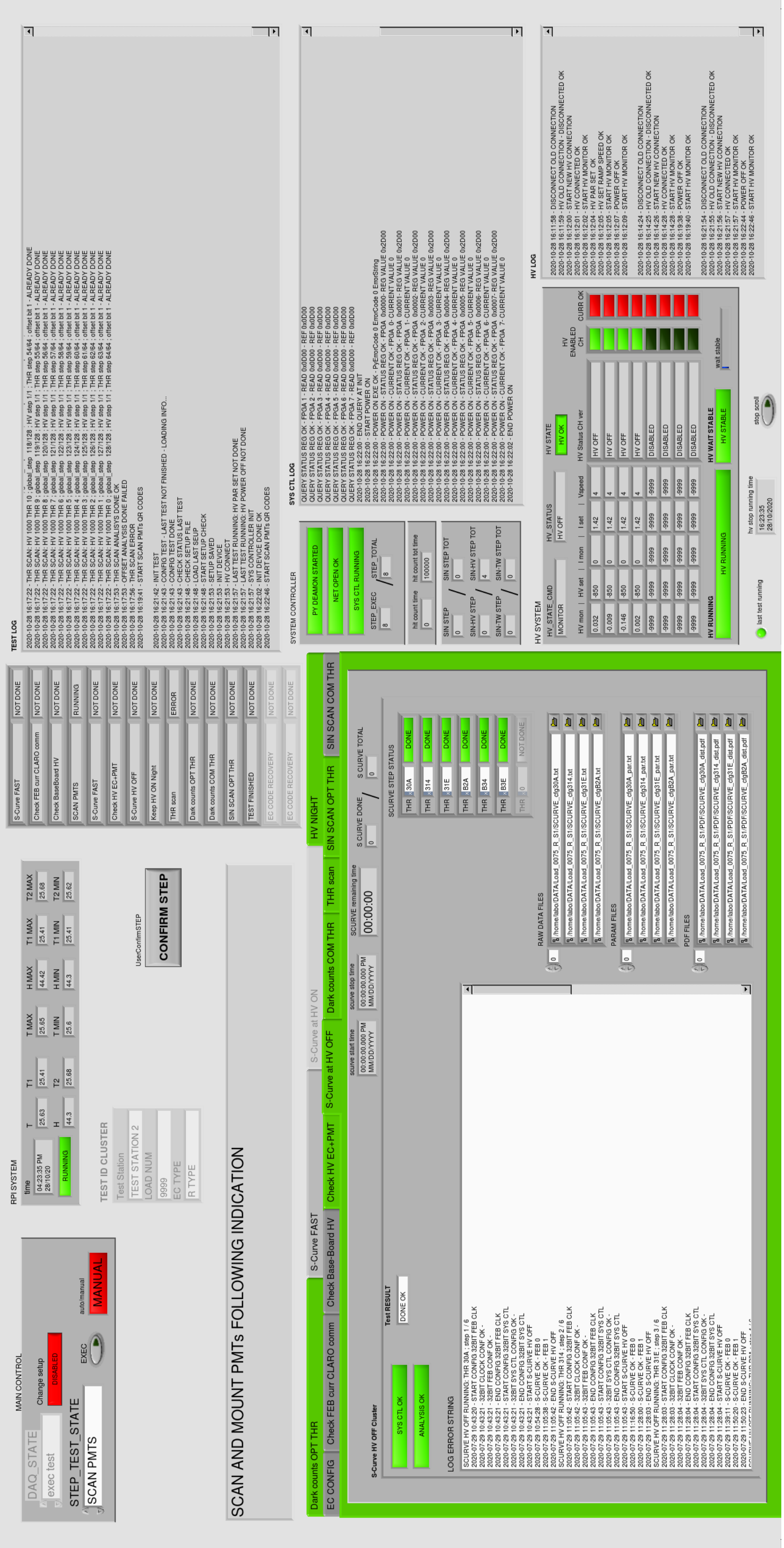

Figure 5.15: ECQA Software main panel. A detailed description provided in the text.

5.7 Data Analysis

In addition to the checks included in the ECQA test protocol, the data analysis is performed to provide an overview of obtained results. After each main measurement (i. e. DAC Scan, Threshold Scan, DCR and SIN), when the raw data is produced, the software initialises a dedicated script to perform an analysis. The scripts are written in C++ and python languages. The PDF files are produced containing the plots relevant to a specific measurement. As an association between the CLARO channels and the MaPMT anodes are not equivalent (the first CLARO channel does not correspond to the first MaPMT anode), each script consists of the electronic and optical mapping correlation. The part of the mapping files are presented in Figure 5.16.

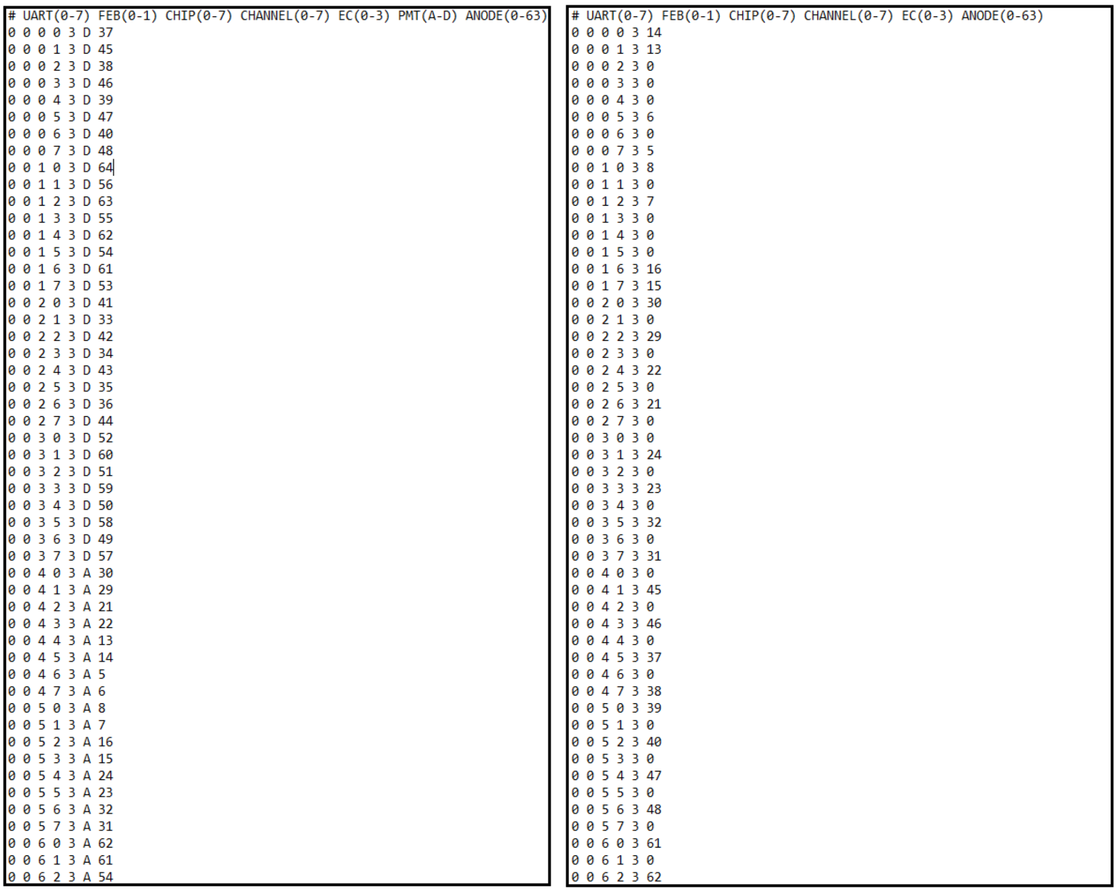

```
# UART(0-7) FEB(0-1) CHIP(0-7) CHANNEL(0-7) EC(0-3) PMT(A-D) ANODE(0-63)
0 0 0 0 3 D 37
0 0 0 1 3 D 45
0 0 0 2 3 D 38
0 0 0 3 3 D 46
0 0 0 4 3 D 39
0 0 0 5 3 D 47
0 0 0 6 3 D 40
0 0 0 7 3 D 48
0 0 1 0 3 D 64
0 0 1 1 3 D 56
0 0 1 2 3 D 63
0 0 1 3 3 D 55
0 0 1 4 3 D 62
0 0 1 5 3 D 54
0 0 1 6 3 D 61
0 0 1 7 3 D 53
0 0 2 0 3 D 41
0 0 2 1 3 D 33
0 0 2 2 3 D 42
0 0 2 3 3 D 34
0 0 2 4 3 D 43
0 0 2 5 3 D 35
0 0 2 6 3 D 36
0 0 2 7 3 D 44
0 0 3 0 3 D 52
0 0 3 1 3 D 60
0 0 3 2 3 D 51
0 0 3 3 3 D 59
0 0 3 4 3 D 50
0 0 3 5 3 D 58
0 0 3 6 3 D 49
0 0 3 7 3 D 57
0 0 4 0 3 A 30
0 0 4 1 3 A 29
0 0 4 2 3 A 21
0 0 4 3 3 A 22
0 0 4 4 3 A 13
0 0 4 5 3 A 14
0 0 4 6 3 A 5
0 0 4 7 3 A 6
0 0 5 0 3 A 8
0 0 5 1 3 A 7
0 0 5 2 3 A 16
0 0 5 3 3 A 15
0 0 5 4 3 A 24
0 0 5 5 3 A 23
0 0 5 6 3 A 32
0 0 5 7 3 A 31
0 0 6 0 3 A 62
0 0 6 1 3 A 61
0 0 6 2 3 A 54
```

```
# UART(0-7) FEB(0-1) CHIP(0-7) CHANNEL(0-7) EC(0-3) ANODE(0-63)
0 0 0 0 3 14
0 0 0 1 3 13
0 0 0 2 3 0
0 0 0 3 3 0
0 0 0 4 3 0
0 0 0 5 3 6
0 0 0 6 3 0
0 0 0 7 3 5
0 0 1 0 3 8
0 0 1 1 3 0
0 0 1 2 3 7
0 0 1 3 3 0
0 0 1 4 3 0
0 0 1 5 3 0
0 0 1 6 3 16
0 0 1 7 3 15
0 0 2 0 3 30
0 0 2 1 3 0
0 0 2 2 3 29
0 0 2 3 3 0
0 0 2 4 3 22
0 0 2 5 3 0
0 0 2 6 3 21
0 0 2 7 3 0
0 0 3 0 3 0
0 0 3 1 3 24
0 0 3 2 3 0
0 0 3 3 3 23
0 0 3 4 3 0
0 0 3 5 3 32
0 0 3 6 3 0
0 0 3 7 3 31
0 0 4 0 3 0
0 0 4 1 3 45
0 0 4 2 3 0
0 0 4 3 3 46
0 0 4 4 3 0
0 0 4 5 3 37
0 0 4 6 3 0
0 0 4 7 3 38
0 0 5 0 3 39
0 0 5 1 3 0
0 0 5 2 3 40
0 0 5 3 3 0
0 0 5 4 3 47
0 0 5 5 3 0
0 0 5 6 3 48
0 0 5 7 3 0
0 0 6 0 3 61
0 0 6 1 3 0
0 0 6 2 3 62
```

Figure 5.16: The mapping files used in the data analysis scripts. Left hand side shows a file dedicated for the R-type load while the right hand side presents the file for the H-type load.

The headline describes the columns underneath. For the R-type load, the first four numbers represent the electronic topology that is an ID of a CLARO channel which is the channel (0-7) of its chip (0-7) of its FEB (0-1) of its UART (0-7). Then two numbers follow that is the optical topology which is the anode (1-64) of its MaPMT (A-D). They are correlated with each other providing a tool for a 2D hitmaps generation. The difference between the R-type and H-type topology can be seen in Figure 5.17 and Figure 5.18 respectively.

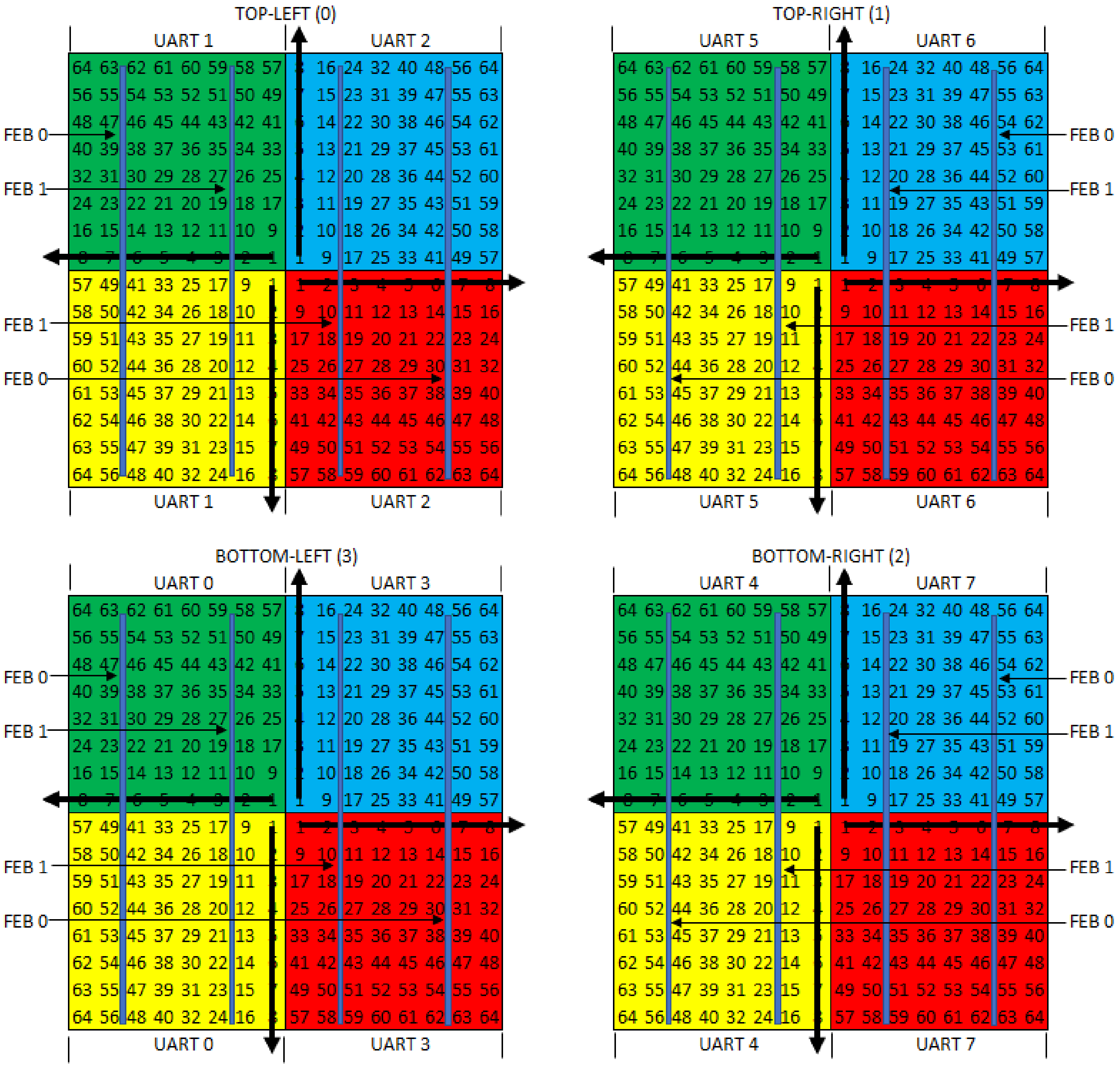

TOP-LEFT (0)

UART 1 | UART 2

64	63	62	61	60	59	58	57	8	16	24	32	40	48	56	64
56	55	54	53	52	51	50	49	7	15	23	31	39	47	55	63
48	47	46	45	44	43	42	41	6	14	22	30	38	46	54	62
40	39	38	37	36	35	34	33	5	13	21	29	37	45	53	61
32	31	30	29	28	27	26	25	4	12	20	28	36	44	52	60
24	23	22	21	20	19	18	17	3	11	19	27	35	43	51	59
16	15	14	13	12	11	10	9	2	10	18	26	34	42	50	58
8	7	6	5	4	3	2	1	1	9	17	25	33	41	49	57
57	49	41	33	25	17	9	1	1	2	3	4	5	6	7	8
58	50	42	34	26	18	10	2	9	10	11	12	13	14	15	16
59	51	43	35	27	19	11	3	17	18	19	20	21	22	23	24
60	52	44	36	28	20	12	4	25	26	27	28	29	30	31	32
61	53	45	37	29	21	13	5	33	34	35	36	37	38	39	40
62	54	46	38	30	22	14	6	41	42	43	44	45	46	47	48
63	55	47	39	31	23	15	7	49	50	51	52	53	54	55	56
64	56	48	40	32	24	16	8	57	58	59	60	61	62	63	64

UART 1 | UART 2

TOP-RIGHT (1)

UART 5 | UART 6

64	63	62	61	60	59	58	57	8	16	24	32	40	48	56	64
56	55	54	53	52	51	50	49	7	15	23	31	39	47	55	63
48	47	46	45	44	43	42	41	6	14	22	30	38	46	54	62
40	39	38	37	36	35	34	33	5	13	21	29	37	45	53	61
32	31	30	29	28	27	26	25	4	12	20	28	36	44	52	60
24	23	22	21	20	19	18	17	3	11	19	27	35	43	51	59
16	15	14	13	12	11	10	9	2	10	18	26	34	42	50	58
8	7	6	5	4	3	2	1	1	9	17	25	33	41	49	57
57	49	41	33	25	17	9	1	1	2	3	4	5	6	7	8
58	50	42	34	26	18	10	2	9	10	11	12	13	14	15	16
59	51	43	35	27	19	11	3	17	18	19	20	21	22	23	24
60	52	44	36	28	20	12	4	25	26	27	28	29	30	31	32
61	53	45	37	29	21	13	5	33	34	35	36	37	38	39	40
62	54	46	38	30	22	14	6	41	42	43	44	45	46	47	48
63	55	47	39	31	23	15	7	49	50	51	52	53	54	55	56
64	56	48	40	32	24	16	8	57	58	59	60	61	62	63	64

UART 5 | UART 6

BOTTOM-LEFT (3)

UART 0 | UART 3

64	63	62	61	60	59	58	57	8	16	24	32	40	48	56	64
56	55	54	53	52	51	50	49	7	15	23	31	39	47	55	63
48	47	46	45	44	43	42	41	6	14	22	30	38	46	54	62
40	39	38	37	36	35	34	33	5	13	21	29	37	45	53	61
32	31	30	29	28	27	26	25	4	12	20	28	36	44	52	60
24	23	22	21	20	19	18	17	3	11	19	27	35	43	51	59
16	15	14	13	12	11	10	9	2	10	18	26	34	42	50	58
8	7	6	5	4	3	2	1	1	9	17	25	33	41	49	57
57	49	41	33	25	17	9	1	1	2	3	4	5	6	7	8
58	50	42	34	26	18	10	2	9	10	11	12	13	14	15	16
59	51	43	35	27	19	11	3	17	18	19	20	21	22	23	24
60	52	44	36	28	20	12	4	25	26	27	28	29	30	31	32
61	53	45	37	29	21	13	5	33	34	35	36	37	38	39	40
62	54	46	38	30	22	14	6	41	42	43	44	45	46	47	48
63	55	47	39	31	23	15	7	49	50	51	52	53	54	55	56
64	56	48	40	32	24	16	8	57	58	59	60	61	62	63	64

UART 0 | UART 3

BOTTOM-RIGHT (2)

UART 4 | UART 7

64	63	62	61	60	59	58	57	8	16	24	32	40	48	56	64
56	55	54	53	52	51	50	49	7	15	23	31	39	47	55	63
48	47	46	45	44	43	42	41	6	14	22	30	38	46	54	62
40	39	38	37	36	35	34	33	5	13	21	29	37	45	53	61
32	31	30	29	28	27	26	25	4	12	20	28	36	44	52	60
24	23	22	21	20	19	18	17	3	11	19	27	35	43	51	59
16	15	14	13	12	11	10	9	2	10	18	26	34	42	50	58
8	7	6	5	4	3	2	1	1	9	17	25	33	41	49	57
57	49	41	33	25	17	9	1	1	2	3	4	5	6	7	8
58	50	42	34	26	18	10	2	9	10	11	12	13	14	15	16
59	51	43	35	27	19	11	3	17	18	19	20	21	22	23	24
60	52	44	36	28	20	12	4	25	26	27	28	29	30	31	32
61	53	45	37	29	21	13	5	33	34	35	36	37	38	39	40
62	54	46	38	30	22	14	6	41	42	43	44	45	46	47	48
63	55	47	39	31	23	15	7	49	50	51	52	53	54	55	56
64	56	48	40	32	24	16	8	57	58	59	60	61	62	63	64

UART 4 | UART 7

Figure 5.17: The MaPMT anodes numbering of the R-type load. The colors green, blue, red and yellow correspond to the MaPMT A, B, C and D respectively. The black arrows show the directions as they are rotated by 90° degrees clockwise to their successors.

For the H-type, the principles are the same, but in the optical topology only one number is necessary (as there is no need for the MaPMTs differentiation since there is only one MaPMT for each EC) that describes the anode numbering. Additionally, half of the UARTs (2, 3, 6, 7) are inactive as they are not physically connected to the FEBs. Inoperative UARTs are ignored by the scripts as the assigned anode number to these UARTs is always 0.

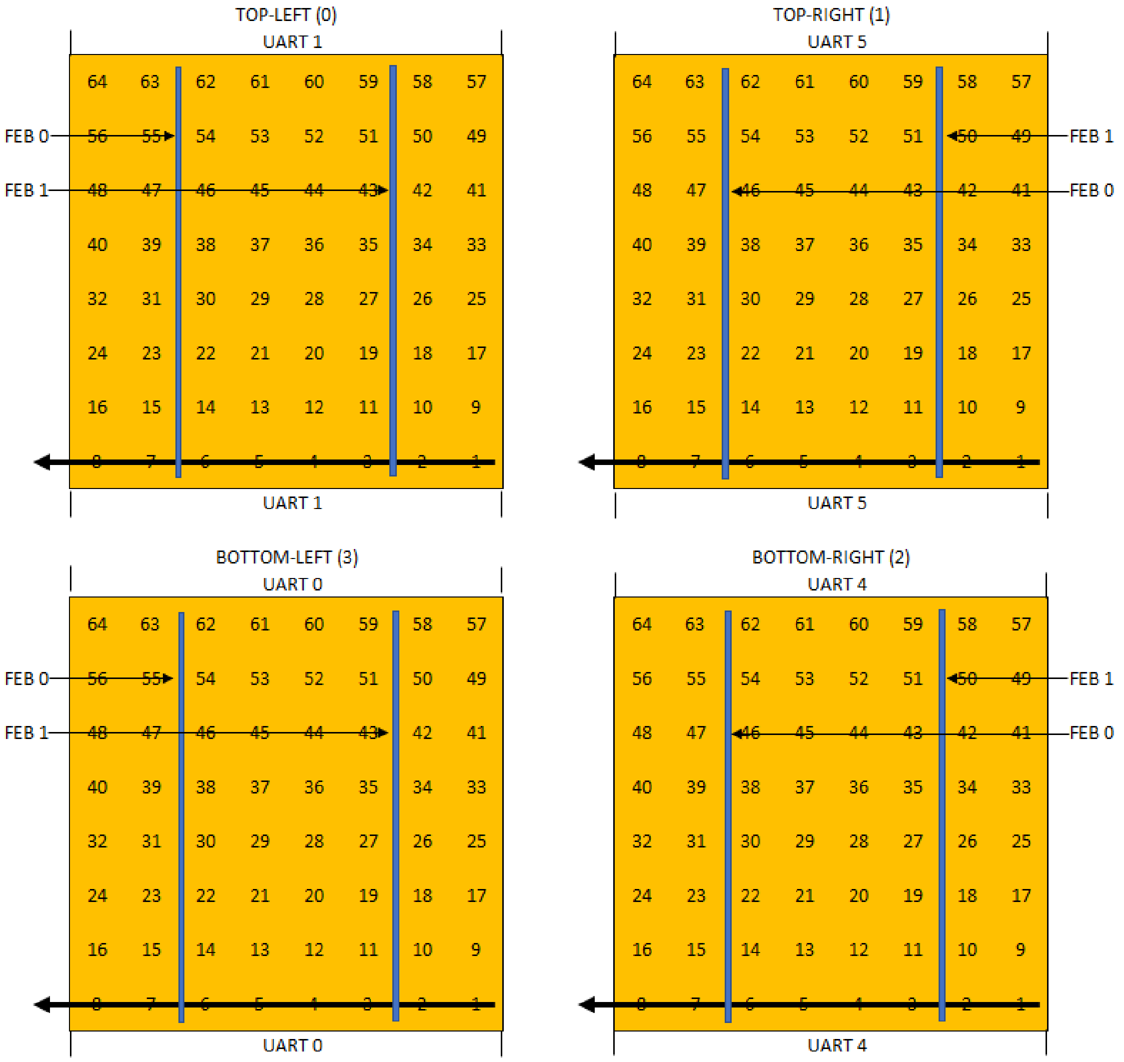

TOP-LEFT (0)

64	63	62	61	60	59	58	57
56	55	54	53	52	51	50	49
48	47	46	45	44	43	42	41
40	39	38	37	36	35	34	33
32	31	30	29	28	27	26	25
24	23	22	21	20	19	18	17
16	15	14	13	12	11	10	9
8	7	6	5	4	3	2	1

TOP-RIGHT (1)

64	63	62	61	60	59	58	57
56	55	54	53	52	51	50	49
48	47	46	45	44	43	42	41
40	39	38	37	36	35	34	33
32	31	30	29	28	27	26	25
24	23	22	21	20	19	18	17
16	15	14	13	12	11	10	9
8	7	6	5	4	3	2	1

BOTTOM-LEFT (3)

64	63	62	61	60	59	58	57
56	55	54	53	52	51	50	49
48	47	46	45	44	43	42	41
40	39	38	37	36	35	34	33
32	31	30	29	28	27	26	25
24	23	22	21	20	19	18	17
16	15	14	13	12	11	10	9
8	7	6	5	4	3	2	1

BOTTOM-RIGHT (2)

64	63	62	61	60	59	58	57
56	55	54	53	52	51	50	49
48	47	46	45	44	43	42	41
40	39	38	37	36	35	34	33
32	31	30	29	28	27	26	25
24	23	22	21	20	19	18	17
16	15	14	13	12	11	10	9
8	7	6	5	4	3	2	1

Figure 5.18: The MaPMT anodes numbering of the H-type load.

To evaluate the correctness of the electronic and optical mapping, a number of tests have been performed. Masks of various geometrical openings have been placed on top of MaPMT surfaces as shown in Figure 5.19 and Figure 5.20. The openings have been carved to check each individual pixel-anode correlation.

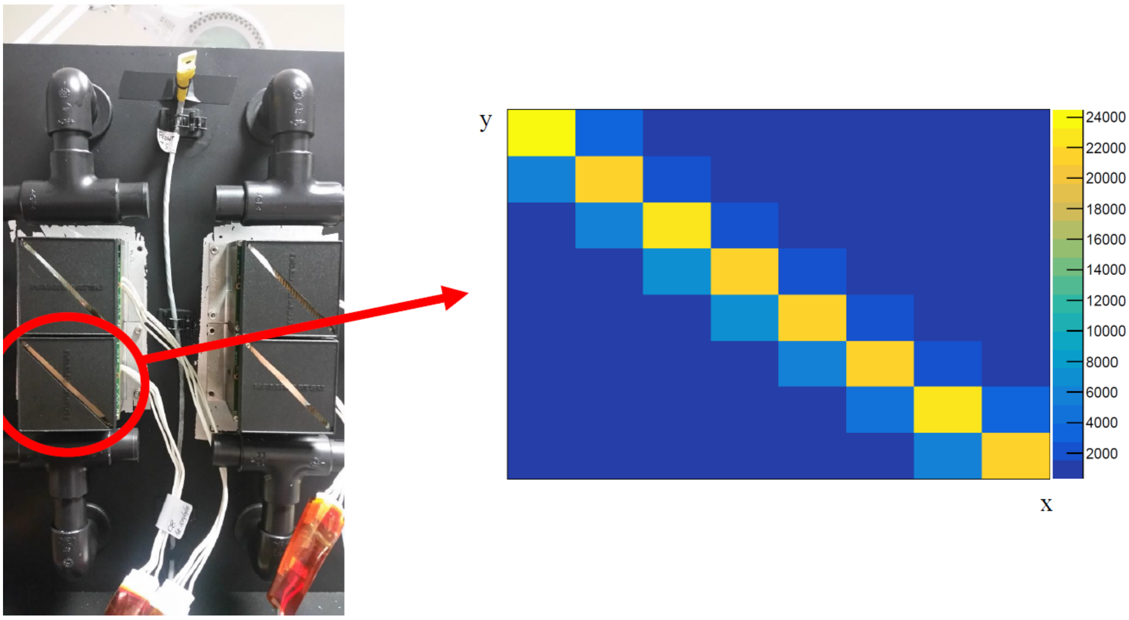

Figure 5.19: Masks with diagonal openings for the H-type load.

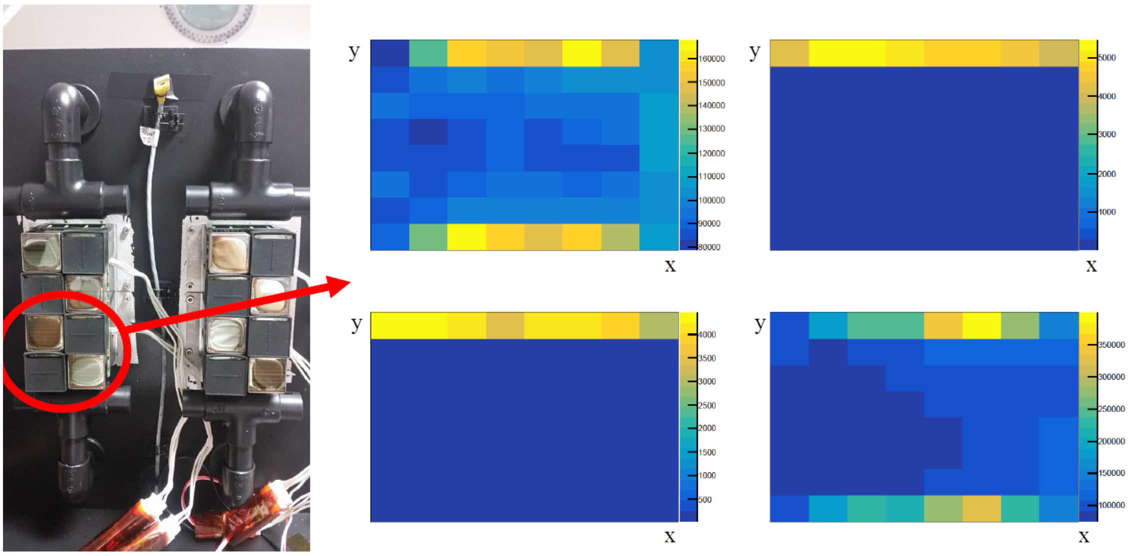

Figure 5.20: Masks with top openings for the R-type load.

5.7.1 DAC Scan

After the DAC Scan test is completed, a dedicated python script is run automatically to perform the analysis. For six output files with different discriminator thresholds, that are generated during the data acquisition, the equivalent number of text and PDF files are created. The translated ERF is used to fit an S-Curve that allows to obtain a transition point and a noise for each CLARO channel. The fit parameters for each CLARO channel are stored in text files required for the database. Additionally, the results are presented graphically in the PDF format. As an example, the S-Curve distribution of one of the channels is reported in Figure 5.21. The heading represents the ID of a CLARO channel which in this particular case (FPGA 0, FEB 0, chip 0, channel 0) is related to the 37th anode of MaPMT "D". The applied configuration is set to `0x30A` which corresponds to the discriminator threshold being equal to 10 units. The x_t (transition point) and the σ (noise) equal to 107.7 and 1.725 in DAC unit respectively.

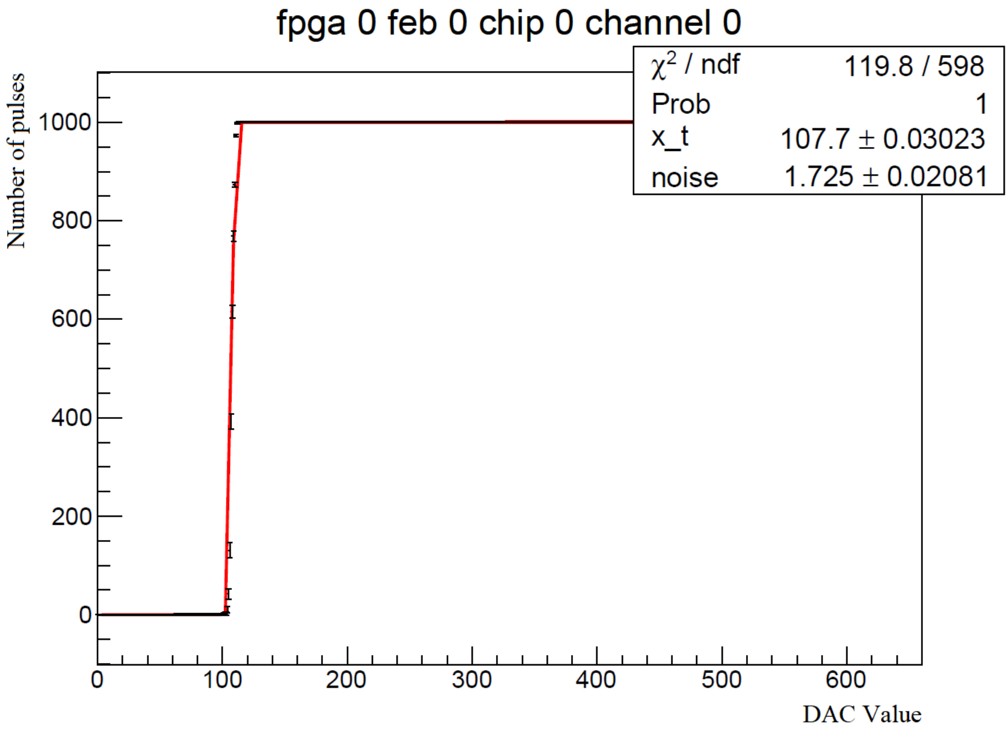

Figure 5.21: The S-Curve distribution for one of the CLARO channels. The parameters of interests are shown in the top-right corner.

The S-Curve fits are performed for all the other remaining CLARO channels. The summary is then presented in the form of histograms. The latter, reported in Figure 5.22, represent the transition point and noise distributions for all the CLARO channels present in a particular load. The distributions are the Gaussian distributions. The entries correspond to the number of channels that have transitions. The expected number of transitions for each measurement is 1024 and 256 respectively for the R-Type and the H-Type load if fully mounted. In the presented example (also at the discriminator threshold equal to 10), the entries are equal to 1024 hence in all the CLARO channel the transition took place because the discussed load is the R-type load. The average value of transition points and noises are equal to 125.3 and 1.753 (in DAC unit) accordingly for this particular example.

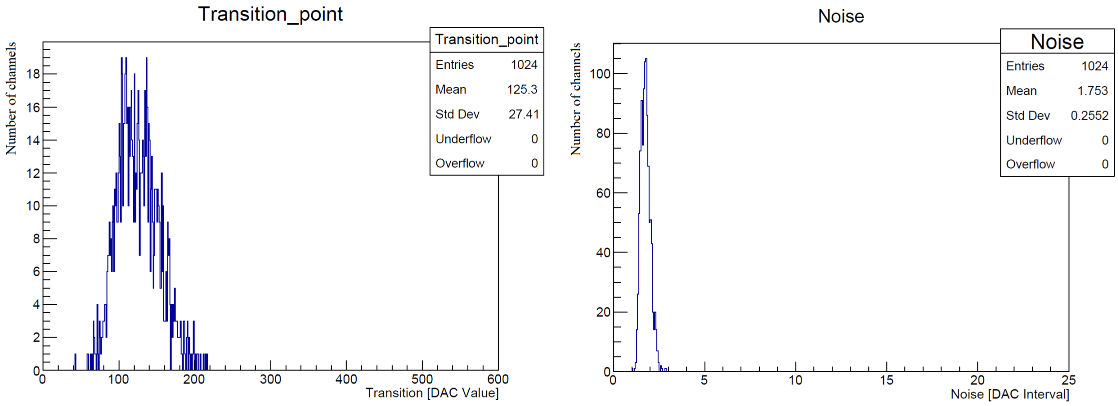

Figure 5.22: The histograms of transition points and noises for the R-type load containing 4 ECs. The entries represent the number of channels that had transitions.

All the parameters of interest that are: the transition point, the noise, the error of transition point, the error of noise and their corresponding ID of CLARO channels are stored in text files to be extracted for the CERN's database. Additionally, for each discriminator threshold, the log files are generated containing overviews of a measured load. The overview includes the number of channels that have transitions and in case of dead or noisy channels, the corresponding ID of a CLARO channel is featured.

5.7.2 Threshold Scan

A subsequent analysis performed during the ECQA procedure is the Threshold Scan analysis that is crucial for the MaPMTs calibration. In order to find a working point for each CLARO channel, the first edge after the pedestal has to be navigated. To ensure that no noise is included, additional five threshold steps are added. At first, the analysis is performed for the offset bit 0. Majority of the CLARO channels do not posses the pedestal at that offset bit hence no working points can be determined. Figure 5.23 represents the overview of the channels for the offset bit 0 for the full R-type load.

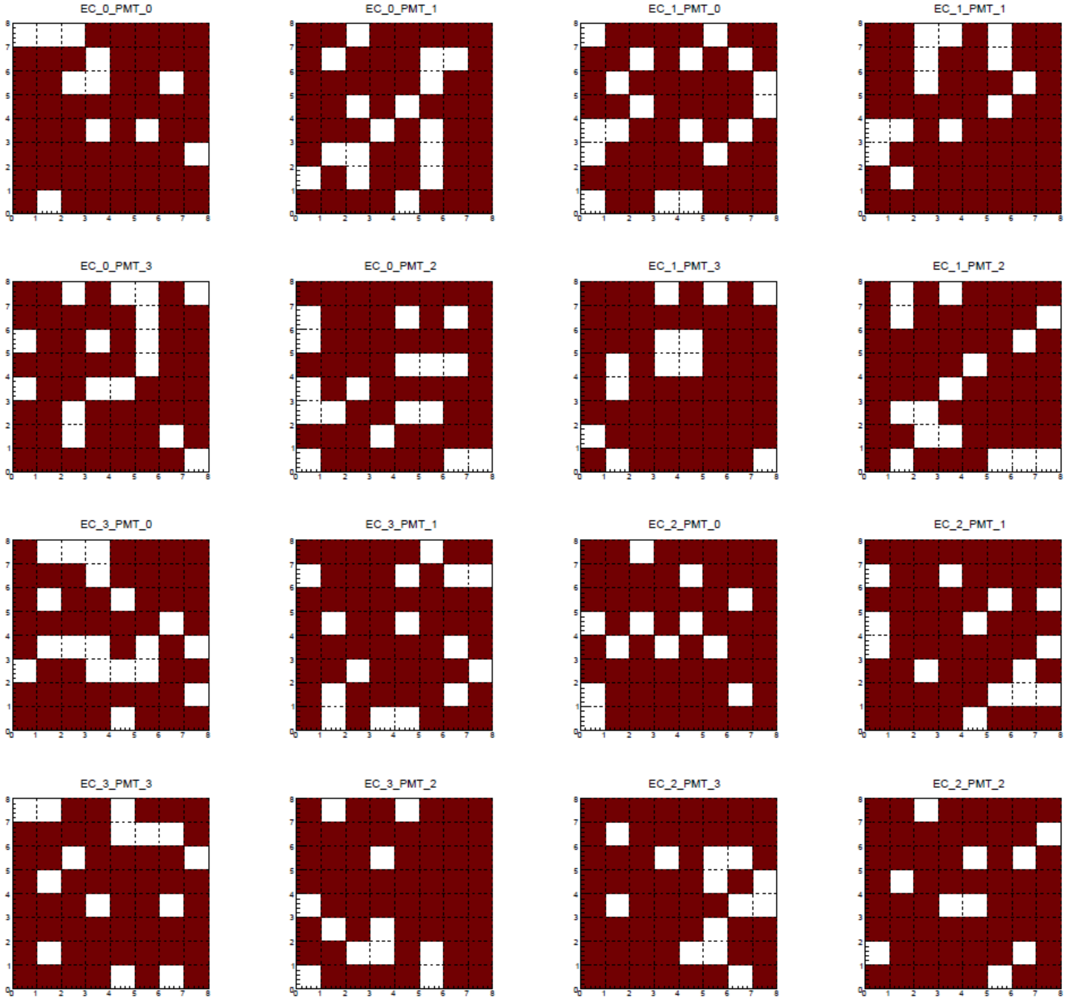

Figure 5.23: The overview representing the CLARO channels for which the working points cannot be determined (red-brown color) as the pedestals are not found.

The overview is a 2D histogram of 4x4 MaPMTs of 8x8 anodes for the R-type load (2x2 MaPMTs of 8x8 anodes for the H-type load). The left blank spots represent the CLARO channels that are able to be configured. The highlighted red-brown color indicates the CLARO channels for which the working points are not found. Presumably, the region of thresholds does not cover the noise pedestal. The situation changes with the second iteration performed for the offset bit 1 where, due to the -32 thresholds shift, the pedestals are found for all the CLARO channels. The obtained optimised thresholds and corresponding configurations are then established.

In addition to the load overviews for the offset bit 0 and 1, for each individual MaPMT, the hit-map of working points and the Threshold Scan distributions for all the 64 CLARO channels are created (Figure 5.24). For the hit-map, the lower number corresponds to the MaPMT anode number whereas the upper number to the actual established value of the working point. For each anode, the Threshold Scan distribution can be carefully examined. The entries correspond to the number of thresholds that change from 63 to 0. The working points, their decimal representations and corresponding ID of the CLARO channels are saved in two separate text files for the offset bit 0 and 1.

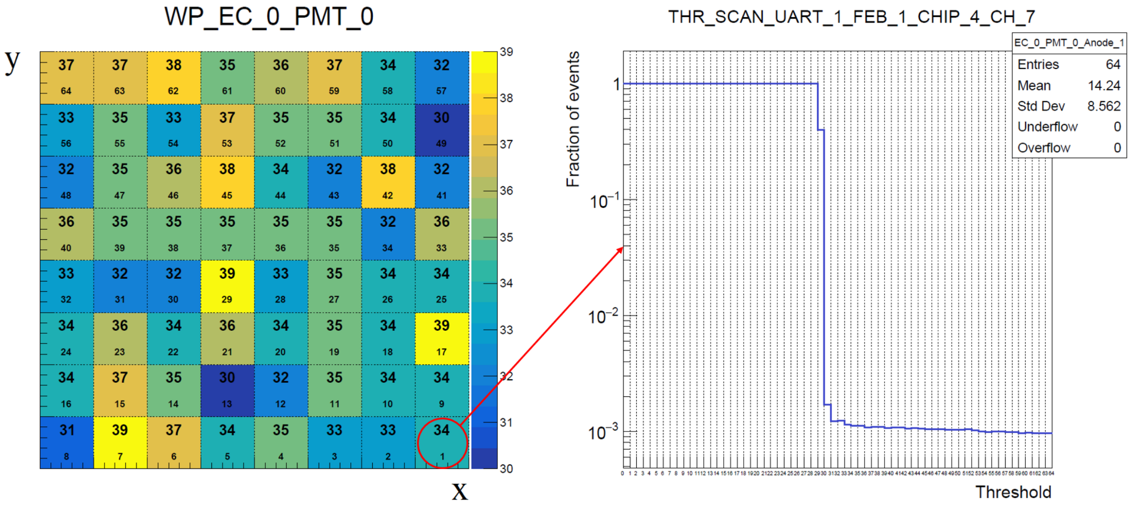

37 64	37 63	38 62	35 61	36 60	37 59	34 58	32 57
33 56	35 55	33 54	37 53	35 52	35 51	34 50	30 49
32 48	35 47	36 46	38 45	34 44	32 43	38 42	32 41
36 40	35 39	35 38	35 37	35 36	35 35	32 34	36 33
33 32	32 31	32 30	39 29	33 28	35 27	34 26	34 25
34 24	36 23	34 22	36 21	34 20	35 19	34 18	39 17
34 16	37 15	35 14	30 13	32 12	35 11	34 10	34 9
31 8	39 7	37 6	34 5	35 4	33 3	33 2	34 1

Figure 5.24: The 2D histogram (left side) representing the obtained working points for the MaPMT "A" of R-Type EC at the offset bit 1. On the right side, the threshold scan distribution is presented for Anode 1.

5.7.3 Dark Count Rate

The dark counts, that are the signals not generated due to the source of light, are the subject for the consecutive analysis. For each MaPMT anode, the DCR rate is calculated using the formula from Equation 3.9. Similarly to the Threshold Scan analysis, the overview of the analysed load is presented (Figure 5.25). If the MaPMT anode exhibits higher dark counts than admissible (1 kHz), it is highlighted on a yellow color. Depending on the type of the load, the overview can either be 4x4 (R-Type) or 2x2 (H-Type).

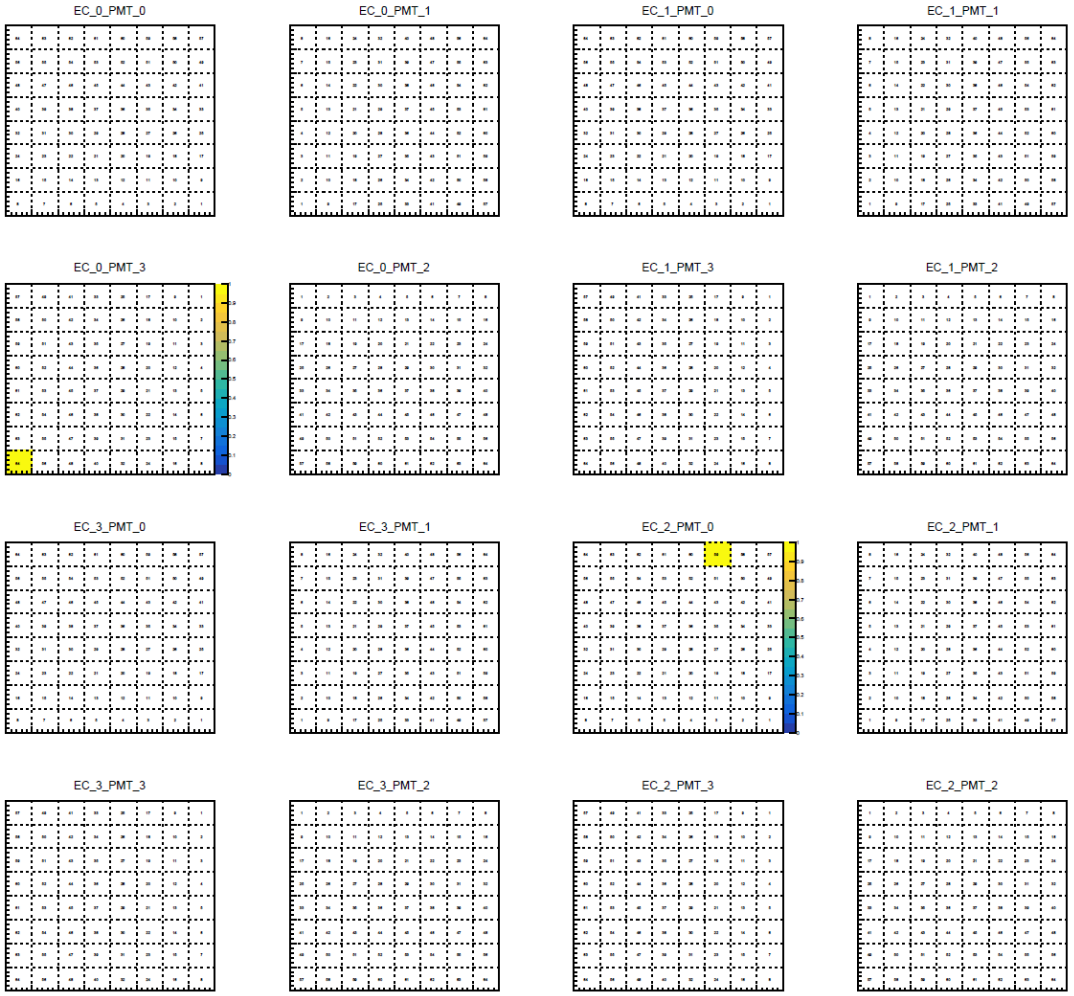

Figure 5.25: The overview of DCR for the load containing 4 ECs. The following distinction allows to determine MaPMT anodes exceeding 1 kHz (yellow color).

There are in total two overviews as there are two iterations of the data acquisition during the DCR measurement. The first one is performed for the fixed configuration `0x307` (threshold 7), whereas the second one is done for the optimised thresholds which are established during the Threshold Scan analysis for the offset bit 1.

Subsequently, the 2D histograms are produced to demonstrate the uniformity of the DCR. In contrary to the Threshold Scan analysis, where each individual MaPMT is analysed and presented separately, in the DCR analysis a set of MaPMTs (R-Type) for a particular EC is examined (Figure 5.26). The DCRs and the corresponding IDs of CLARO channels are stored in two separate files to be used for the database.

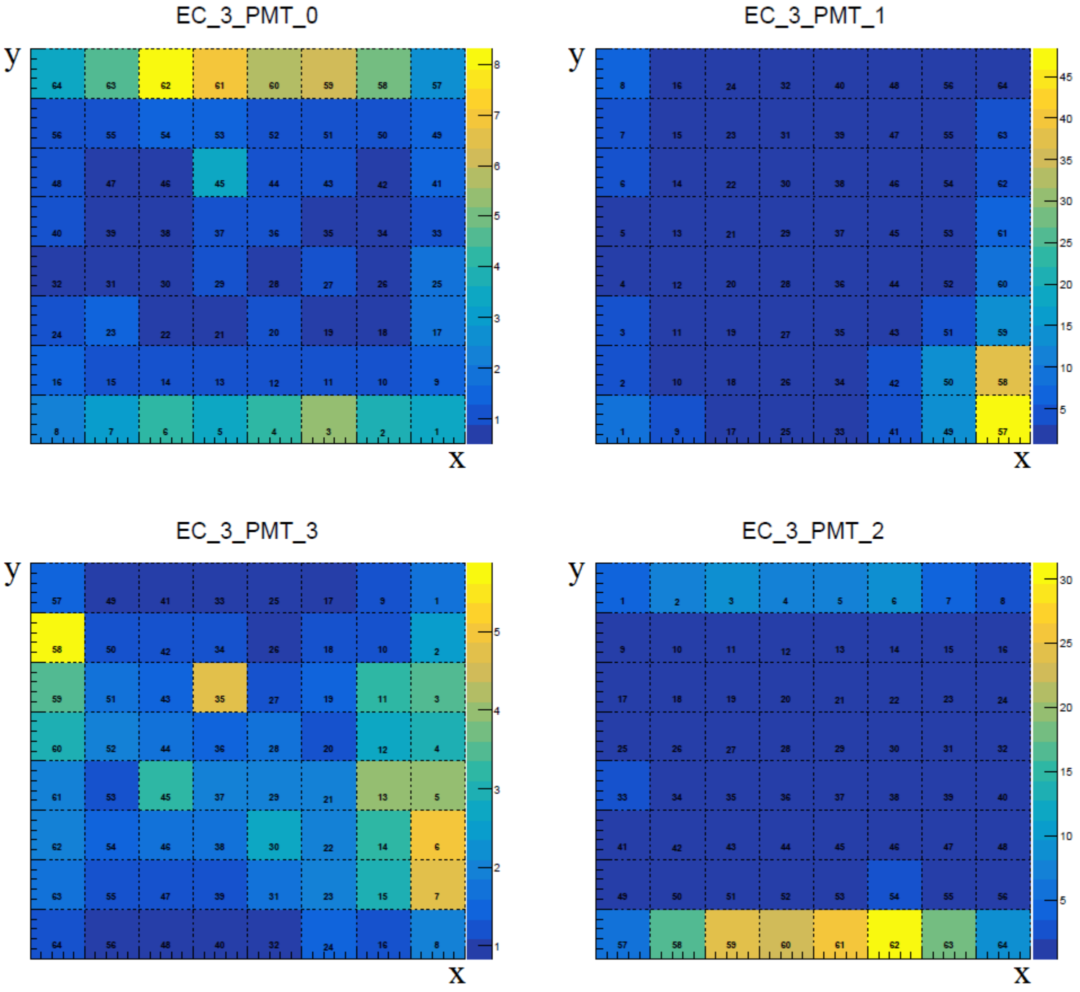

Figure 5.26: The DCR histogram of R-Type EC performed for optimized thresholds.

5.7.4 Signal Induced Noise

The last analysis that is performed is the SIN analysis. Depending on the magnitude of the after-pulses, three distinctive regions can be isolated (Figure 5.27). During the ECQA procedure it has been noticed, that all the MaPMTs follow the presented pattern.

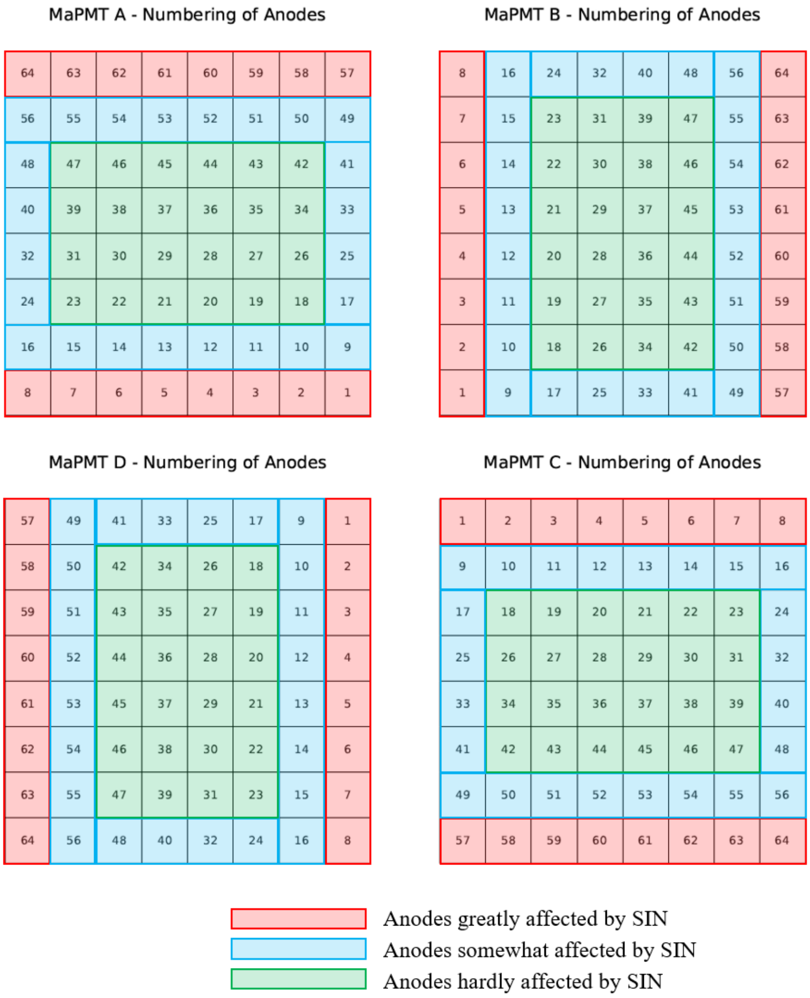

MaPMT A - Numbering of Anodes

64	63	62	61	60	59	58	57
56	55	54	53	52	51	50	49
48	47	46	45	44	43	42	41
40	39	38	37	36	35	34	33
32	31	30	29	28	27	26	25
24	23	22	21	20	19	18	17
16	15	14	13	12	11	10	9
8	7	6	5	4	3	2	1

MaPMT B - Numbering of Anodes

8	16	24	32	40	48	56	64
7	15	23	31	39	47	55	63
6	14	22	30	38	46	54	62
5	13	21	29	37	45	53	61
4	12	20	28	36	44	52	60
3	11	19	27	35	43	51	59
2	10	18	26	34	42	50	58
1	9	17	25	33	41	49	57

MaPMT D - Numbering of Anodes

57	49	41	33	25	17	9	1
58	50	42	34	26	18	10	2
59	51	43	35	27	19	11	3
60	52	44	36	28	20	12	4
61	53	45	37	29	21	13	5
62	54	46	38	30	22	14	6
63	55	47	39	31	23	15	7
64	56	48	40	32	24	16	8

MaPMT C - Numbering of Anodes

1	2	3	4	5	6	7	8
9	10	11	12	13	14	15	16
17	18	19	20	21	22	23	24
25	26	27	28	29	30	31	32
33	34	35	36	37	38	39	40
41	42	43	44	45	46	47	48
49	50	51	52	53	54	55	56
57	58	59	60	61	62	63	64

🟥 Anodes greatly affected by SIN
🟦 Anodes somewhat affected by SIN
🟩 Anodes hardly affected by SIN

Figure 5.27: Zones depending on the magnitude of SIN.

Anodes mostly influenced by SIN are the anodes 1-8 and 57-64. They are referred as "anodes greatly affected by SIN" marked on red color. On the other hand the "anodes hardly affected by SIN" represent a group of anodes in a central region that are affected the least by SIN. They are stressed by green color. Between these two regions, the last group is composed of "anodes somewhat affected by SIN" that are classified between these two groups in terms of SIN magnitude.

The actual SIN distribution can be seen in Figure 3.19. The time interval is represented in step units, dependent on a DAC value, where each step constitutes to 25 ns. The total SIN spectrum is taken from 0 to 256 steps (0 to 6.4 μs). Multiple SIN measurements were performed and it was observed that the peak (marked on green color) occurs at the step 14 (325-350) ns followed by the smaller peak at the step 15 (350-375) ns. However, for small portion of anodes, the situation is reversed as the main peak is recorded at the step 15. For this reason, the signal is considered to be the sum of these two intervals. Every counts proceeding the LED signal, recorded at the steps 0-13 (0-325) ns, are the dark counts. Most of the time, the intrinsic noise equals to zero, but if present, it constitutes just to few counts maximum hence the mentioned range and corresponding counts are not considered in the SIN analysis. Everything that follows after the LED signal (marked on red color), registered at the steps 15-256 (0.375-6.4) μs, is the actual SIN. When the SIN test is completed and the raw data files are produced for each HV (e. i. 1000 V, 950 V, 900 V and 850 V), the SIN analysis script is initialised. The script distinguishes the dark counts, the LED signal and the SIN. Based on the obtained values, the histograms of the LED signal and the total counts (signal and SIN) are produced (Figure 5.28). The values in each anode represent the anodes numbering. The followed graphs give an overview of the absolute values hence the magnitude of SIN needs to be determined.

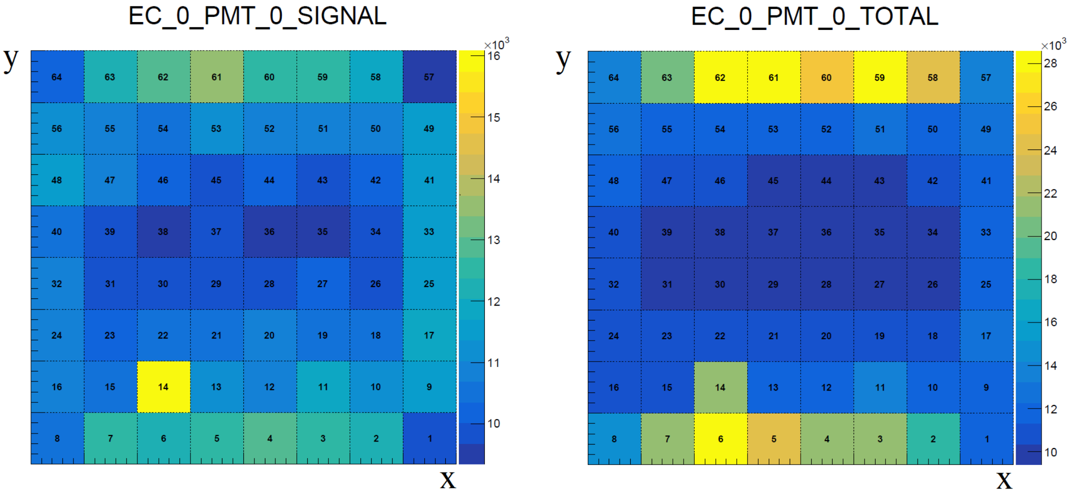

Figure 5.28: 2D histograms presenting the signal and the total counts acquired during the SIN measurement for the MaPMT A of Type-R EC at 1000 V.

The constitution of SIN is the inherent element of every MaPMT. However, modifications of MaPMTs structures were introduced by the developer (Hamamatsu Company) to minimize as much as possible the SIN presence in their products. For this reason, 200 new R-type MaPMTs were produced and delivered to Ferrara facility. They are referred as the "SIN-less" MaPMTs. The presence of SIN is still noticeable but on much lower scale in comparison to all the other MaPMTs. The SIN-less ECs are going to be placed in the regions at the highest occupancy. Figure 5.29 presents the SIN hit-map and exemplary SIN spectra for three regions of interest. The value in each anode corresponds to the constitution of SIN Fraction in percentage, calculated using the formula from Equation 3.10.

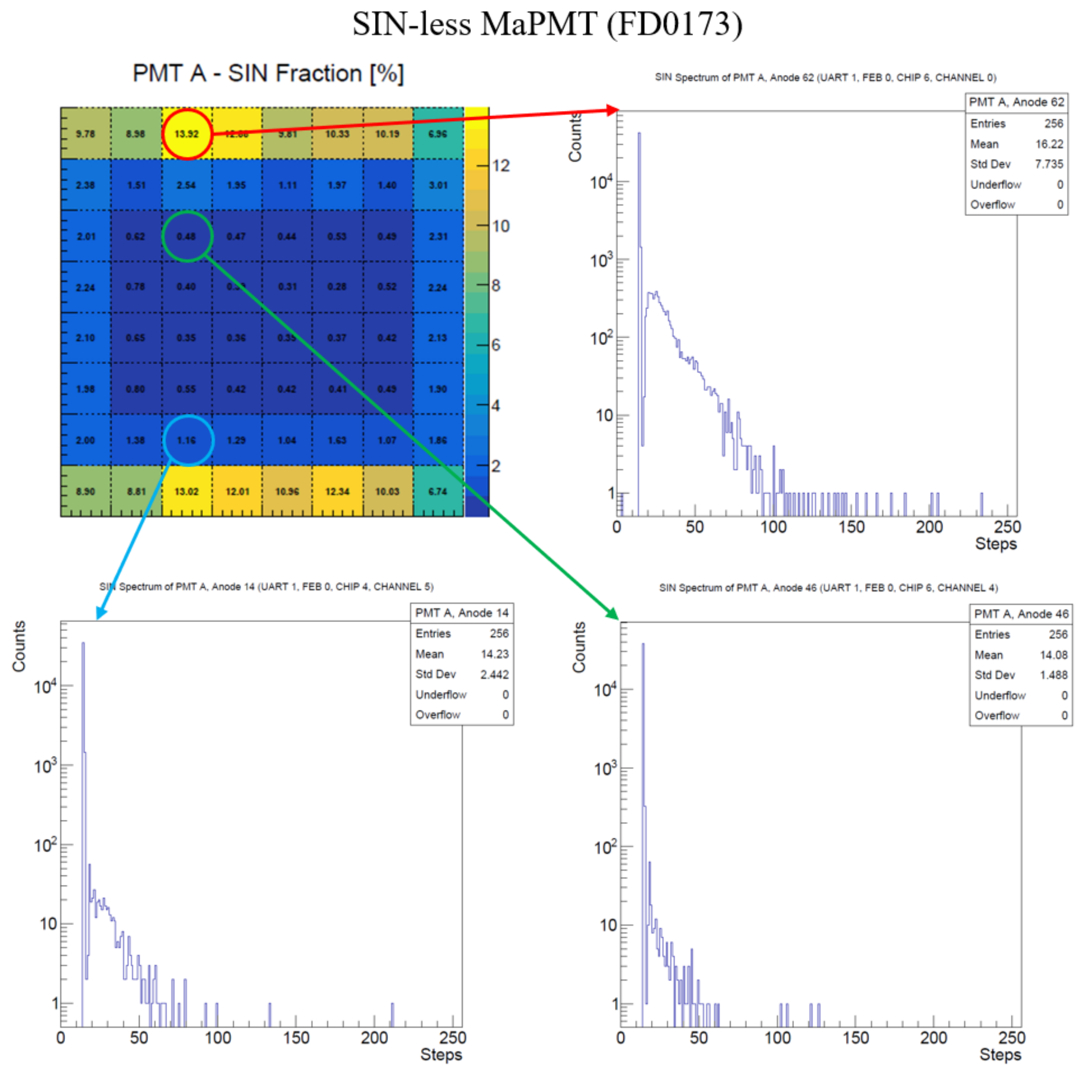

Figure 5.29: SIN hit-map and three SIN spectra of one of the SIN-less MaPMT.

Every MaPMT not being in the newly produced family of 200 SIN-less MaPMTs, is referred as the "SIN-affected" MaPMT. For the comparison, Figure 5.30 is presented with the same graphs as in the example above but for the SIN-affected EC. The SIN constitution is much greater for all the anodes.

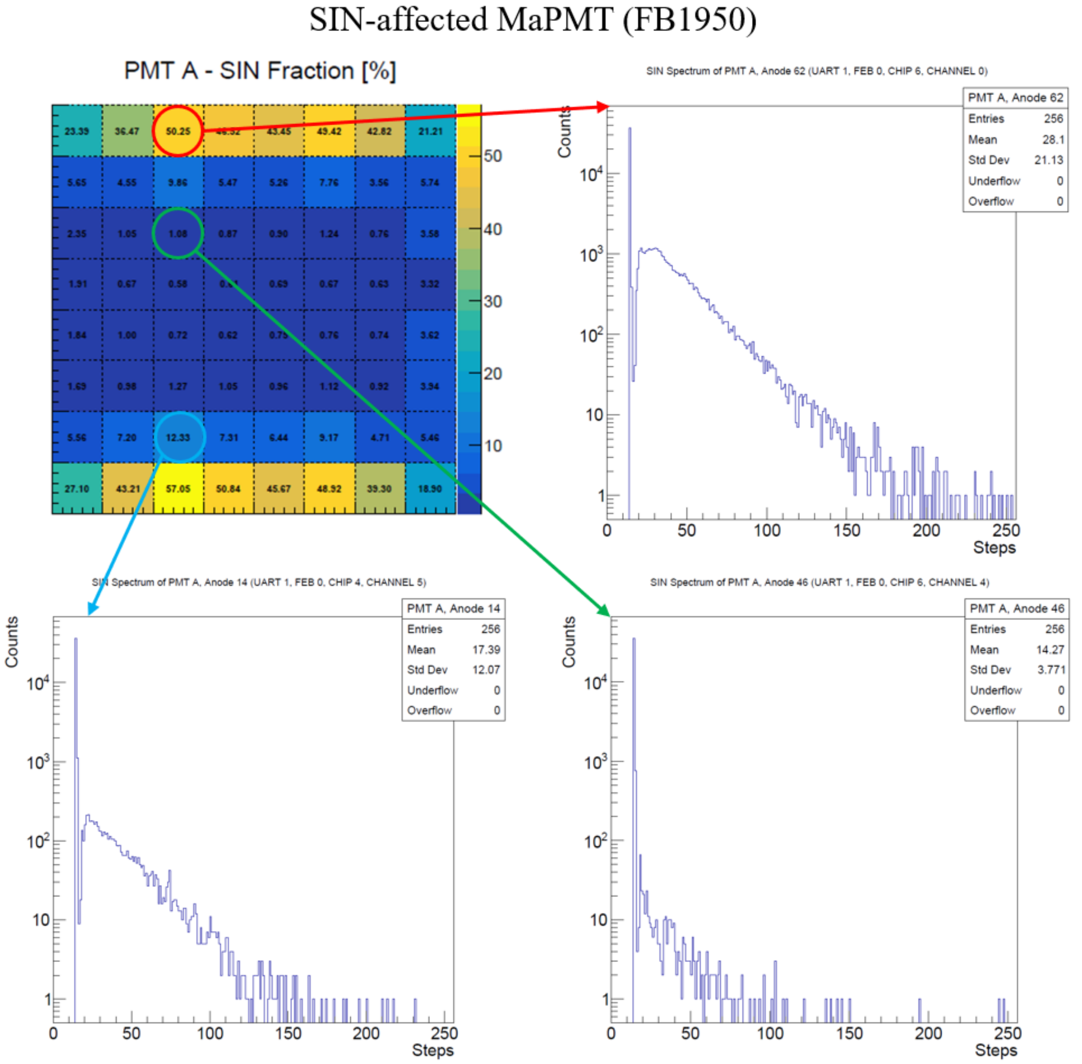

Figure 5.30: SIN hit-map and three SIN spectra of one of the SIN-affected MaPMT.

Subsequently, the S/N Ratio is determined using the formula from Equation 3.11. The histogram of exemplary EC of Type-R is presented in Figure 5.31. Similarly to the previous histogram, the values represent the actual result of S/N Ratio for each anode. As one could expect, the highest S/N concentration falls into the region of the anodes hardly affected by SIN, followed by the anodes somewhat affected by SIN and the anodes greatly affected by SIN.

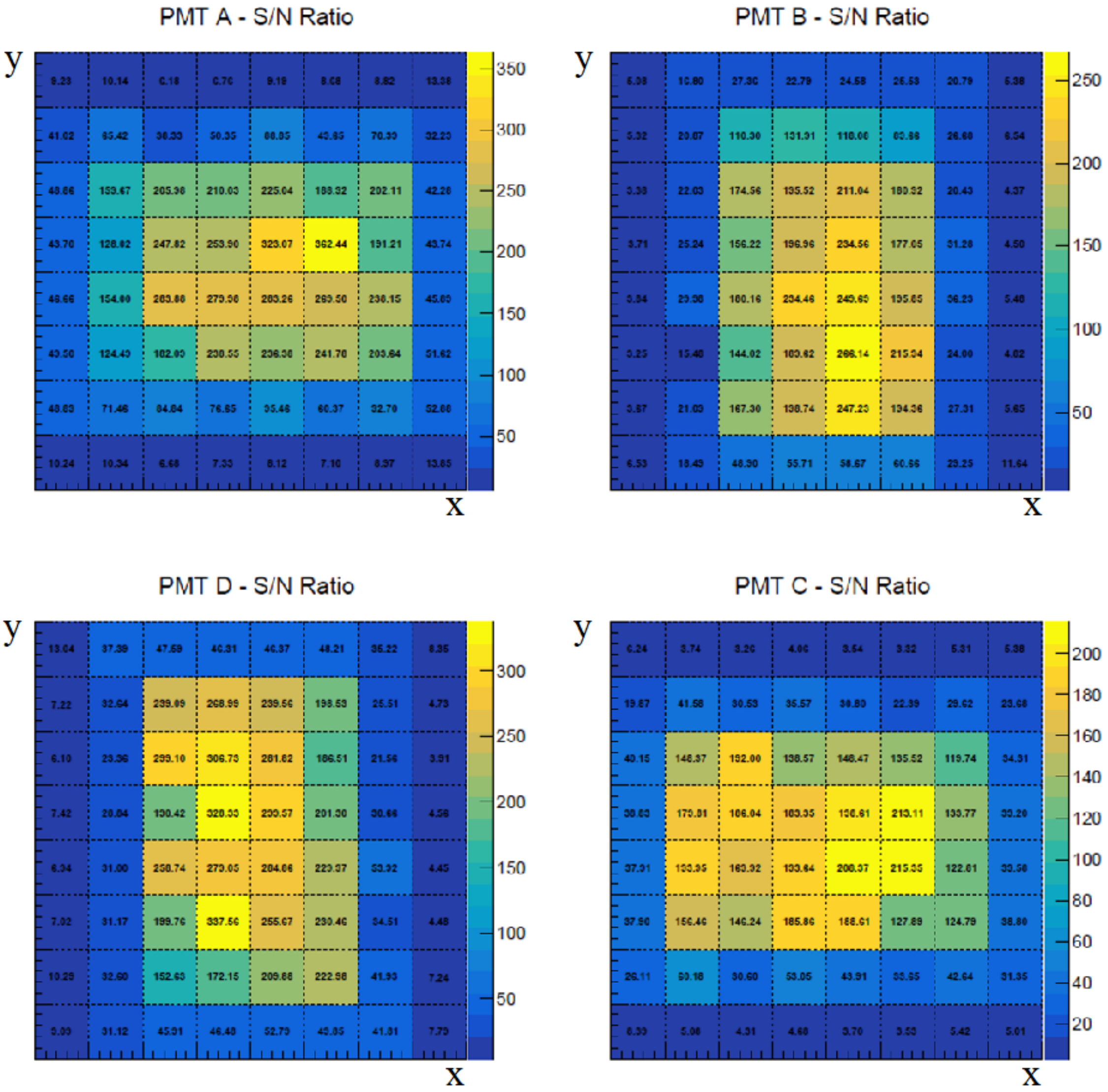

Figure 5.31: 2D histogram of S/N Ratio for SIN-less R-Type EC.

In addition, the histograms are produced to give an overview of SIN Fraction and S/N Ratio for all the anodes of a particular EC. The comparison between the SIN-less EC and the SIN-affected EC is presented in Figure 5.32 and Figure 5.33 for these two parameters. For the SIN-less EC, SIN Fraction constitutes mainly just few percentage for most of the anodes. For few anodes, in the region of anodes greatly affected by SIN, SIN goes up to 24%. In confrontation with the SIN-affected EC, SIN is much greater and goes up to around 80%. When it comes to the S/N Ratio, as expected, for the SIN-less EC the S/N Ratio is significantly greater reaching up to 350 while for the SIN-affected EC it is around 200.

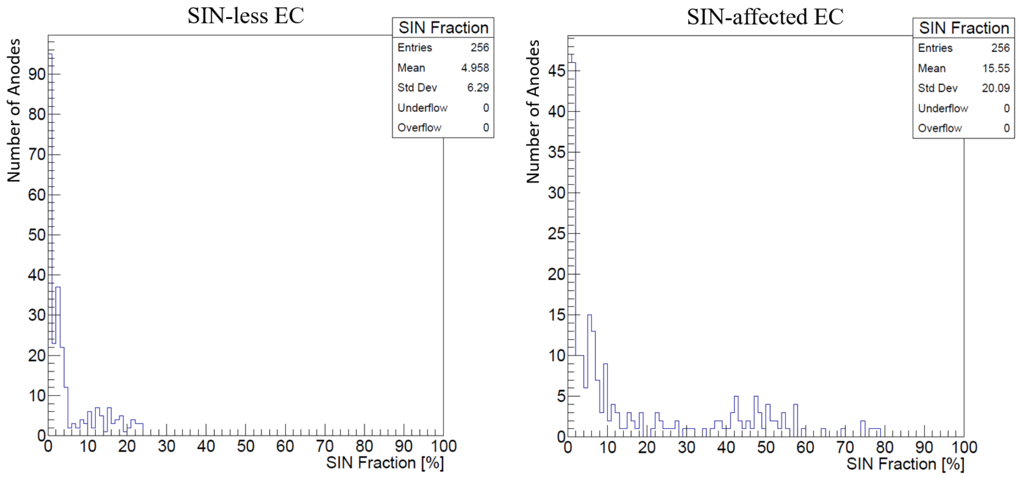

Figure 5.32: Comparison between SIN-less EC and SIN-affected EC in SIN Fraction.

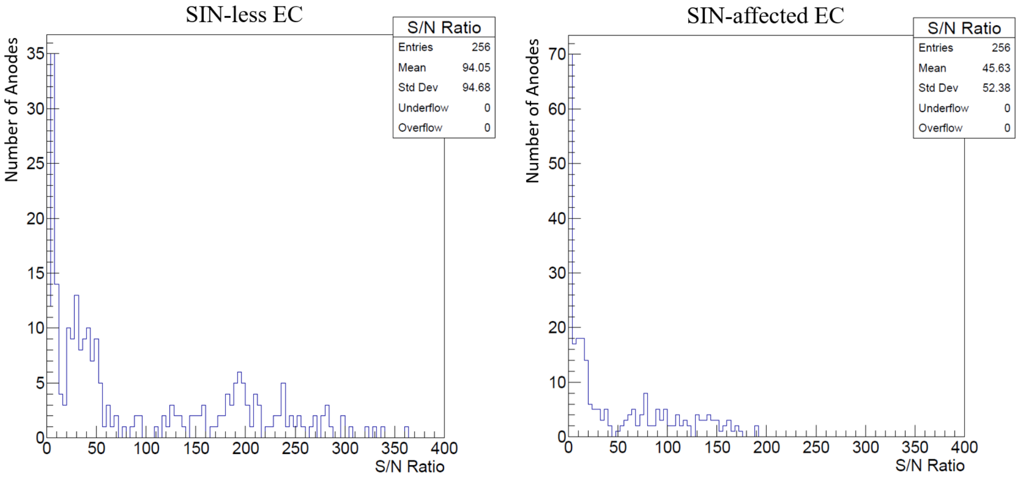

Figure 5.33: Comparison between SIN-less EC and SIN-affected EC in S/N Ratio.

A detailed overview concerning the SIN Fraction and S/N Ratio between the SIN-less and the SIN-affected ECs was performed. For this reason, high statistic of CLARO channels (6144) was analysed as 24 ECs (12 SIN-less and 12 SIN-affected) were selected and tested. The results are summarised in Table 5.1 (for the anodes hardly affected by SIN), Table 5.2 (for the anodes somewhat affected by SIN), Table 5.3 (for the anodes greatly affected by SIN) and Table 5.4 (for all the anodes affected by SIN). The analysis has proven that the SIN-less ECs perform much better (lower SIN Fraction and higher S/N Ratio) in comparison to the SIN-affected ECs. As intended, the SIN-less ECs should be installed in the regions at the highest occupancy.

Average SIN Fraction of SIN-less ECs in comparison to SIN-affected ECs is:

- 52% lower for the anodes hardly affected by SIN,
- 64% lower for the anodes somewhat affected by SIN,
- 63% lower for the anodes greatly affected by SIN,
- 63% lower for all the anodes affected by SIN.

Average S/N Ratio of SIN-less ECs in comparison to SIN-affected ECs is:

- 2.00 times higher for the anodes hardly affected by SIN,
- 2.25 times higher for the anodes somewhat affected by SIN,
- 3.95 higher for the anodes greatly affected by SIN,
- 2.05 lower for all the anodes affected by SIN.

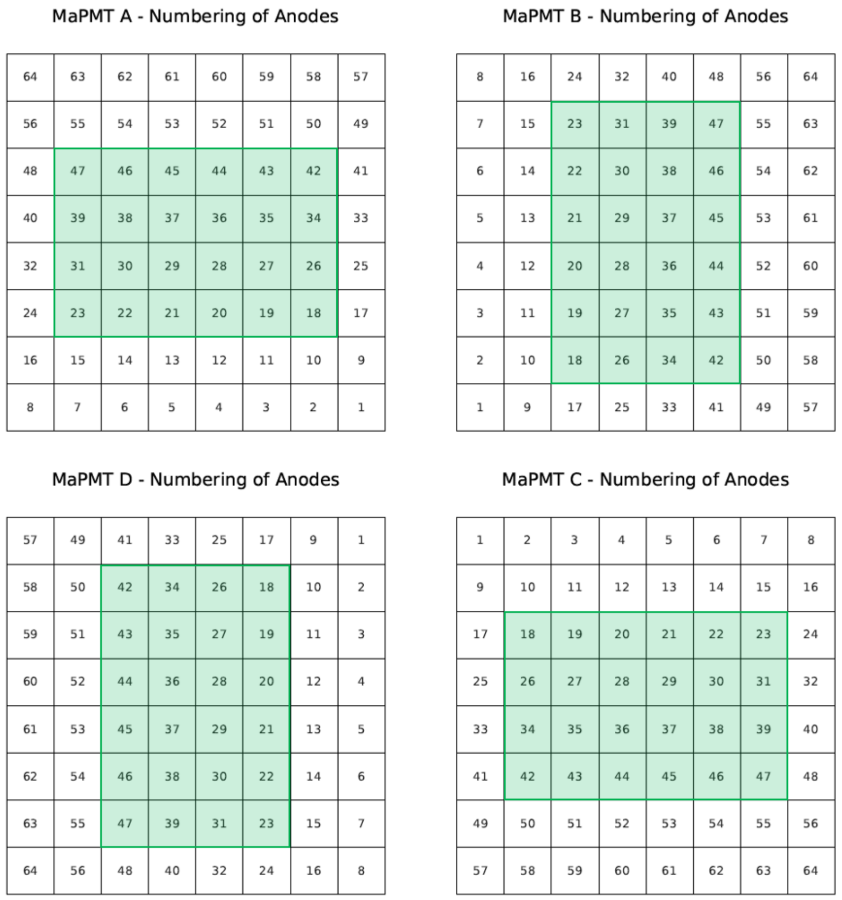

MaPMT A - Numbering of Anodes

64	63	62	61	60	59	58	57
56	55	54	53	52	51	50	49
48	47	46	45	44	43	42	41
40	39	38	37	36	35	34	33
32	31	30	29	28	27	26	25
24	23	22	21	20	19	18	17
16	15	14	13	12	11	10	9
8	7	6	5	4	3	2	1

MaPMT B - Numbering of Anodes

8	16	24	32	40	48	56	64
7	15	23	31	39	47	55	63
6	14	22	30	38	46	54	62
5	13	21	29	37	45	53	61
4	12	20	28	36	44	52	60
3	11	19	27	35	43	51	59
2	10	18	26	34	42	50	58
1	9	17	25	33	41	49	57

MaPMT D - Numbering of Anodes

57	49	41	33	25	17	9	1
58	50	42	34	26	18	10	2
59	51	43	35	27	19	11	3
60	52	44	36	28	20	12	4
61	53	45	37	29	21	13	5
62	54	46	38	30	22	14	6
63	55	47	39	31	23	15	7
64	56	48	40	32	24	16	8

MaPMT C - Numbering of Anodes

1	2	3	4	5	6	7	8
9	10	11	12	13	14	15	16
17	18	19	20	21	22	23	24
25	26	27	28	29	30	31	32
33	34	35	36	37	38	39	40
41	42	43	44	45	46	47	48
49	50	51	52	53	54	55	56
57	58	59	60	61	62	63	64

#	SIN Fraction [%]								
	mean		ratio	abs min		ratio	abs max		ratio
EC1	0.52	1.14	0.46	0.28	0.52	0.54	1.10	3.65	0.30
EC2	0.54	1.27	0.43	0.24	0.58	0.41	1.14	2.98	0.38
EC3	0.57	0.85	0.67	0.27	0.32	0.84	1.06	2.57	0.41
EC4	0.55	1.29	0.43	0.20	0.66	0.30	1.59	2.69	0.59
EC5	0.55	1.45	0.38	0.09	0.53	0.17	1.65	4.76	0.35
EC6	0.90	1.38	0.65	0.34	0.62	0.55	1.97	5.15	0.38
EC7	0.59	1.45	0.41	0.26	0.67	0.39	1.23	5.57	0.22
EC8	0.74	2.16	0.34	0.39	0.86	0.45	2.09	5.89	0.35
EC9	0.66	1.07	0.62	0.31	0.50	0.62	1.67	2.59	0.64
EC10	0.93	1.19	0.78	0.40	0.37	1.08	2.52	5.54	0.45
EC11	0.67	1.61	0.42	0.37	0.60	0.62	2.01	4.86	0.41
EC12	0.64	1.59	0.40	0.17	0.43	0.40	1.25	5.29	0.24
Average	**0.66**	**1.37**	**0.48**	**0.28**	**0.56**	**0.50**	**1.61**	**4.30**	**0.37**
RMS	**0.45**	**1.98**	**0.23**	**0.08**	**0.33**	**0.26**	**2.78**	**20.00**	**0.14**

#	S/N Ratio								
	mean		ratio	abs min		ratio	abs max		ratio
EC1	206.03	104.60	1.97	89.66	26.43	3.39	362.44	190.57	1.90
EC2	207.52	89.38	2.32	86.98	32.59	2.67	413.33	172.01	2.40
EC3	188.58	139.77	1.35	93.13	37.89	2.46	369.70	308.22	1.20
EC4	226.59	84.18	2.69	61.75	36.12	1.71	508.66	150.85	3.37
EC5	272.23	86.42	3.15	59.43	20.02	2.97	1076.21	186.26	5.78
EC6	133.66	87.35	1.53	49.84	18.43	2.70	291.56	160.25	1.82
EC7	188.44	88.54	2.13	80.34	16.96	4.74	379.97	149.12	2.55
EC8	152.22	55.89	2.72	46.80	15.98	2.93	256.68	115.81	2.22
EC9	176.15	111.03	1.59	58.86	37.56	1.57	326.57	199.73	1.64
EC10	125.90	108.63	1.16	38.67	17.07	2.27	247.87	268.32	0.92
EC11	167.07	73.42	2.28	48.70	19.60	2.48	267.02	166.78	1.60
EC12	191.92	87.65	2.19	79.18	17.89	4.43	570.57	230.27	2.48
Average	**186.36**	**93.07**	**2.00**	**66.11**	**24.71**	**2.68**	**422.55**	**191.52**	**2.21**
RMS	**36224.87**	**9067.87**	**3.99**	**4696.04**	**682.56**	**6.88**	**226337.65**	**39367.40**	**5.75**

	Average								
	mean		ratio	abs min		ratio	abs max		ratio
SIN Fraction [%]	**0.66**	**1.37**	**0.48**	**0.28**	**0.56**	**0.50**	**1.61**	**4.30**	**0.37**
S/N Ratio	**186.36**	**93.07**	**2.00**	**66.11**	**24.71**	**2.68**	**422.55**	**191.52**	**2.21**

	RMS								
	mean		ratio	abs min		ratio	abs max		ratio
SIN Fraction [%]	**0.45**	**1.98**	**0.23**	**0.08**	**0.33**	**0.26**	**2.78**	**20.00**	**0.14**
S/N Ratio	**36224.87**	**93.07**	**3.99**	**4696.04**	**24.71**	**6.88**	**226337.65**	**191.52**	**5.75**

🟩 SIN-less 🟧 SIN-affected

Table 5.1: SIN Fraction and S/N Ratio results for the anodes hardly affected by SIN.

MaPMT A - Numbering of Anodes

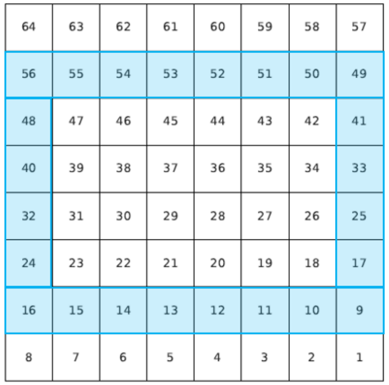

64	63	62	61	60	59	58	57
56	55	54	53	52	51	50	49
48	47	46	45	44	43	42	41
40	39	38	37	36	35	34	33
32	31	30	29	28	27	26	25
24	23	22	21	20	19	18	17
16	15	14	13	12	11	10	9
8	7	6	5	4	3	2	1

MaPMT B - Numbering of Anodes

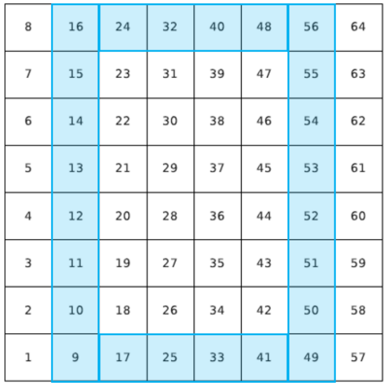

8	16	24	32	40	48	56	64
7	15	23	31	39	47	55	63
6	14	22	30	38	46	54	62
5	13	21	29	37	45	53	61
4	12	20	28	36	44	52	60
3	11	19	27	35	43	51	59
2	10	18	26	34	42	50	58
1	9	17	25	33	41	49	57

MaPMT D - Numbering of Anodes

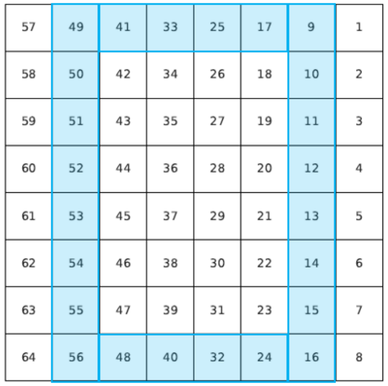

57	49	41	33	25	17	9	1
58	50	42	34	26	18	10	2
59	51	43	35	27	19	11	3
60	52	44	36	28	20	12	4
61	53	45	37	29	21	13	5
62	54	46	38	30	22	14	6
63	55	47	39	31	23	15	7
64	56	48	40	32	24	16	8

MaPMT C - Numbering of Anodes

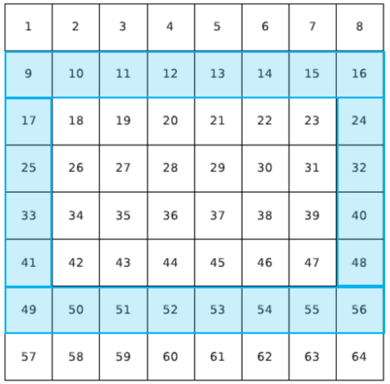

1	2	3	4	5	6	7	8
9	10	11	12	13	14	15	16
17	18	19	20	21	22	23	24
25	26	27	28	29	30	31	32
33	34	35	36	37	38	39	40
41	42	43	44	45	46	47	48
49	50	51	52	53	54	55	56
57	58	59	60	61	62	63	64

#	SIN Fraction [%]								
	mean		ratio	abs min		ratio	abs max		ratio
EC1	2.79	9.61	0.29	1.04	1.69	0.62	6.07	42.23	0.14
EC2	2.74	12.06	0.23	0.88	1.36	0.65	5.24	39.76	0.13
EC3	3.19	8.10	0.39	1.06	1.40	0.76	6.88	31.43	0.22
EC4	3.30	10.59	0.31	1.24	2.02	0.61	9.20	37.73	0.24
EC5	3.64	12.95	0.28	0.58	1.88	0.31	9.75	40.24	0.24
EC6	5.69	12.13	0.47	1.49	2.46	0.61	15.12	40.20	0.38
EC7	4.20	12.19	0.34	1.76	1.76	1.00	10.31	57.03	0.18
EC8	5.13	18.24	0.28	2.14	3.08	0.69	10.21	51.81	0.20
EC9	4.15	9.21	0.45	1.33	1.87	0.71	13.52	29.25	0.46
EC10	6.02	10.82	0.56	1.43	2.03	0.70	22.51	43.93	0.51
EC11	4.30	15.32	0.28	1.20	2.46	0.49	7.22	40.66	0.18
EC12	4.71	15.13	0.31	0.82	2.04	0.40	13.93	54.42	0.26
Average	**4.16**	**12.20**	**0.34**	**1.25**	**2.00**	**0.62**	**10.83**	**42.39**	**0.26**
RMS	**18.34**	**156.43**	**0.12**	**1.72**	**4.23**	**0.41**	**138.85**	**1862.32**	**0.07**

#	S/N Ratio								
	mean		ratio	abs min		ratio	abs max		ratio
EC1	40.43	16.10	2.51	15.48	1.37	11.30	95.46	58.21	1.64
EC2	42.18	14.21	2.97	18.07	1.51	11.97	112.11	72.50	1.55
EC3	36.68	23.03	1.59	13.53	2.18	6.21	93.23	70.44	1.32
EC4	35.02	14.71	2.38	9.87	1.65	5.98	79.97	48.44	1.65
EC5	50.98	13.77	3.70	9.25	1.49	6.21	169.96	52.13	3.26
EC6	23.79	14.11	1.69	5.61	1.49	3.77	66.10	39.66	1.67
EC7	26.84	14.82	1.81	8.70	0.75	11.60	55.67	55.74	1.00
EC8	21.72	8.25	2.63	8.79	0.93	9.45	45.81	31.49	1.45
EC9	30.72	15.61	1.97	6.40	2.42	2.64	74.41	52.49	1.42
EC10	21.07	14.74	1.43	3.44	1.28	2.69	69.10	48.36	1.43
EC11	25.68	9.34	2.75	12.85	1.46	8.80	82.00	39.67	2.07
EC12	29.65	12.12	2.45	6.18	0.84	7.36	120.60	48.00	2.51
Average	**32.06**	**14.23**	**2.25**	**9.85**	**1.45**	**6.80**	**88.70**	**51.43**	**1.72**
RMS	**1105.74**	**214.95**	**5.14**	**114.39**	**2.32**	**49.32**	**8900.14**	**2776.13**	**3.21**

	Average								
	mean		ratio	abs min		ratio	abs max		ratio
SIN Fraction [%]	**4.16**	**12.20**	**0.34**	**1.25**	**2.00**	**0.62**	**10.83**	**42.39**	**0.26**
S/N Ratio	**32.06**	**14.23**	**2.25**	**9.85**	**1.45**	**6.80**	**88.70**	**51.43**	**1.72**

	RMS								
	mean		ratio	abs min		ratio	abs max		ratio
SIN Fraction [%]	**18.34**	**156.43**	**0.12**	**1.72**	**4.23**	**0.41**	**138.85**	**1862.32**	**0.07**
S/N Ratio	**1105.74**	**14.23**	**5.14**	**114.39**	**1.45**	**49.32**	**8900.14**	**51.43**	**3.21**

🟩 SIN-less 🟧 SIN-affected

Table 5.2: SIN Fraction and S/N Ratio results for the anodes somewhat affected by SIN.

MaPMT A - Numbering of Anodes

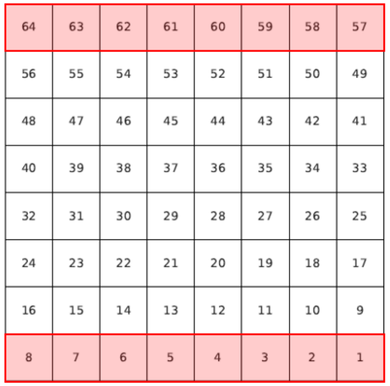

64	63	62	61	60	59	58	57
56	55	54	53	52	51	50	49
48	47	46	45	44	43	42	41
40	39	38	37	36	35	34	33
32	31	30	29	28	27	26	25
24	23	22	21	20	19	18	17
16	15	14	13	12	11	10	9
8	7	6	5	4	3	2	1

MaPMT B - Numbering of Anodes

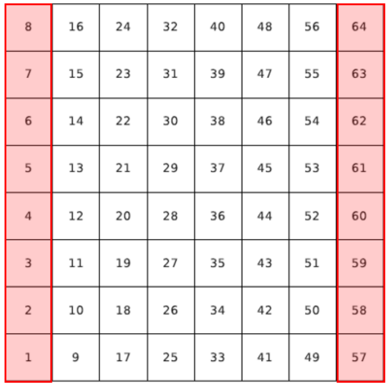

8	16	24	32	40	48	56	64
7	15	23	31	39	47	55	63
6	14	22	30	38	46	54	62
5	13	21	29	37	45	53	61
4	12	20	28	36	44	52	60
3	11	19	27	35	43	51	59
2	10	18	26	34	42	50	58
1	9	17	25	33	41	49	57

MaPMT D - Numbering of Anodes

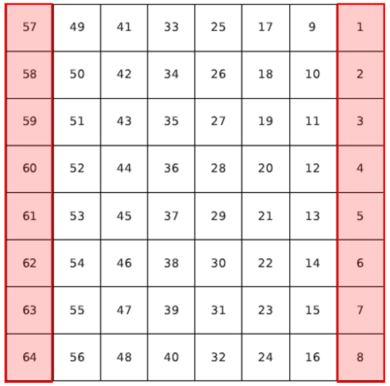

57	49	41	33	25	17	9	1
58	50	42	34	26	18	10	2
59	51	43	35	27	19	11	3
60	52	44	36	28	20	12	4
61	53	45	37	29	21	13	5
62	54	46	38	30	22	14	6
63	55	47	39	31	23	15	7
64	56	48	40	32	24	16	8

MaPMT C - Numbering of Anodes

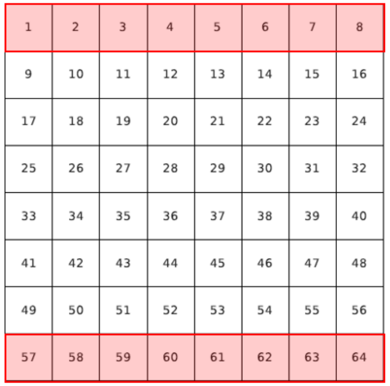

1	2	3	4	5	6	7	8
9	10	11	12	13	14	15	16
17	18	19	20	21	22	23	24
25	26	27	28	29	30	31	32
33	34	35	36	37	38	39	40
41	42	43	44	45	46	47	48
49	50	51	52	53	54	55	56
57	58	59	60	61	62	63	64

#	SIN Fraction [%]								
	mean		ratio	abs min		ratio	abs max		ratio
EC1	14.87	46.06	0.32	6.74	18.90	0.36	23.53	78.65	0.30
EC2	15.38	51.88	0.30	7.00	15.97	0.44	25.60	74.30	0.34
EC3	16.12	39.89	0.40	7.44	6.20	1.20	25.69	75.92	0.34
EC4	15.87	49.04	0.32	5.72	18.18	0.31	31.71	77.08	0.41
EC5	15.99	50.77	0.31	1.80	10.95	0.16	36.58	80.14	0.46
EC6	23.80	50.29	0.47	4.30	2.46	1.75	42.46	40.20	1.06
EC7	18.48	48.78	0.38	7.65	16.22	0.47	34.55	85.59	0.40
EC8	20.89	62.13	0.34	10.47	28.81	0.36	32.95	84.90	0.39
EC9	18.58	42.78	0.43	5.16	12.67	0.41	34.52	72.31	0.48
EC10	25.49	45.58	0.56	9.37	12.76	0.73	48.07	78.87	0.61
EC11	19.51	55.98	0.35	9.02	24.64	0.37	29.73	79.84	0.37
EC12	18.80	54.86	0.34	4.94	11.51	0.43	32.76	82.68	0.40
Average	**18.65**	**49.84**	**0.37**	**6.63**	**14.94**	**0.44**	**33.18**	**75.87**	**0.44**
RMS	**358.20**	**2517.21**	**0.14**	**49.38**	**271.93**	**0.18**	**1146.19**	**5886.94**	**0.19**

#	S/N Ratio								
	mean		ratio	abs min		ratio	abs max		ratio
EC1	6.50	1.45	4.48	3.25	0.27	12.04	13.85	4.29	3.23
EC2	6.21	1.18	5.26	2.91	0.35	8.31	13.29	5.26	2.53
EC3	5.79	2.32	2.50	2.89	0.32	9.03	12.44	15.12	0.82
EC4	6.19	1.32	4.69	2.15	0.30	7.17	16.49	4.50	3.66
EC5	9.28	1.40	6.63	1.73	0.25	6.92	54.46	8.13	6.70
EC6	4.45	1.48	3.01	1.36	1.49	0.91	22.26	39.66	0.56
EC7	5.07	1.47	3.45	1.89	0.17	11.12	12.08	5.17	2.34
EC8	4.15	0.74	5.61	2.03	0.18	11.28	8.55	2.47	3.46
EC9	5.38	1.74	3.09	1.90	0.38	5.00	18.38	6.89	2.67
EC10	3.40	1.58	2.15	1.08	0.27	4.00	9.67	6.84	1.41
EC11	4.46	0.95	4.69	2.36	0.25	9.44	10.08	3.06	3.29
EC12	5.56	1.19	4.67	2.05	0.21	9.76	19.22	7.69	2.50
Average	**5.54**	**1.40**	**3.95**	**2.13**	**0.37**	**5.77**	**17.56**	**9.09**	**1.93**
RMS	**32.73**	**2.11**	**15.51**	**4.92**	**0.25**	**19.34**	**448.16**	**177.46**	**2.53**

	Average								
	mean		ratio	abs min		ratio	abs max		ratio
SIN Fraction [%]	**18.65**	**49.84**	**0.37**	**6.63**	**14.94**	**0.44**	**33.18**	**75.87**	**0.44**
S/N Ratio	**5.54**	**1.40**	**3.95**	**2.13**	**0.37**	**5.77**	**17.56**	**9.09**	**1.93**

	RMS								
	mean		ratio	abs min		ratio	abs max		ratio
SIN Fraction [%]	**358.20**	**2517.21**	**0.14**	**49.38**	**271.93**	**0.18**	**1146.19**	**5886.94**	**0.19**
S/N Ratio	**32.73**	**1.40**	**15.51**	**4.92**	**0.37**	**19.34**	**448.16**	**9.09**	**2.53**

🟩 SIN-less 🟧 SIN-affected

Table 5.3: SIN Fraction and S/N Ratio results for the anodes greatly affected by SIN.

MaPMT A - Numbering of Anodes

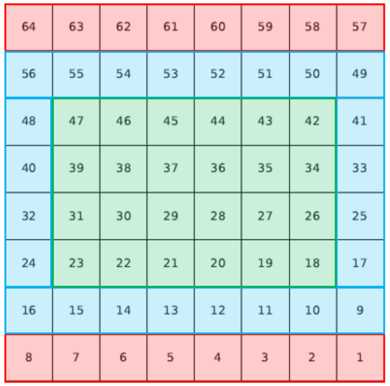

64	63	62	61	60	59	58	57
56	55	54	53	52	51	50	49
48	47	46	45	44	43	42	41
40	39	38	37	36	35	34	33
32	31	30	29	28	27	26	25
24	23	22	21	20	19	18	17
16	15	14	13	12	11	10	9
8	7	6	5	4	3	2	1

MaPMT B - Numbering of Anodes

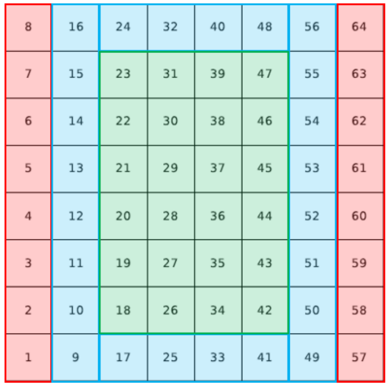

8	16	24	32	40	48	56	64
7	15	23	31	39	47	55	63
6	14	22	30	38	46	54	62
5	13	21	29	37	45	53	61
4	12	20	28	36	44	52	60
3	11	19	27	35	43	51	59
2	10	18	26	34	42	50	58
1	9	17	25	33	41	49	57

MaPMT D - Numbering of Anodes

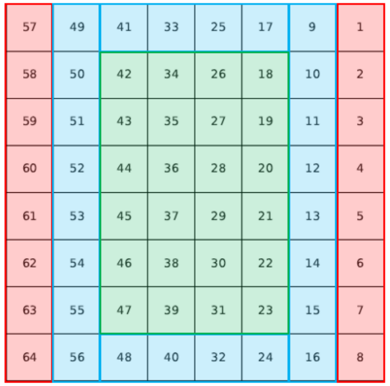

57	49	41	33	25	17	9	1
58	50	42	34	26	18	10	2
59	51	43	35	27	19	11	3
60	52	44	36	28	20	12	4
61	53	45	37	29	21	13	5
62	54	46	38	30	22	14	6
63	55	47	39	31	23	15	7
64	56	48	40	32	24	16	8

MaPMT C - Numbering of Anodes

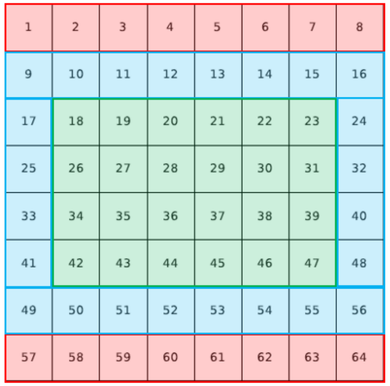

1	2	3	4	5	6	7	8
9	10	11	12	13	14	15	16
17	18	19	20	21	22	23	24
25	26	27	28	29	30	31	32
33	34	35	36	37	38	39	40
41	42	43	44	45	46	47	48
49	50	51	52	53	54	55	56
57	58	59	60	61	62	63	64

#	SIN Fraction [%]								
	mean		ratio	abs min		ratio	abs max		ratio
EC1	4.96	15.55	0.32	0.28	0.52	0.54	23.53	78.65	0.30
EC2	5.07	17.97	0.28	0.24	0.58	0.41	25.60	74.30	0.34
EC3	5.44	13.33	0.41	0.27	0.32	0.84	25.69	75.92	0.34
EC4	5.41	16.71	0.32	0.20	0.66	0.30	31.71	77.08	0.41
EC5	5.57	18.09	0.31	0.09	0.53	0.17	36.58	80.14	0.46
EC6	8.42	17.64	0.48	0.34	0.62	0.55	42.46	79.58	0.53
EC7	6.42	17.31	0.37	0.26	0.57	0.46	34.55	85.59	0.40
EC8	7.42	23.18	0.32	0.39	0.86	0.45	32.95	84.90	0.39
EC9	6.45	14.55	0.44	0.31	0.50	0.62	34.52	72.31	0.48
EC10	8.98	15.90	0.56	0.40	0.37	1.08	48.07	78.87	0.61
EC11	6.74	20.34	0.33	0.37	0.60	0.62	29.73	79.84	0.37
EC12	6.71	19.99	0.34	0.17	0.43	0.40	32.76	82.68	0.40
Average	**6.47**	**17.55**	**0.37**	**0.28**	**0.55**	**0.51**	**33.18**	**79.16**	**0.42**
RMS	**43.34**	**314.57**	**0.14**	**0.08**	**0.32**	**0.27**	**1146.19**	**6280.01**	**0.18**

#	S/N Ratio								
	mean		ratio	abs min		ratio	abs max		ratio
EC1	94.05	45.63	2.06	3.25	0.27	12.04	362.44	190.57	1.90
EC2	95.19	39.14	2.43	2.91	0.35	8.31	413.33	172.01	2.40
EC3	85.92	61.63	1.39	2.89	0.32	9.03	369.70	308.22	1.20
EC4	99.65	37.42	2.66	2.15	0.30	7.17	508.66	150.85	3.37
EC5	123.52	37.92	3.26	1.73	0.25	6.92	1076.21	186.26	5.78
EC6	60.16	38.42	1.57	1.36	0.26	5.23	291.56	160.25	1.82
EC7	82.00	39.13	2.10	1.89	0.17	11.12	379.97	149.12	2.55
EC8	66.27	24.23	2.74	2.03	0.18	11.28	256.68	115.81	2.22
EC9	78.92	47.92	1.65	1.90	0.38	5.00	326.57	199.73	1.64
EC10	55.96	46.66	1.20	1.08	0.27	4.00	247.87	268.32	0.92
EC11	73.39	31.27	2.35	2.36	0.25	9.44	267.02	166.78	1.60
EC12	84.48	37.71	2.24	2.05	0.21	9.76	570.57	230.27	2.48
Average	**83.29**	**40.59**	**2.05**	**2.13**	**0.27**	**7.98**	**422.55**	**191.52**	**2.21**
RMS	**7257.82**	**1726.51**	**4.20**	**4.92**	**0.08**	**65.43**	**226337.65**	**39367.40**	**5.75**

	Average								
	mean		ratio	abs min		ratio	abs max		ratio
SIN Fraction [%]	**6.47**	**17.55**	**0.37**	**0.28**	**0.55**	**0.51**	**33.18**	**79.16**	**0.42**
S/N Ratio	**83.29**	**40.59**	**2.05**	**2.13**	**0.27**	**7.98**	**422.55**	**191.52**	**2.21**

	RMS								
	mean		ratio	abs min		ratio	abs max		ratio
SIN Fraction [%]	**43.34**	**314.57**	**0.14**	**0.08**	**0.32**	**0.27**	**1146.19**	**6280.01**	**0.18**
S/N Ratio	**7257.82**	**40.59**	**4.20**	**4.92**	**0.27**	**65.43**	**226337.65**	**191.52**	**5.75**

🟩 SIN-less 🟧 SIN-affected

Table 5.4: SIN Fraction and S/N Ratio results for all the anodes affected by SIN.

5.8 Shippings

When all the measurements are completed and no errors occurred during the tests mentioned in the ECQA procedure, the ECs are prepared to be sent to the CERN for the columns installation. Each EC is taken off from a station and a barcode is assigned to it. A barcode is a QR code that is placed on the side of the aluminum casings for future EC identification. The ECs are then encapsulated in the plastic jars specially designed for it (Figure 5.34). The HV cable is wrapped around the aluminum case and tightened with a non-conductive adhesive tape. The MaPMTs have to always point upwards to prevent any loosening that could occur during the transportation from the test facilities to the CERN.

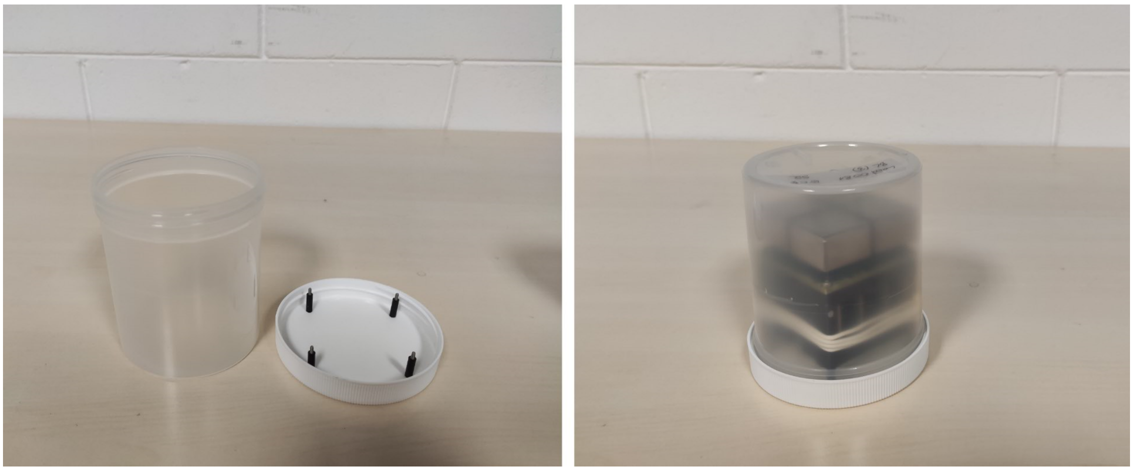

Figure 5.34: Encapsulation of an EC.

When the ECs are prepared (Figure 5.35), they are inserted in Korrvu cardboard boxes [127] (Figure 5.36). The ECs are secured with the plastic membranes from both sides. Similarly to the plastic jars, the boxes also have to point the upward direction. Up to two ECs are put in one box. Lastly, they are placed in a wooden box (Figure 5.37). Wooden boxes can accommodate a maximum of 40 cardboard boxes hence the shipments are usually sent with 80 tested ECs.

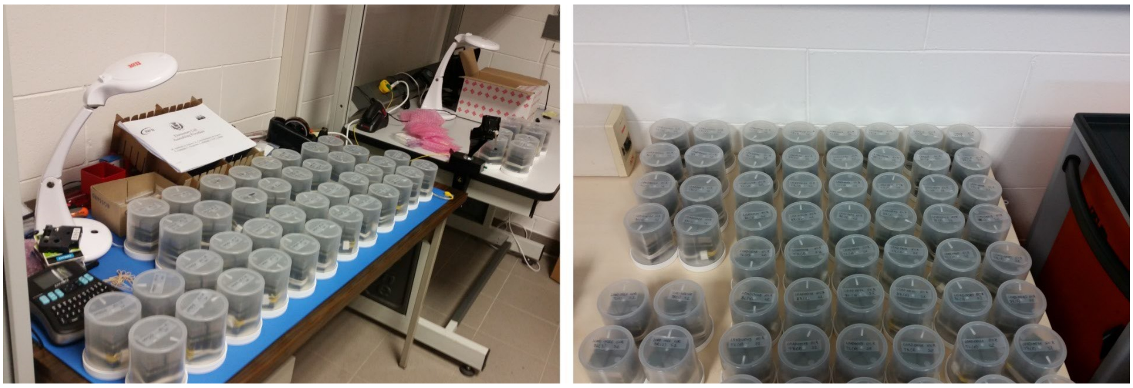

Figure 5.35: Encapsulated ECs ready to be placed in Korrvu cardboard boxes.

Figure 5.36: Korrvu cardboard box.

Figure 5.37: Wooden box used for transportation of ECs to the CERN.

Chapter 6

Summary

The studies presented in the thesis cover the opto-electronic chain for the upgraded RICH detectors at the LHCb experiment. The electronic instrumentation is currently under the assembly on detector columns or about to be operable. The significance of the PID has been shown on the example of the simplified analysis of the $B_s^0 \to D_s^{\mp} K^{\pm}$ decays performed by the Author. Based on very precise quality assurance, high detector performance is expected. The new photodetection units, called Elementary Cells, have proven to be extremely consistent, reliable and efficient. A total number of 387 R-Type and 194 H-Type ECs have been tested at Ferrara site. Only handful of them were not eligible for the RICH upgrade. To achieve a complete status, the experimental test setup has been prepared, specially designed for the quality control measurements on the ECs. The assembling procedure of the ECs and the test protocol have been created and followed throughout all the process. The fully automated software, dedicated for the quality assurance of the ECs, has been developed and performed exceptionally well with uninterrupted process. The offline data analysis scripts have been developed which provided graphical representation of performed tests, thus providing efficient way of the quality control. An undesired effect, called Signal-Induced Noise, has been looked into. The analysis concerned finding out the difference between the SIN-affected and SIN-less ECs. It has proven that the SIN-less ECs perform much more efficient and they are advised to be installed in the central regions of the RICH detectors. All the ECs that positively made the ECQA, have been prepared and shipped to CERN. All the key-data of the ECQA have been saved locally and sent to the CERN database.

Appendix A

Assembling Procedure

Aluminum plates are screwed together by eight M1.6x6 screws with torque of 1.0 Nm using conical Philips flat head screwdriver. Then, an aluminum case needs to be screwed with a Bb by four M2x6 screws with torque of 0.2 Nm using a hex socket head cap screwdriver. At the end, when a Bkb (R-type or H-type) is installed and connects FEBs from the other side, six M1.6x4 screws with torque of 0.1 Nm are screwed using a conical Philips flat head screwdriver.

Table A.1: An overview of the screws used during the assembly of ECs.

Screw Type	Quantity	Torque [Nm]	Head Type
M1.6x6	8	0.1	conical Philips flat head
M1.6x4	6		
M2.x6	4	0.2	hex socket head cap

Appendix B

Filenames

Table B.1: An overview of the filenames generated for specific measurements during the ECQA procedure.

Measurement	Filename
Communication Check	S_Curve_Comm_Check_offsetbit0.txt S_Curve_Comm_Check_offsetbit1.txt
Low Voltage	LV_noconf.txt LV_conf.txt
High Voltage	HV_nopmt.txt HV_pmt.txt
DAC Scan	S_Curve_cfg30A.txt S_Curve_cfg314.txt S_Curve_cfg31E.txt S_Curve_cfgB2A.txt S_Curve_cfgB34.txt S_Curve_cfgB3E.txt
Threshold Scan	THR_1000V_offset0.txt THR_1000V_offset1.txt
Dark Count Rate	DCR_1000V_cfg307_100s.txt DCR_1000V_cfgOptThr_100s.txt
Signal Induced Noise	SIN_1000V_cfgOptThr.txt SIN_950V_cfgOptThr.txt SIN_900V_cfgOptThr.txt SIN_850V_cfgOptThr.txt

Bibliography

[1] A. D. Sakharov, *Violation of CP invariance, C asymmetry, and baryon asymmetry of the universe*, Soviet Physics Uspekhi, vol. 34, no. 5, pp. 32–35, 1991.

[2] P. A. Zyla *et al.*, *Review of Particle Physics*, Progress of Theoretical and Experimental Physics, vol. 2020, no. 8, p. 083C01, 2020.

[3] F. Abe *et al.*, *Observation of Top Quark Production in* $\bar{p}p$ *Collisions with the Collider Detector at Fermilab*, Physical Review Letters, vol. 74, no. 14, pp. 2626–2631, 1995.

[4] S. Abachi *et al.*, *Observation of the Top Quark*, Physical Review Letters, vol. 74, no. 14, pp. 2632–2637, 1995.

[5] J. E. Augustin *et al.*, *Discovery of a Narrow Resonance in* e^+e^- *Annihilation*, Physical Review Letters, vol. 33, no. 23, pp. 1406–1408, 1974.

[6] J. J. Aubert *et al.*, *Experimental Observation of a Heavy Particle J*, Physical Review Letters, vol. 33, no. 23, pp. 1404–1406, 1974.

[7] J. Woithe, G. J. Wiener, and F. F. V. der Veken, *Let's have a coffee with the Standard Model of particle physics!* Physics Education, vol. 52, no. 3, 2017.

[8] G. Altarelli, *The Higgs and the Excessive Success of the Standard Model*, Frascati Physics Series, Frontier Objects in Astrophysics and Particle Physics, vol. 58, 2014.

[9] C. Patrignani, *Review of Particle Physics*, Chinese Physics C, vol. 40, no. 10, 2016.

[10] S. Tomonaga, *On a Relativistically Invariant Formulation of the Quantum Theory of Wave Fields*, Progress of Theoretical Physics, vol. 1, no. 2, pp. 27–42, 1946.

[11] J. Schwinger, *Quantum Electrodynamics. I. A Covariant Formulation*, Physical Review, vol. 74, no. 10, pp. 1439–1461, 1948.

[12] R. P. Feynman, *Mathematical Formulation of the Quantum Theory of Electromagnetic Interaction*, Physical Review, vol. 80, no. 3, pp. 440–457, 1950.

[13] S. L. Glashow, *Partial-symmetries of weak interactions*, Nuclear Physics, vol. 22, no. 4, pp. 579–588, 1961.

[14] A. Salam, *Weak and electromagnetic interactions*, World Scientific Series in 20th Century Physics, vol. 5, pp. 244–254, 1994.

[15] S. Weinberg, *A Model of Leptons*, Physical Review Letters, vol. 19, no. 1264, 1967.

[16] M. Gell-Mann, *A schematic model of baryons and mesons*, Physics Letters, vol. 8, no. 3, pp. 214–215, 1964.

[17] D. J. Gross and F. Wilczek, *Ultraviolet Behavior of Non-Abelian Gauge Theories*, Physical Review Letters, vol. 30, no. 26, pp. 1343–1346, 1973.

[18] G. Aad *et al.*, *Observation of a new particle in the search for the Standard Model Higgs boson with the ATLAS detector at the LHC*, Physics Letters B, vol. 716, no. 1, pp. 1–29, 2012.

[19] S. Chatrchyan *et al.*, *Observation of a new boson at a mass of 125 GeV with the CMS experiment at the LHC*, Physics Letters B, vol. 716, no. 1, pp. 30–61, 2012.

[20] F. Englert and R. Brout, *Broken Symmetry and the Mass of Gauge Vector Mesons*, Physical Review Letters, vol. 13, no. 9, pp. 321–323, 1964.

[21] P. W. Higgs, *Broken Symmetries and the Masses of Gauge Bosons*, Physical Review Letters, vol. 13, no. 16, pp. 508–509, 1964.

[22] T. Kajita, *Discovery of Atmospheric Neutrino Oscillations*, Nobel Lecture, 2015.

[23] A. B. McDonald, *The Sudbury Neutrino Observatory: Observation of Flavor Change for Solar Neutrinos*, Nobel Lecture, 2015.

[24] R. D. Peccei and H. R. Quinn, *CP Conservation in the Presence of Pseudoparticles*, Physical Review Letters, vol. 38, no. 25, pp. 1440–1443, 1977.

[25] J. H. Christenson, J. W. Cronin, V. L. Fitch, and R. Turlay, *Evidence for the* 2π *Decay of the* K_2^0 *Meson*, Physical Review Letters, vol. 13, no. 4, pp. 138–140, 1964.

[26] N. Cabibbo, *Unitary Symmetry and Leptonic Decays*, Physical Review Letters, vol. 10, no. 12, pp. 531–533, 1963.

[27] M. Kobayashi and T. Maskawa, *CP-Violation in the Renormalizable Theory of Weak Interaction*, Progress of Theoretical Physics, vol. 49, no. 2, pp. 652–657, 1973.

[28] L. Wolfenstein, *Parametrization of the Kobayashi-Maskawa Matrix*, Progress of Theoretical Physics, vol. 51, no. 21, pp. 1945–1947, 1983.

[29] N. Cabibbo, *Unitary Symmetry and Leptonic Decays*, Physical Review Letters, vol. 10, no. 12, pp. 531–533, 1963.

[30] The CKMfitter Group - Preliminary results as of Summer 2019 (EPS 2019 conference), website: http://ckmfitter.in2p3.fr/www/html/ckm$_{r}esults.html$.

[31] R. Aaij *et al.*, *Physics case for an LHCb Upgrade II - Opportunities in flavour physics, and beyond, in the HL-LHC era*, LHCB-PUB-2018-009, CERN-LHCC-2018-027, 2018.

[32] R. Aaij *et al.*, *Measurement of the* $B_s^0 \to \mu^+\mu^-$ *Branching Fraction and Effective Lifetime and Search for* $B^0 \to \mu^+\mu^-$ *Decays*, Physical Review Letters, vol. 118, no. 19, p. 191 801, 2017.

[33] R. Aaij *et al.*, *Search for the lepton-flavour violating decays* $B_s^0 \to e^\pm\mu^\mp$, Journal of High Energy Physics, no. 78, 2018.

[34] R. Aaij *et al.*, *Search for the lepton flavour violating decay* $\tau^- \to \mu^-\mu^+\mu^-$, Journal of High Energy Physics, no. 121, 2015.

[35] R. Aaij *et al.*, *Search for Majorana Neutrinos in* $B^- \to \pi^+\mu^-\mu^-$ *Decays*, Physical Review Letters, vol. 112, no. 13, p. 131 802, 2014.

[36] R. Aaij *et al.*, *Search for Baryon-Number Violating* Ξ_b^0 *Oscillations*, Physical Review Letters, vol. 119, no. 18, p. 181 807, 2017.

[37] C. Bobeth *et al.*, $B_{s,d} \to \ell^+\ell^-$ *in the Standard Model with Reduced Theoretical Uncertainty*, Physical Review Letters, vol. 112, no. 10, p. 101 801, 2014.

[38] S. L. Glashow, J. Iliopoulos, and L. Maiani, *Weak Interactions with Lepton-Hadron Symmetry*, Physical Review D, vol. 2, no. 7, pp. 1285–1292, 1970.

[39] CMS Collaboration & LHCb Collaboration, *Observation of the rare* $B^0_{(s)} \to \mu^+\mu^-$ *decay from the combined analysis of CMS and LHCb data*, Nature, vol. 522, pp. 68–72, 2015.

[40] R. Aaij *et al.*, *Test of Lepton Universality Using* $B^+ \to K^+ l^+ l^-$ *Decays*, Physical Review Letters, vol. 113, no. 15, p. 151 601, 2014.

[41] R. Aaij *et al.*, *Test of lepton universality with* $B^0 \to K^{*0} l^+ l^-$ *decays*, Journal of High Energy Physics, vol. 08, no. 55, 2017.

[42] R. Aaij *et al.*, *Measurement of CP asymmetry in* $B^0_s \to D^{\mp}_s K^{\pm}$ *decays*, Journal of High Energy Physics, vol. 03, no. 59, 2018.

[43] The LHCb Collaboration, *Update of the LHCb combination of the CKM angle* γ *using* $B \to DK$ *decays*, LHCb-CONF-2017-004 ; CERN-LHCb-CONF-2017-004, 2017.

[44] R. Aaij *et al.*, *Measurement of CP violation in* $B^0 \to J/\psi K^0_s$ *and* $B^0 \to \psi(2S) K^0_s$ *decays*, Journal of High Energy Physics, vol. 11, no. 170, 2017.

[45] R. Aaij *et al.*, *Precision Measurement of* CP *Violation in* $B^0_s \to J/\psi K^+ K^-$ *decays*, Physical Review Letters, vol. 114, no. 4, p. 041 801, 2015.

[46] R. Aaij *et al.*, *Measurement of the* CP*-Violating Phase* ϕ_s *in* $\overline{B}^0_s \to D^+_s D^-_s$ *Decays*, Physical Review Letters, vol. 113, no. 21, p. 211 801, 2014.

[47] R. Aaij *et al.*, *Measurement of* CP *violation in* $B^0_s \to \phi\phi$ *decays*, Physical Review D, vol. 90, no. 5, p. 052 011, 2014.

[48] R. Aaij *et al.*, *Measurement of the* CP *Asymmetry in* $B^0_s - \overline{B}^0_s$ *Mixing*, Physical Review Letters, vol. 117, no. 6, p. 061 803, 2016.

[49] R. Aaij *et al.*, *Determination of the quark coupling strength* $|V_{ub}|$*using baryonic decays*, Nature Physics, vol. 11, pp. 743–747, 2015.

[50] R. Aaij *et al.*, *Measurement of the Ratio of Branching Fractions* $\mathcal{B}(\overline{B}^0 \to D^{*+}\tau^-\overline{\nu}_\tau)/\mathcal{B}(\overline{B}^0_s \to D^{*+}\mu^-\overline{\nu}_\mu)$, Physical Review Letters, vol. 115, no. 11, p. 111 803, 2015.

[51] R. Aaij *et al.*, *Test of lepton flavor universality by the measurement of the* $B^0 \to D^{*-}\tau^+\nu_\tau$ *branching fraction using three-prong* τ *decays*, Physical Review D, vol. 97, no. 7, p. 072 013, 2018.

[52] R. Aaij *et al.*, *Measurement of the Ratio of Branching Fractions* $\mathcal{B}(B_c^+ \to J/\psi\tau^+\nu_\tau)/\mathcal{B}(B_c^+ \to J/\psi\mu^+\nu_\mu)$, Physical Review Letters, vol. 120, no. 12, p. 121 801, 2018.

[53] R. Aaij *et al.*, *Measurement of the Difference of Time-Integrated CP Asymmetries in* $D^0 \to K^-K^+$ *and* $D^0 \to \mu^-\mu^+$ *Decays*, Physical Review Letters, vol. 116, no. 19, p. 191 601, 2016.

[54] R. Aaij *et al.*, *Measurement of the CP Violation Parameter* A_Γ *in* $D^0 \to K^+K^-$ *and* $D^0 \to \mu^+\mu^-$ *Decays*, Physical Review Letters, vol. 118, no. 26, p. 261 803, 2017.

[55] R. Aaij *et al.*, *Updated determination of* $D^0-\overline{D}^0$ *mixing and CP violation parameters with* $D^0 \to K^+\pi^-$ *decays*, Physical Review D, vol. 97, no. 3, p. 031 101, 2018.

[56] L. Evans and P. Bryant, *LHC Machine*, Journal of Instrumentation, vol. 3, 2008.

[57] The Large Electron-Positron Collider, website: https://home.cern/science/accelerators/large-electron-positron-collider.

[58] A. Team, *The four main LHC experiments*, 1999.

[59] G. Aad *et al.*, *The ATLAS Experiment at the CERN Large Hadron Collider*, Journal of Instrumentation, vol. 3, S08003, 2008.

[60] S. Chatrchyan *et al.*, *The CMS experiment at the CERN LHC*, Journal of Instrumentation, vol. 3, S08004, 2008.

[61] K. Aamodt *et al.*, *The ALICE experiment at the CERN LHC*, Journal of Instrumentation, vol. 3, S08002, 2008.

[62] A. A. A. Jr *et al.*, *The LHCb detector at the LHC*, Journal of Instrumentation, vol. 3, S08005, 2008.

[63] O. Adriani *et al.*, *The LHCf detector at the CERN Large Hadron Collider*, Journal of Instrumentation, vol. 3, S08006, 2008.

[64] O. Acharya *et al.*, *The TOTEM Experiment at the CERN Large Hadron Collider*, Journal of Instrumentation, vol. 3, S08007, 2008.

[65] B. Acharya *et al.*, *The physics programme of the MoEDAL experiment at the LHC*, International Journal of Modern Physics A, vol. 29, no. 23, p. 1 430 050, 2014.

[66] Cryogenics - Low temperatures, high performance, website: https://home.cern/science/engineering/cryogenics-low-temperatures-high-performance.

[67] Linear Accelerator 2, website: https://home.cern/science/accelerators/linear-accelerator-2.

[68] The Proton Synchrotron Booster, website: https://home.cern/science/accelerators/proton-synchrotron-booster.

[69] The Proton Synchrotron, website: https://home.cern/science/accelerators/proton-synchrotron.

[70] The Super Proton Synchrotron, website: https://home.cern/science/accelerators/super-proton-synchrotron.

[71] J. Haffner, The CERN accelerator complex Complexe des accélérateurs du CERN, 2013.

[72] C. Elsässer, $\bar{b}b$ production angle plots.

[73] R. Aaij *et al.*, *LHCb detector performance*, International Journal of Modern Physics A, vol. 30, no. 07, p. 1 530 022, 2015.

[74] LHCb - Large Hadron Collider beauty experiment, website: http://lhcb-public.web.cern.ch/.

[75] R. Aaij *et al.*, *Performance of the LHCb Vertex Locator*, Journal of Instrumentation, vol. 9, P09007, 2014.

[76] J. Luisier, *Performance of LHCb Silicon Tracker Detector in the LHC*, Physics Procedia, vol. 37, pp. 851–858, 2012.

[77] LHCb Silicon Tracker - Material for Publications, website: https://lhcb.physik.uzh.ch/ST/public/material/index.php.

[78] R. Arink *et al.*, *Performance of the LHCb Outer Tracker*, Journal of Instrumentation, vol. 9, no. 01, P01002–P01002, 2014.

[79] M. Adinolfi *et al.*, *Performance of the LHCb RICH detector at the LHC*, The European Physical Journal C, vol. 73, no. 2431, 2013.

[80] Y. Guz, *The LHCb Calorimeter system: design, performance and upgrade*, Journal of Instrumentation, vol. 12, p. C07024, 2017.

[81] E. P. Olloqui, *LHCb Preshower(PS) and Scintillating Pad Detector (SPD): Commissioning, calibration, and monitoring*, Journal of Physics: Conference Series, vol. 160, p. 012 046, 2008.

[82] A. A. A. Jr *et al.*, *Performance of the LHCb muon system*, Journal of Instrumentation, vol. 8, P02022, 2013.

[83] T. Head, *The LHCb trigger system*, Journal of Instrumentation, vol. 9, p. C09015, 2014.

[84] RTA and DPA dataflow diagrams for Run 1, Run 2, and the upgraded LHCb detector, website: https://lhcbproject.web.cern.ch/lhcbproject/Publications/f/p/LHCb-FIGURE-2020-016.html.

[85] A. Piucci, *The LHCb Upgrade*, Journal of Physics: Conference Series, vol. 878, p. 012 012, 2017.

[86] R. Aaij *et al.*, *LHCb Trigger and Online Upgrade Technical Design Report*, Technical Design Report LHCb, CERN-LHCC-2014-016, 2014.

[87] R. Aaij *et al.*, *LHCb VELO Upgrade Technical Design Report*, Technical Design Report LHCb, CERN-LHCC-2013-021, 2013.

[88] T. Bird, *The upgrade of the LHCb Vertex Locator*, Journal of Instrumentation, p. C12041, 2014.

[89] R. Aaij *et al.*, *LHCb Tracker Upgrade Technical Design Report*, Technical Design Report LHCb, CERN-LHCC-2014-001, 2014.

[90] P. Hopchev, *SciFi: A large Scintillating Fibre Tracker for LHCb*, The Fifth Annual Conference on Large Hadron Collider Physics, 2019.

[91] R. Aaij *et al.*, *LHCb PID Upgrade Technical Design Report*, Technical Design Report LHCb, CERN-LHCC-2013-022, 2013.

[92] P. Cherenkov, *Visible emission of clean liquids by action of γ radiation*, Doklady Akademii Nauk SSSR, vol. 2, no. 451, 1934.

[93] C. Huygens, *Treatise On Light*, Macmillan And Company, 1912.

[94] Y. Hu *et al.*, *Cherenkov Radiation Control via Self-accelerating Wave-packets*, Scientific Reports, vol. 7, no. 8695, 2017.

[95] M. Alemi *et al.*, *First operation of a hybrid photon detector prototype with electrostatic cross-focussing and integrated silicon pixel readout*, Nuclear Instruments and Methods in Physics Research Section A: Accelerators, Spectrometers, Detectors and Associated Equipment, vol. 449, no. 1-2, pp. 48–59, 2000.

[96] N. Styles, *Hybrid Photon Detectors for the LHCb RICH System*, 2008.

[97] M. Fiorini, *The upgrade of the LHCb RICH detectors*, Nuclear Instruments and Methods in Physics Research Section A: Accelerators, Spectrometers, Detectors and Associated Equipment, vol. 952, p. 161 688, 2020.

[98] P. Garsed and S. Wotton, *PDMDB Motherboard*,

[99] P. Carniti and LHCb RICH Collaboration, *Beam test results for the upgraded LHCb RICH optoelectronic readout system*, Nuclear Instruments and Methods in Physics Research Section A: Accelerators, Spectrometers, Detectors and Associated Equipment, vol. 876, pp. 137–140, 2017.

[100] Hamamatsu Photonics, Chapter 9 Position Sensitive Photomultiplier Tubes.

[101] M. Baszczyk *et al.*, *CLARO: an ASIC for high rate single photon counting with multi-anode photomultipliers*, Journal of Instrumentation, vol. 12, P08019, 2017.

[102] Austria Micro Systems, website: https://ams.com/ams-start.

[103] Hamamatsu Photonics, Photomultiplier Tubes and Photomultiplier Tube Assemblies R11265U Series / H11934 Series.

[104] M. Baszczyk *et al.*, *LHCb RICH upgrade - Production Readiness Review report for the Elementary Cell of the Photo-Detector*, LHCb-2016-TBD, 2016.

[105] The LHCb RICH 2 Collaboration, *LHCb Upgraded RICH 2 Engineering Design Review Report*, LHCb-PUB-2016-015, 2016.

[106] M. P. Blago, *The LHCb RICH Upgrade*, The 39th International Conference on High Energy Physics (ICHEP2018), 2018.

[107] L. Cassina, *LHCb RICH Upgrade: an overview of the photon detector and electronics system*, Journal of Instrumentation, vol. 11, p. C01025, 2016.

[108] T. Abe *et al.*, *Belle II Technical Design Report*, 2010.

[109] SuperKEKB Collider, website: https://www-superkekb.kek.jp/.

[110] LHCb collaboration, *Computing Model of the Upgrade LHCb experiment*, CERN-LHCC-2018-014, 2018.

[111] R. Aaij *et al.*, *Design and performance of the LHCb trigger and full real-time reconstruction in Run 2 of the LHC*, Journal of Instrumentation, vol. 14, P04013, 2019.

[112] R. Aaij *et al.*, *A comprehensive real-time analysis model at the LHCb experiment*, Journal of Instrumentation, vol. 14, P04006, 2019.

[113] R. Aaij *et al.*, *Observation of CP violation in two-body $B^0_{(s)}$-meson decays to charged pions and kaons*, Journal of High Energy Physics, no. 3, 2021.

[114] R. Aaij *et al.*, *Observation of the Annihilation Decay Mode $B^0 \to K^+K^-$*, Physical Review Letters, vol. 118, no. 8, p. 081 801, 2017.

[115] R. Aaij *et al.*, *Measurement of CP observables in $B^\pm \to D^{(*)}K^\pm$ $B^\pm \to D^{(*)}\pi^\pm$ decays using two-body D final states*, Journal of High Energy Physics, 2020.

[116] R. Aaij *et al.*, *Measurement of the CKM angle γ in $B^\pm \to DK^\pm$ and $B^\pm \to D\pi^\pm$ decays with $D \to K^0_S h^+h^-$*, Journal of High Energy Physics, 2021.

[117] R. Aaij *et al.*, *Measurement of CP asymmetry in $B^0_s \to D^\mp_s K^\pm$ decays*, Journal of High Energy Physics, vol. 03, no. 59, 2018.

[118] R. Aaij *et al.*, *Measurement of CP violation in $B^0 \to D^\mp\pi^\pm$ decays*, Journal of High Energy Physics, vol. 06, no. 84, 2018.

[119] C. A. Beteta *et al.*, *Calibration and performance of the LHCb calorimeters in Run 1 and 2 at the LHC*, CERN-LHCb-DP-2020-001, 2020.

[120] R. Aaij *et al.*, *Decay chain fitting with a Kalman filter*, Nuclear Instruments and Methods in Physics Research Section A: Accelerators, Spectrometers, Detectors and Associated Equipment, vol. 552, no. 3, pp. 566–575, 2005.

[121] T. Chen and C. Guestrin, *XGBoost: A Scalable Tree Boosting System*, KDD 16: Proceedings of the 22nd ACM SIGKDD International Conference on Knowledge Discovery and Data Mining, pp. 785–794, 2016.

[122] J. Beringer *et al.*, *Review of Particle Physics*, Physical Review D 86, vol. 2020, no. 1, p. 010 001, 2012.

[123] iseg: High Voltage. Exactly., ECH 242 / 244, 2 / 4 Slot 19" MMS-Crate Series for iseg MMS High Voltage Power Supply Modules.

[124] iseg: High Voltage. Exactly., Crate Controller 2x Series Controller module for use with MMS compatible ECH crate series and MMS compatible modules.

[125] iseg: High Voltage. Exactly., EHS Series Versatile High Precision High Voltage Module with multiple Floating Options.

[126] Aim-TTi, AIM & Thurlby Thandar Instruments EL-R & EX-R Series.

[127] SealedAir, Korrvu® Suspension & Retention Packaging.